ABSTRACT

Title of Dissertation: ANALYSIS OF LASER PROCESSING OF METAL WIRES USED IN MICROELECTRONICS APPLICATIONS

Joo-Han Lee , Doctor of Philosophy, 2001

Dissertation directed by: Assistant Professor Joseph B. Bernstein
Department of Materials and Nuclear Engineering
Department of Electrical and Computer Engineering

Metal fuses for laser redundant links have been used for years in laser repair applications. However, reliability problems occur for laser metal cut structures, such as the material remaining at the bottom of the cut site or the formation of a lower corner crack. Furthermore, the improvement of laser cut processing remains an unsolved problem due to the variety of materials used for links as well as the complex thermo-mechanical mechanism of laser processing. This work discusses various aspects of the laser metal cut processing and the vertical make linking. Simulation results prove earlier experimental results that a laser-energy window exists for each cut structure under a specified laser pulse. Experimental observations reveal that the differential between upper corner stress and lower corner stress is temporarily dependent on the passivation breakthrough caused by upper corner cracks as predicted by simulation, and that lower-corner cracks can be formed at lower laser-energy level below passivation-break threshold energy.

3-D finite element modeling shows that upper corner stress in the case of pad cut structure is higher than that of simple line cut structure but the lower corner stress is lower due to the stress-relief effect. This proves that the pad cut structure is an improvement over simple line cut structure by increasing the time difference between upper cracking and lower cracking. In the analysis of copper cut process, upper cracking which is parallel to surface suggests lateral make-linking would be successful for the laser process of copper. In contrast to the metal cut link process, previously developed laser-induced vertical make link, connecting two different levels of metal lines using a laser pulse, is also studied in this work. From the scalability study of make link structure, two limitations are found in the process of scaled-down link structures which are the ratios of the thickness of inter-layer dielectric and the quality of laser beam parameters. A simple equation to estimate the scalability is acquired and 0.5 μm is evaluated to be possible for the metal 1 line with a 0.6 μm thick metal 1 line and a 0.5 μm thick inter layer dielectric. Energy process windows of various make link structures were simulated through finite element modeling and the results show a decreasing trend of relative energy window for smaller links, which is consistent with experimental results. It is also shown that there always exists an acceptable energy process window for any scaled links. A simple equation to evaluate the optimal spot size of laser beam for various link structure is presented. Dense layouts of interconnect were designed and proposed with a 1 μm pitch of 0.5 μm wide metal 1 line. As an application, an LPMCM substrate is designed using the vertical make-link structure.

ANALYSIS OF LASER PROCESSING OF METAL WIRES USED IN MICROELECTRONICS APPLICATIONS

by

Joo-Han Lee

Dissertation submitted to the Faculty of the Graduate School of the
University of Maryland, College Park in partial fulfillment
of the requirements for the degree of
Doctor of Philosophy
2001

Advisory Committee:

Assistant Professor Joseph B. Bernstein, Chairman/Advisor
Professor Kyu Yong Choi / Advisor
Associate Professor Neil Goldsman / Dean's Representative
Assistant Professor Raymond A. Adomaitis
Assistant Professor Tracey R. Pulliam Holoman

DEDICATION

To My Parents

ACKNOWLEDGEMENTS

I would like to thank my advisor, Professor Joseph Bernstein, for the time and encouragement given to me during this project. Without his support, this document would not exist. I also wish to thank Professor Kyu Yong Choi, my advisor in Chemical Engineering Department, for his support and help throughout my stay in Maryland. And I acknowledge the consenting to join the advisory committee and reviewing this thesis of Professor Neil Goldsman, Professor Raymond Adomaitis and Professor Tracey R. Pullium Holoman. Great appreciation must also be expressed to the members of Institute of Plasma Research, Professor John Melngailis, Professor Jon Orloff for putting up with me as I asked for help with facilities. I would also like to thank all the group members associated with laser processing for their help.

A undying thanks to my parents for being supportive, their love and prayer for me throughout my life. Similarly, Ji-Hun Kang, Sung-Hee Kang, Soo Min Cho, Wonsang Cho, have my special thanks for their help.

Finally, I would like to appreciate all to God who has led my life from the birth till now for allowing me to finish this work.

TABLE OF CONTENTS

LIST OF TABLES

LIST OF FIGURES

Chapter 1

Introduction

1.1 The Evolution of Laser Processing

The developments of lasers that followed the first flash lamp-pumped ruby laser in 1960 suddenly pushed the upper limit of coherent electronics from the millimeter-wave range, using microwave tubes and transistor, out to include the submilimeter, infrared, visible, ultraviolet spectral regions [4]. In the years since the first appearance of coherent light, lasers have become widespread and almost commonplace devices [5].

Lasers come in a great variety of forms, using many different laser materials, many different atomic system and kinds of pumping or excitation techniques. The beams of radiation that lasers emit or amplify have remarkable properties of directionality, spectral purity and intensity. These properties have already led to an enormous variety of applications in the industry for material processing, chemical processing and environmental analysis [6].

In the area of microelectronics, due to its high degree of precision, resolution and capability for automation, laser-beam processing techniques have found widespread application in the repair of integrated circuit chips for yield enhance-

ment and in some customization processes.

When fabricating Very Large Scale Integrated circuits(VLSI circuits) and Ultra Large Scale Integrated circuits(ULSI circuits) such as Dynamic Random Access Memory (DRAM) chips and Static Random Access Memory (SRAM) chips, it is often desirable to build redundancy into such circuits so as to increase the yield of acceptable chips [7]. For example, a DRAM or SRAM chip might be designed to include one or more redundant rows or columns. During final testing of the chip, if a fault is detected it is desirable to "wire around" the defect and thereby salvage what would otherwise be a defective chip. As is well known from earlier works, it is often possible to design a circuit such that "wire around" the defect may simply be accomplished by cutting and linking one or more electrical interconnects in the circuit.

Ideally, both line linking and line cutting systems should be combined and integrated into a semiconductor fabrication/testing line without the need for a vacuum chamber. If this were possible, the number of chips rejected on account of circuit flaws would be dramatically reduced due to the ease and speed of repair [8, 9].

Currently, circuit repair is a labor and time consuming process. Laser-assisted Chemical Vapor Deposition (LCVD) is one process for repairing flawed circuits through deposition of new metal lines. In LCVD, the laser is used to accelerate the overall deposition rate through photoadsorption and photodesorption of the precursor gas or dissociated products [10, 11]. A new metal line may thus be slowly "drawn" on the substrate as the laser spot moves across it. Unfortunately, these systems require ultra-high vacuum which make them time-intensive and uneconomical.

However, laser repair systems considered in this work retain a clear advantage over previously-used techniques in that they do not require vacuum for their operation and are less likely to damage the substrate when a circuit line may be linked with a laser at atmospheric pressure. A finely focused laser pulse of appropriate power and duration is all that is needed to make link. This technique was modeled and demonstrated well on poly-silicide links by C. Y. Lu *et al.* [12, 13] and on aluminum lines by H. Yamaguchi *et al.* [14].

Laser defect avoidance techniques based on novel methods of cutting and connection of interconnects for wafer-scale integration and programmable gate array applications have been developed. Redundancy techniques are generally divided into two classes; deletive and additive. The former means the cutting out of some structure by breaking the signal lines leading to it. The alternative additive techniques involve the ability to connect devices that were previously not present in the system and make new signal paths. Deletive procedures are naturally much simpler, were the first to be employed and have been more widely used [7]. For more complex structures, additive processes are of special interest. Both deletive and additive techniques can be realized by employing laser melting of lines and crossover structures on the integrated circuit.

Lasers also have a promising future in multichip modules (MCMs) manufacture. The need in electronic systems for higher clock speeds, lower power consumption, and greater compactness of functionality dictates the use of MCMs [3]. An MCM is built on a substrate that supports unpackaged integrated circuit chips mechanically, electrically and thermally, while it also provides interconnection between them with conductors not much larger than those on the chip themselves. The application of laser-induced link to a design for a Laser Pro-

grammable Multichip Module(LPMCM) will be detailed in the final chapter.

1.2 Material Properties and the Principle

In the test wafer, there are three main materials, aluminum, silicon dioxide, and silicon nitride. The principle of make-linking employs the contrast of material properties between the metal and the surrounding dielectrics (SiO_2/Si_3N_4). In case of aluminum, the metal line includes 1% silicon (Si) and 0.5% copper (Cu), which makes the melting temperature lower than pure aluminum by about 20-60°C. However, it is assumed as pure aluminum through this work for simplicity. On the other hand, Cu fuse metallization described in Chapter 4 was sputtered from 100% Cu sources.

Both of metal line are known to be buried under silicon dioxide (SiO_2) and silicon nitride (Si_3N_4) which are transparent to the Infrared (IR) laser. The TiN anti-reflective coating (ARC) layer on aluminum metallization also acts to increase the laser energy absorption in the metal because the reflectivity of TiN is much lower than that of aluminum. On the other hand, copper metallization has no ARC layer due to the low reflectivity of Cu.

The thermal conductivities of aluminum and copper are 170 and 270 times larger than that of silicon dioxide, and 10 and 17 times than that of silicon nitride, respectively. Therefore, when the laser impinges on the link designed site, we can assume that the passivation layers remain at room temperature while the metal increases its temperature dramatically.

Another significant feature of the combination of materials is the coefficient of thermal expansion (CTE). Due to the large CTE and the thermal conductivity of metal, Al and Cu, compared with those of silicon dioxide and/or silicon nitride,

a large tensile stress develops around metal line and is focused on upper-corners due to the geometry within the time frame of the laser pulse. Expanding metal fractures the dielectric separating them and the link can be formed by molten metal flowing though the crack around upper-corners of the lower metal line.

1.3 Laser Operation Parameters

The laser used in this research is a *Spectra Physics* diode-pumped Q-switched Nd:YLF laser (λ = 1047nm) operated in the saturated single-pulse mode. The laser has many variable parameters: spot size, pulse length, pulse repetition frequency(PRF), and pump power. The spot size and energy per pulse can be controlled by computer. In case of *ESI* 9275 laser system used in this work, the minimum $1/e^2$ spot size is 1.8$\times$ 1.8 μm. The maximum energy per pulse is related to the spot size, the bigger the spot size, the smaller the maximum laser energy. Wavelength also plays an important role in the laser's effectiveness. The wavelength of laser around from 1047nm to 1320nm is adequate and adopted for the processes because of its transparency in SiO_2 and Si_3N_4 and absorption by metal.

Positioning accuracy is also a concern here. Better positioning will make more laser energy effectively absorbed by metal which will result in better yields. Laser spot size is more tolerant to the positioning error, but at the same time, this is restricted by the fuse pitch in case of trimming and the size of upper metal frame hole for make linking. The pulse parameters were optimized to produce the best cutting and linking yield for this setup.

1.4 Laser Cut Process of Semiconductor Based Devices

The first commercial application of deletive redundancy involved certain designs of 64K DRAMs in 1979 [15]. A laser was employed to remove defective elements and replace then with redundant ones. In the work, poly-silicon fuses were employed for chip repair. Since then, this laser deletion technology has found the greatest applications in memory repair.

To repair the defective cells in chips, a certain number of spare rows and columns of memory cells were designed in to the memory chip layout. Then, wafer level testing is carried out during the fabrication processing. Defective cells were detected from the testing and the some specific links are then cut by laser pulses to wire around the faulty cells. Also, this laser cut processing activates the redundant rows and columns to replace the faulty cells.

At present, this laser cut processing has become a standard process in the industry for mass production of almost all memory devices, as well as a powerful tool in fabrication of other integrated circuits such as programmable logic devices or gate arrays, and ASICs [16].

Figure 1.1 shows the processed links with laser pulses to wire-around the defective cells in a DRAM device. It can be seen that the links every other link were processed and the fuse material was blown off.

However, laser cut-link processing has its own problems such as reliability concerns at processing and post-processing. Furthermore, using metal as the link material made the cut process more difficult than poly-silicon process. For older generation memory devices, poly-silicon was the main material used for links.

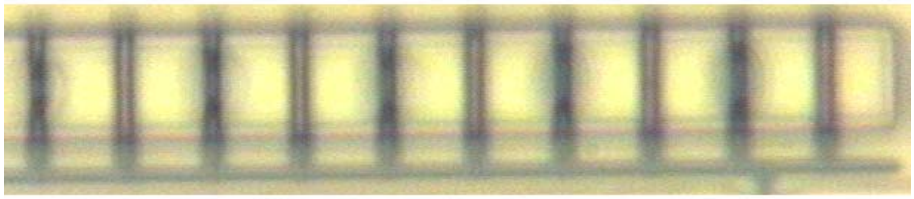

Figure 1.1: Top view of cut-links processed with laser pulses.

However, metals have become the necessary choice as the link materials due to the drawbacks of poly-silicon properties and processing.

Metal links gives far lower electrical resistance which helps the improvement of operation speed of devices. This is an important factor in current VLSI or ULSI devices. Also, poly-silicon links become deeply buried under many layers due to its nature of IC fabrication; as a result, the cutting of deeply buried link gets difficult. The analysis of of metal link cut processing and the process window will be covered in next chapter with detailed descriptions.

1.5 Laser-induced Make-Link

Ever since Hitachi disclosed the first method for making a link in 1984 [17], many ideas have been proposed in the past to make connections between two metal lines. Potential applications of a laser make-link are at least as extensive as the laser break-link. The ability to both make and break links allows for a much broader range of repair algorithms, and it is the goal of wafer scale integration [18]. In case of link-making, reduction of link structure size, increase in link yield, and seamless compatibility with standard complementary metal-oxide-semiconductor (CMOS)

processing steps are crucial elements for widespread utility of laser-restructurable circuit.

J. Raffel *et al.* have developed a laser-restructurable gate array application that can be fully tested prior to packaging and is fabricated using a standard CMOS process [19]. The technology uses laser cutting and both diffused and vertical forms of "linking". Diffused links are created by laser-melting the silicon between heavily doped regions. An ohmic connection of 100 to 300 Ω is formed between the two regions after the dopants redistribute within the molten area. Vertical links may be formed where two levels of metallizations cross when metal 2 is melted by the laser and alloys with the molten dielectric to form an aluminum-silicon connection to metal 1. Various diffused link structures have been studied and some of them have been in wide use [3, 20, 21, 22].

The main disadvantage of these methods of linking is that they require additional fabrication steps to deposit the link dielectric and the resistance of the connection is high. Another problem is the narrow energy range over which efficient heating and melting can occur without damage to the upper levels of metal and dielectric. Different vertical linking methods involving crack formation in the dielectric and metal flow through the crack to form the connection have been developed by H. Hartmann and T. Hillmann-Ruge, as well as M. Rouillon-Martin *et al.* [23, 24].

Compared with connections through silicon, direct metal-to-metal connections were made on standard CMOS processing, where links were formed when a laser was focused on a Tungsten metal 1 through an annular region of metal 2, but the linking yield was never shown to be better than 99%. High yield of vertical metal-to-metal links have been formed from a structure which was fabricated

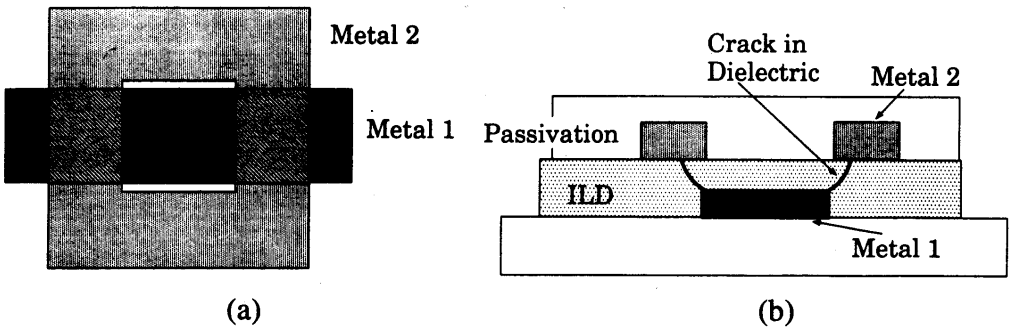

Figure 1.2: Design layout of an improved laser link structure. (a) Top view, and (b) cross-sectional view showing the vertical fracture path and filament [26].

using a standard two-level metallization process, proposed by J. Bernstein *et al.* (see Figure 1.2) [25]. In their work, they proposed the mechanism of formation of the vertical links as a thermomechanical fracture of the interlevel dielectric allowing molten metal to form a filament contact.

Recently, J. B. Bernstein *et al.* reported the parameters of laser which resulted in solid metallic connection with perfect yield as a result of the cracked dielectric between the two levels and the molten metal filling of the crack [26]. This vertical link has the advantage that the cracks are completely terminated on metal lines and there is no damage to the passivation. Also the laser process has a broad energy window and forms a robust link. On the other hand, there are remaining voids due to flows of molten metal to the cracks through thermal expansion while it is hot, which bring about the reliability issue. Zhang *et al.* performed electromigration tests to evaluated the void related reliability of the laser-induced vertical links and reported the link has sufficient reliability for practical implementation [27].

1.6 Objectives and Organization

The repeatability and reliability of the linking process was reported to be sufficient to meet the industry standards [28, 29, 27], thus, the understanding and comparison of make linking process and cut link process becomes important issues in order to catch up the VLSI technologies. The objective of this work is to study the process window of laser metal cut and make-link and its applications to practical devices.

ESI 9200 HT laser processing system and FIB/SEM dual-beam system from FEI were utilized in order to process and analyze the process window of the links. Also, finite element models were designed using MSC Marc 2000 for investigation of the time-dependent change of metal-dielectrics interactions under laser heating.

Mainly, this work can be separated into two parts. Chapters from 2 through 4 cover the analysis of conventional cut link including Cu fuse. On the other hand, the analysis of make link processing and the application are detailed from Chapter 5 through 8.

Chapter 2 covers the mechanism of conventional link cutting and the process window analysis using cross-sectional images. Also the upper and lower bound of process window of laser metal cut are defined. In Chapter 3, analysis of process window of pad-cut structure using 3-D finite models to study its advantages over simple line structure. Cross sections of the two different structure with energy variation are presented to compare the difference of the two process windows. Results of processing of Cu fuses under two different wavelength laser beam are detailed in Chapter 4.

Vertical make-link are introduced and the brief simulation results from finite element modeling are presented in Chapter 5. In Chapter 6, the scalability of ver-

tical make-link structure are calculated through the cross-sectional observations of larger make links. Chapter 7 covers the energy process window simulations of scaled make link and a design of a dense link layout adopting 1 μm fuse pitch are presented. Applications of make-link structures to laser programmable multichip module are shown through a substrate design including pads and tracks of metallizations.

Chapter 9 presents the conclusions of this research and some suggestions for future work.

Chapter 2

Analysis of Laser Metal-Cut Energy Process Window

2.1 Introduction

As stated earlier, laser technology has found the greatest application in devices which exhibit large-scale redundancy in their designs [15]. A laser is employed to remove defective elements and replace them with redundant ones.

In order to achieve successful laser-cutting of metal lines, material leftover at the bottom of cut-site and lower-corner cracks have become a major reliability issue. These two failure phenomena prevent the line from being completely disconnected and cause substrate damage as well [7, 30]. Laser processing involves the action of complex thermal and mechanical coupled mechanisms within a very short time frame of laser impingement. Therefore, it is essential to understand the kinetics in order to improve the reliability of laser processing.

Computer simulation models have been used to help understand the physical and thermal interactions induced by the laser within the metal structure. From the analyses of the simulations, proposals for improved cut structures, with better

performance, have been presented [31, 32, 33]. In this chapter, an analysis of the developments of upper and lower-corner cracks produced by the laser cutting of aluminum lines is presented. The results of computer simulations as well as experimental observations are both detailed in order to better understand the metal cutting process. The concept of a "process window" for reliable line cutting is also presented.

2.2 Dynamics of Crack Formation

Laser-induced line cutting is achieved by the complex interplay of both mechanical and thermal mechanisms. The thermal expansion of aluminum, caused by the transfer of energy from a laser pulse, induces the necessary thermo-mechanical mechanisms. Eventually, this action displaces the metal from the line. Together, these mechanisms combine to remove the intended material from the wafer surface.

The removal of metallic material is initiated by the application of a laser pulse to the designated cut-site of the aluminum line. Since the silicon nitride and silicon dioxide passivation layers are "transparent" to the laser spectrum (as compared to aluminum), most of the laser energy is absorbed by the metal line. Once the aluminum (or more accurately the metal over-coating) absorbs this energy, the temperature of the metal line increases. An increase in the temperature causes the metal to expand and, in turn, induces high tensile stress around the metal line in the surrounding dielectric layers.

The amount of stress generated around the metal line is mainly dependent upon the metallization geometry and the degree of mismatch between the thermal expansion coefficients of aluminum and the silicon dioxide surrounding it. Rect-

angular shaped cross-section of metallization causes high tensile stresses to be focused on the both upper and lower-corners of the metal line where laser pulse hits. Since the dielectric layer (silicon dioxide) is thicker below the line than above, greater stress will be induced at the upper-corners of the metal line, even when assuming a uniform temperature profile across aluminum line [34]. When accounting for a non-uniform temperature profile, due to the limited absorption depth of the initial stages of the laser pulse, the difference in stress between the upper and lower-corners will be even greater. The thermal profile within an aluminum line, over a period of a laser pulse, was presented by R. Rasera *et al.* [35].

Once a critical stress, σ_c, is reached, a crack is initiated at each of the upper-corners. Initiating from the upper-corners, the cracks tend to move perpendicularly to the local maximum principal tensile stress. Due to the brittle behavior of the glassy passivation, this crack propagates through the dielectric layers to the surface. It is considered that a crack initiates before superheated Al melts due to the hard surrounding passivation. The propagation of the cracks to the surface allows the metal to melt due to the pressure release caused by cracking and creates an explosion which ejects the metal away from the cut-site. Further studies are being continued to simulate the material yielding and the initiation and propagation of the cracks.

If the entire cross-section of aluminum melts (due to the diffusion of heat from the surface) when the passivation layer is ejected, then the molten aluminum will be removed at the instant that the explosion occurs. Simulations of crack formation (for rectangular line geometry) reveal that cracking at the lower-corners will also occur at high energies, but only after upper-corner cracking occurs.

It has been observed from experiments that the laser metal cut process is dependent upon the energy of the laser pulse used [30]. If the laser energy is too low, then some metal will remain at the bottom of cut-site after the explosion. Therefore, a connection will remain at the cut-site. On the other hand, if the laser energy is too high, then the lower-corners may crack before the explosion occurs. When this happens, molten metal fills the lower-corner cracks. These lower-corner cracks may damage the underlying circuitry and/or result in an incomplete cut [30].

2.3 Simulations

2.3.1 Finite Element Model

To simulate the crack formation process, a custom Finite Element Model (FEM) was utilized. The model was simulated using the MSC*Mentat* software. The models are illustrated in Figure 2.1, and you can also refer to the cross-sectional images of Figure 2.11 - 2.13 to see the correspondence with this representation.

Figure 2.1(a), depicts the situation during the initial period of laser heating, prior to crack initiation at the upper-corner. This stage of the model covers the period of time between the application of the laser pulse and the initiation of a crack at the upper-corner. After the crack is generated, a transition period occurs in which the stress at the lower-corner begins to be released. Propagation of the crack to the free surface occurs during this transition period. The transition period concludes when the passivation breaks. Figure 2.1(b), shows the result after the crack propagation and passivation break.

In the simulations, only half of the metal line structure was considered. This

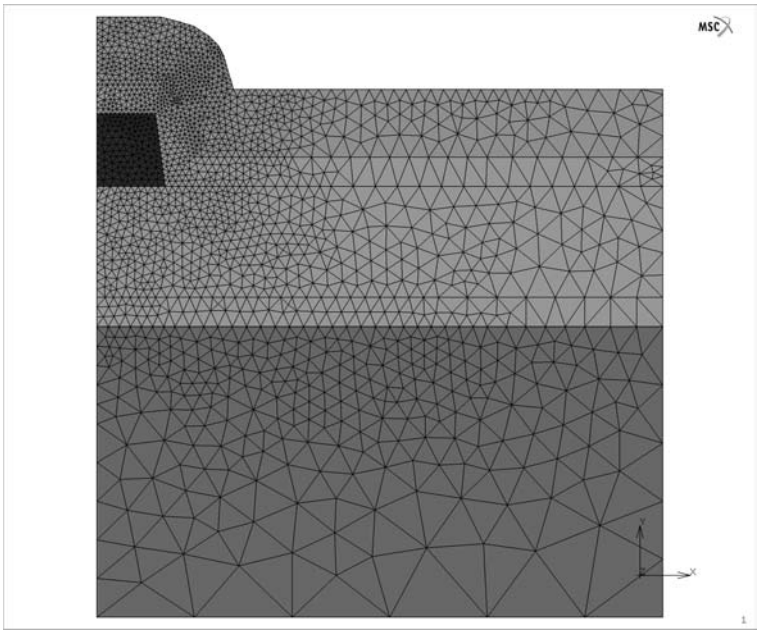

(a)

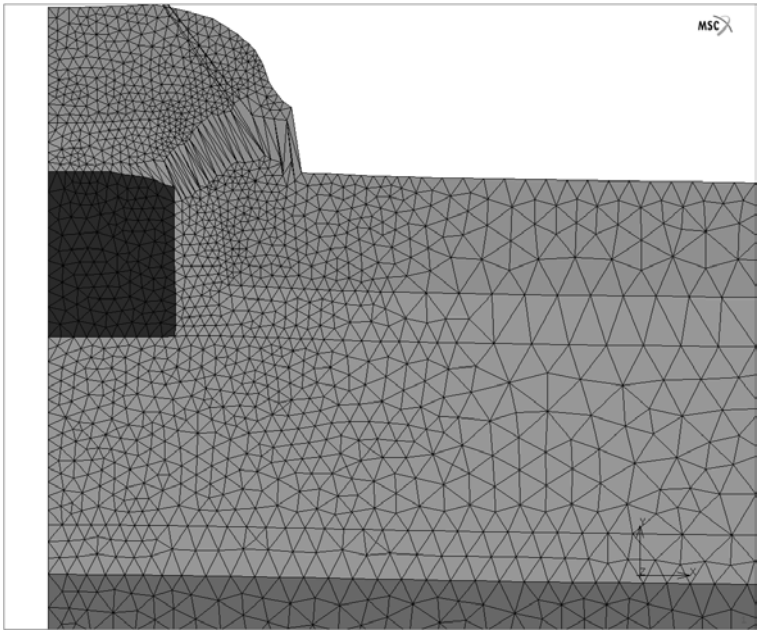

(b)

Figure 2.1: Finite element model simulated showing meshes. (a) Model before laser irradiation and (b) model after cracking and passivation break caused by laser energy.

was done since the metal line possesses a symmetrical cross-section. We assumed that the anti-reflective overcoating layer of the aluminum and dielectric layer accounted for 50% absorption of the impinged laser energy. Overcoating and undercoating layer were not considered in the mechanical simulation. The symmetric (vertical) axis of the simulation model was assumed to only exhibit vertical displacement. The other vertical axis (depicted on the right side of Figure 2.1(a)), as well as the bottom horizontal axis were treated as boundaries where no displacements and no temperature changes could occur.

The laser pulse was simulated to impinge on the surface of the wafer in the manner depicted in Figure 2.1(a). In addition, heating by the laser was simulated by heat flux from the top of the metal, obeying a Gaussian distribution [36]. Heating of the metal structure was considered only along its cross-section.

Because most of our concerns are at the upper and lower coners of the metal structure, different density of element was needed depending on the points in model. A triangle mesh was used for the simulations in order to make sure that there were enough elements around the corners of the structure. It has been proven that the results obtained from this mesh scheme are comparable with the traditional all-quadrilateral scheme [37].

2.3.2 Material Properties

Simulations adopt cm-g-sec unit system. The material properties employed are listed in Table 2.1 and Table 2.2. The material properties of Al were treated as those of pure aluminum for these models though the Al tested also contained 1% Si and 0.5% Cu. Also, the TiN/Ti over and undercoating layer were ignored for the sake of simplicity.

Table 2.1: Material properties I

Properties	Used value
Aluminum	
Density at 298K (g/cm^3)	2.702
Melting Point (K)	933
Specific Heat(J/g.K)	See Figure 2.2
Thermal Conductivity(W/cm.K)	See Figure 2.3
Young's Modulus(N/cm^2)	See Figure 2.4
Poisson's Ratio	0.345
Coefficient of Thermal Expansion(1/K)	See Figure 2.5
Silicon Dioxide(SiO_2)	
Density at 298K (g/cm^3)	2.27
Melting Point (K)	1708
Specific Heat(J/g.K)	See Figure 2.6
Thermal Conductivity(W/cm.K)	See Figure 2.7
Young's Modulus(N/cm^2)	See Figure 2.8
Poisson's Ratio	0.24
Coefficient of Thermal Expansion(1/K)	$5\times10^{-10}\times$Temperature(K)$+4\times10^{-7}$

Table 2.2: Material properties (continues from Table 2.1)

Properties	Used value
Silicon Nitride(Si_3N_4)	
Density at 298K (g/cm^3)	3.173
Melting Point (K)	$\sim$ 2151 decomposes
Specific Heat(J/g.K)	0.71
Thermal Conductivity(W/cm.K)	0.22
Young's Modulus(N/cm^2)	1.5×10^{7}
Poisson's Ratio	0.25
Coefficient of Thermal Expansion(1/K)	3.0×10^{-6}
Silicon (Si)	
Density at 298K (g/cm^3)	2.328
Melting Point (K)	1693
Specific Heat(J/g.K)	0.7
Thermal Conductivity(W/cm.K)	1.5
Young's Modulus(N/cm^2)	4.6×10^{6}
Poisson's Ratio	0.25
Coefficient of Thermal Expansion(1/K)	2.6×10^{-6}

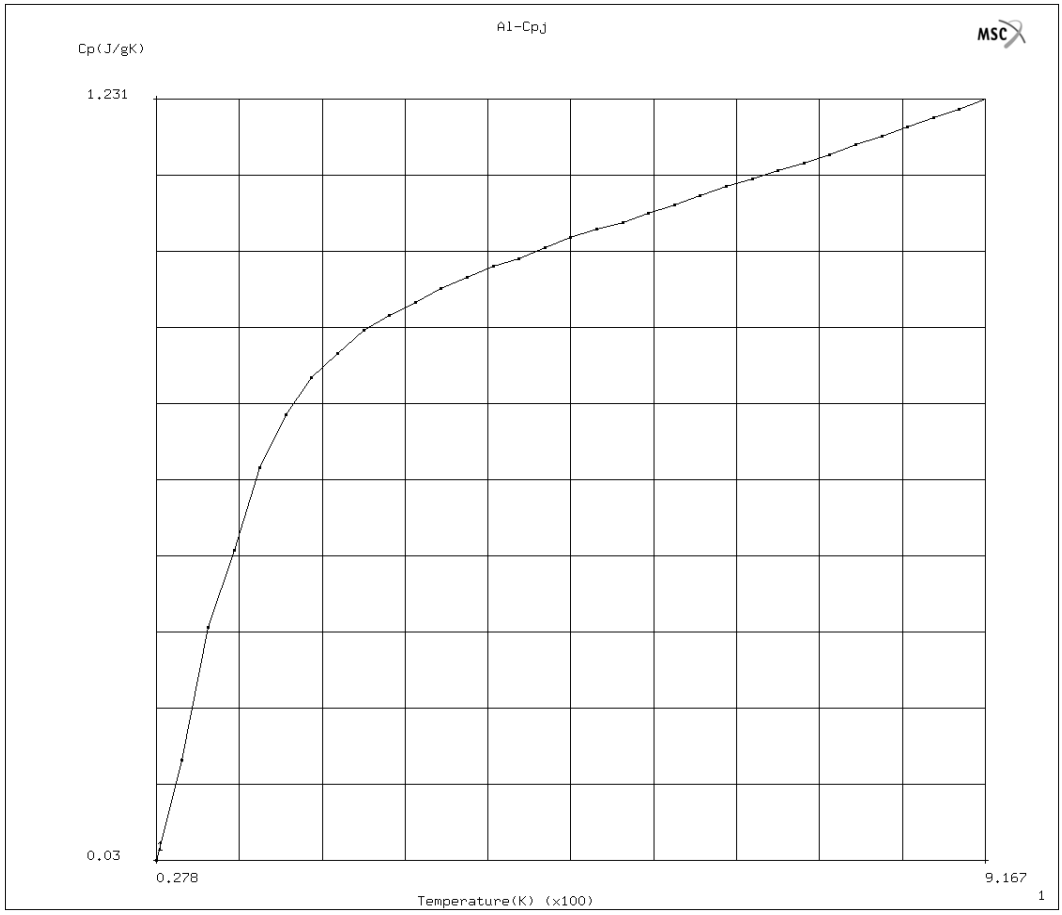

Figure 2.2: Specific Heat of pure aluminum.

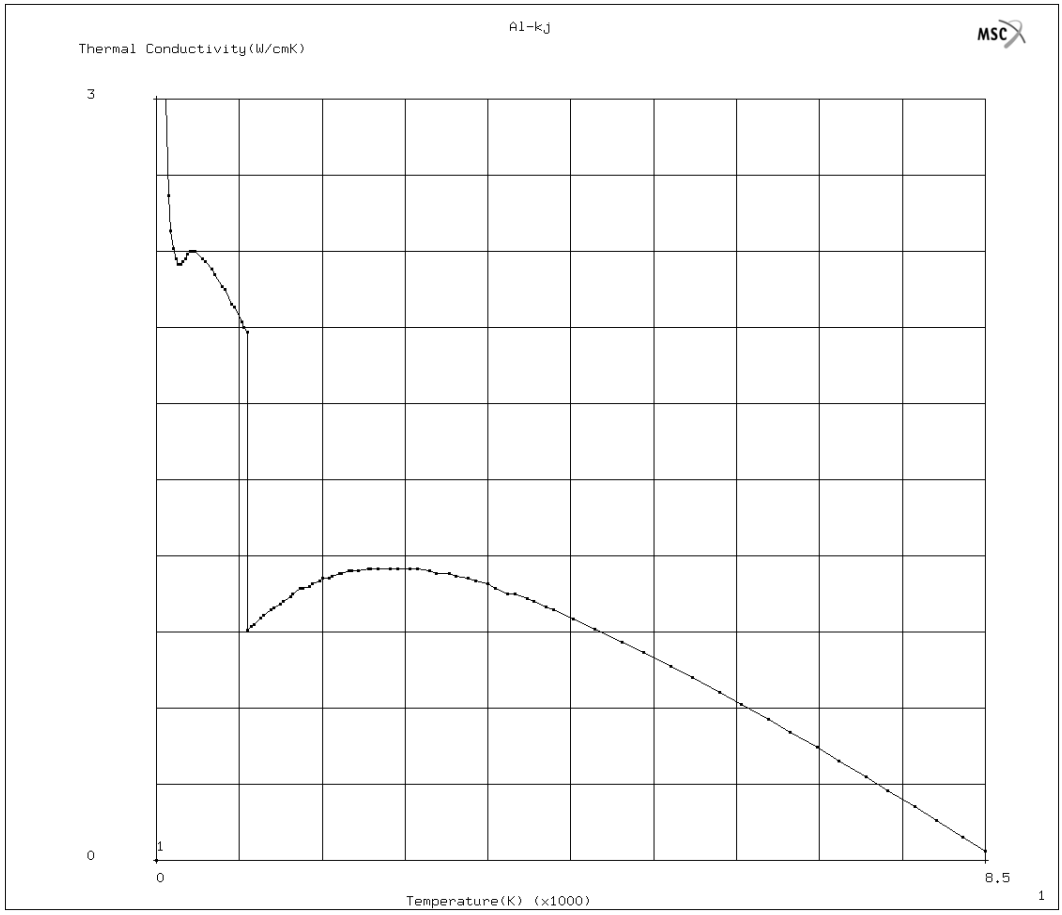

Figure 2.3: Thermal Conductivity of pure aluminum.

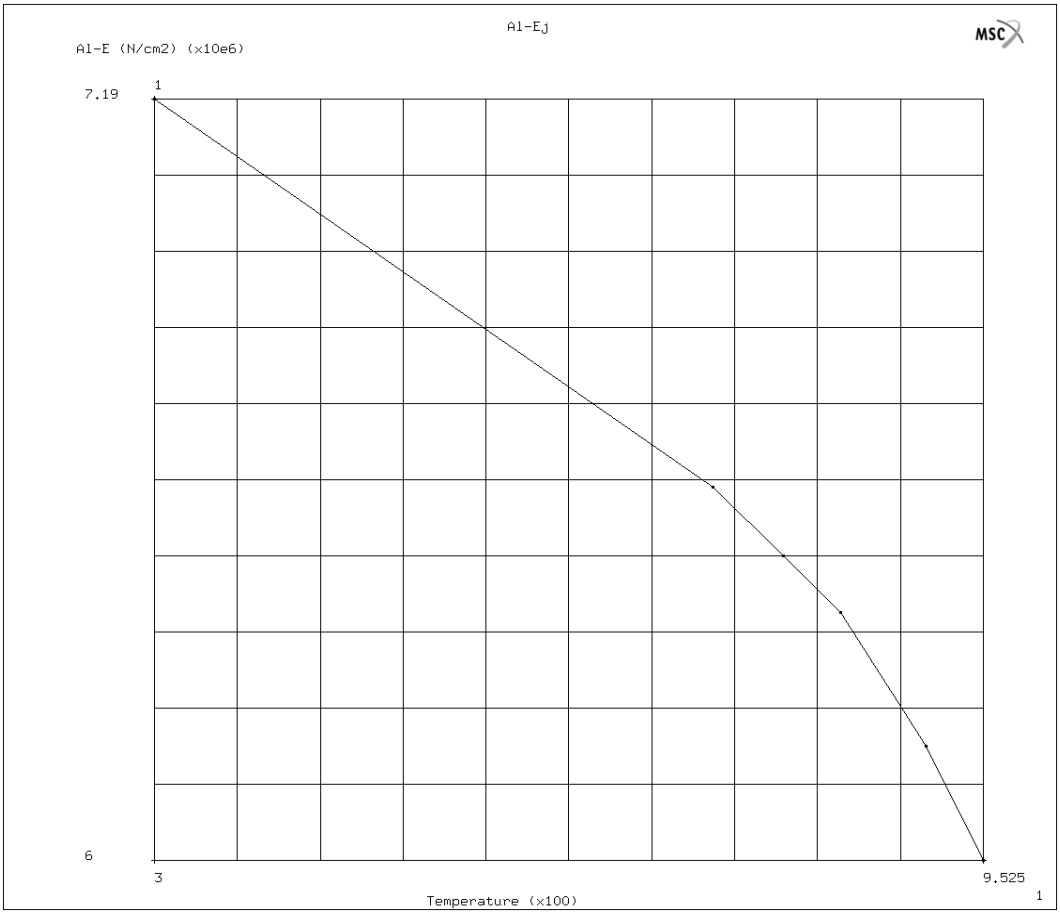

Figure 2.4: Young's Modulus of pure aluminum.

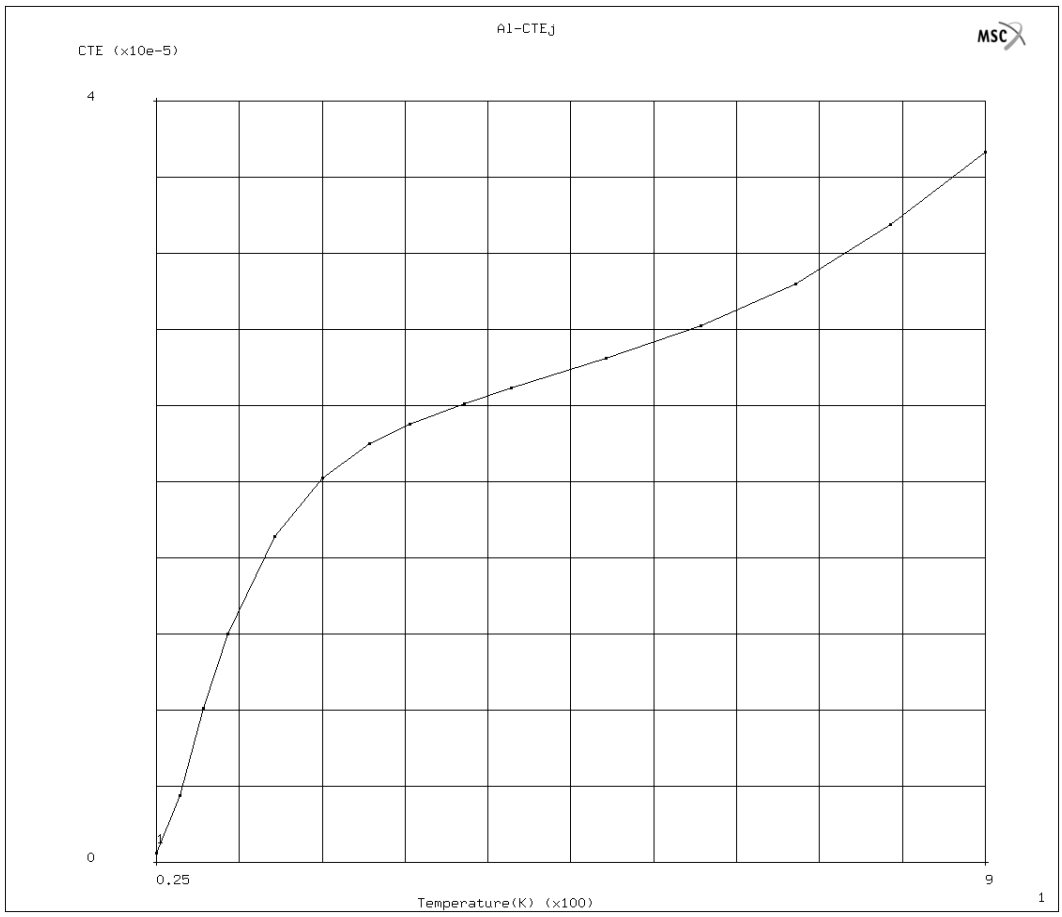

Figure 2.5: Coefficient of Thermal Expansion of pure aluminum.

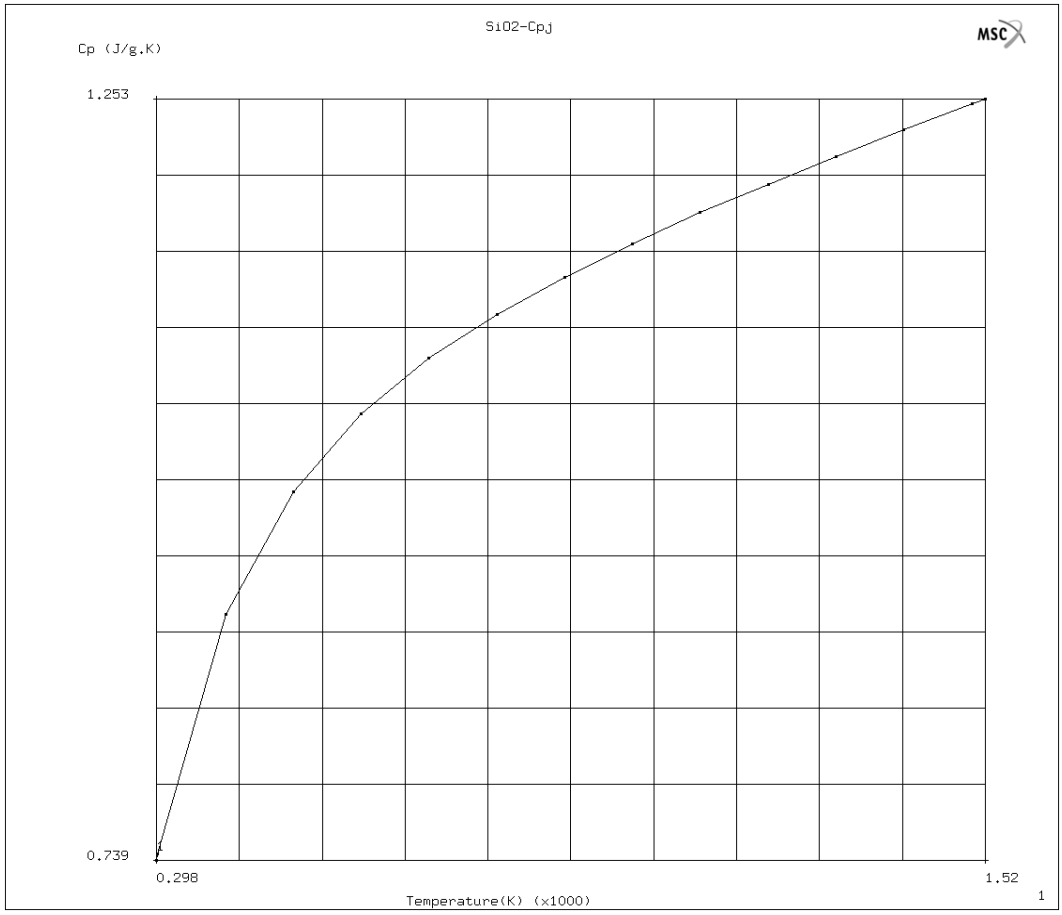

Figure 2.6: Specific Heat of silicon dioxide.

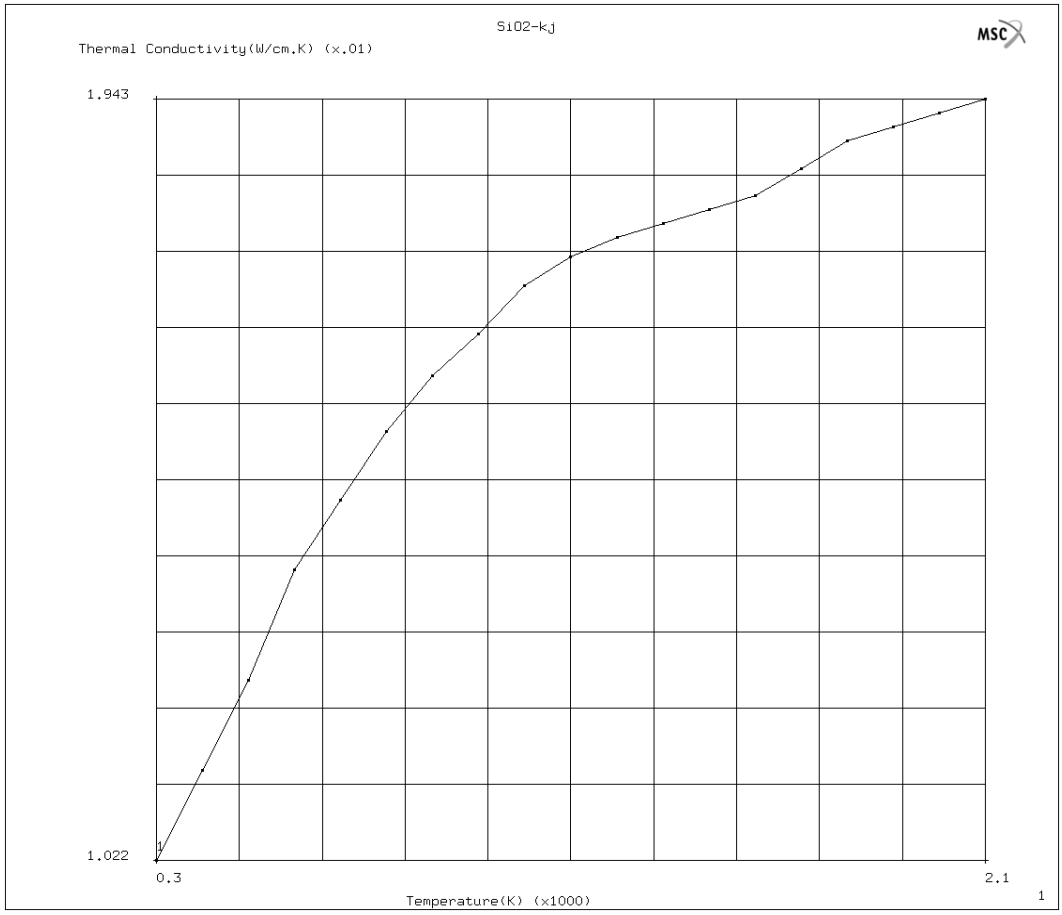

Figure 2.7: Thermal Conductivity of silicon dioxide.

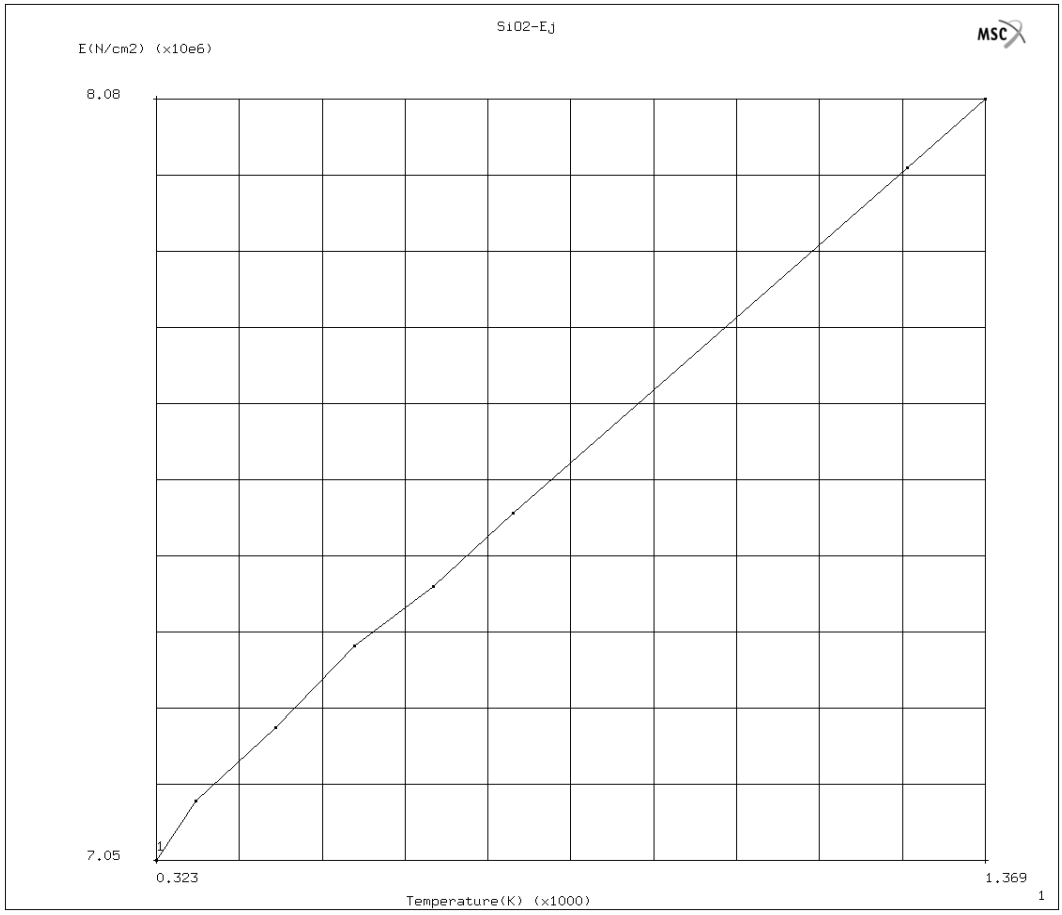

Figure 2.8: Young's Modulus of silicon dioxide.

2.3.3 Simulation Results

Simulation Curves

Sample simulation curves of the induced stress, at the upper and lower-corners of metal line under the laser heating, as a function of time is illustrated in Figure 2.9. The induced stresses are plotted on the vertical axis, in units of GPa and time is plotted on the horizontal axis, in units of ns. The two curves that are plotted are actually the results of two nodes closest to the Al corners in dielectric. Therefore, the stress values measured were somewhat lower than the actual stresses at the right on the upper and lower-corners of metal line. It is considered that there exist steep gradient of stresses between the Al corners and the closest nodes, and it was around from 300 MPa to 400 MPa depending on the location of node.

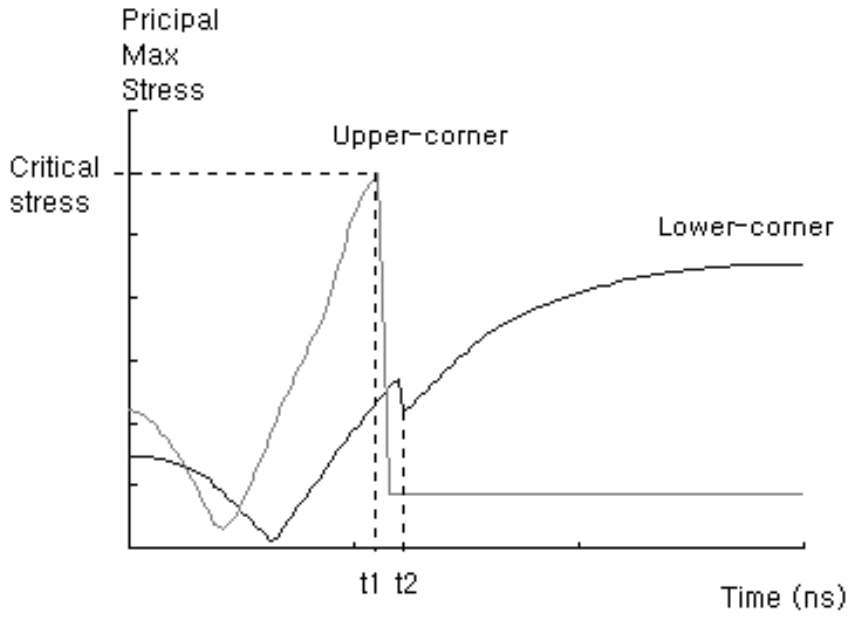

Figure 2.9: Result: Sample curves from simulation results.

The simulation results reveal that both the upper-corner stress (*Upper-corner*) and the lower-corner stress (*Lower-corner*) begin to be releaved for a short time to compensate the compressive stress caused by the fabrication at high temeprature when the laser pulse impinges on the structure. After the relaxation, the stresses start to increase. However, the stress at the upper-corner is greater than that at the lower-corner. This result is consistent with results of earlier works [34, 35]. The critical stress (stress necessary for crack initiation) at the upper corner, σ_c, occurs at time t_1 in Figure 2.9 where the crack initiates at upper-corner. In the simulations, it was clearly noticed that the stress at the upper-corner was sharply released upon passivation break at t_2 and dissapear .

The release of stress at the lower-corner, as a result of crack development at the upper-corner, can be noticed in Figure 2.9. When the upper-corner crack breaks the overlaying passivation, at time t_2, it is thought that the stress relief effect at lower-corner ends. However, the stress relief effects observed throughout the simulations were much less than actual since it was impossible to model the molten metal flow caused by laser energy.

When the metal line was processed with high laser energy, cracking at lower-corner was able to seen, thus sharp stress relief also observed. This will be more detailed in a later section.

Laser Cut Process Cases

The simulations using different laser energies were performed to illustrate the three main outcomes for a laser cut process. In these simulations, an aluminum line measuring 0.8 μm thick and 1.2 μm wide, with a 1.0 μm passivation layer, was used. A 15 ns triangular laser pulse, with a peak at 3.25 ns and a round $1/e^2$

spot size of 2.5 μm in diameter, was utilized to simulate the cut process. With the spot size of more than 2 times larger than metal line width, uniform laser energy density was assumed. Laser energies of 0.3μJ, 0.5μJ, and 1.2μJ, were selected for these simulations. Prior to the impingement of the laser, the structure was assumed to be at room temperature.

In each of the three simulations, the critical stress for dielectric cracking was assumed to be 1 GPa [38]. The crack propagation speed was found to be dependent on the laser energy. That is, a higher laser energy produced a higher propagation velocity. From the simulation, the time for crack propagation was approximately 1 ns. Even from calculation based on the fact that the crack propagation speed is limited to approximately 1/3 the speed of sound in the brittle, solid materials [39], a time of 1 ns is needed for the crack to propagate through a 1 μm thick passivation layer. Therefore, the simulation results were well consistent with the theory. In this work, 1 ns was used for the time of crack propagation. The explosion and ejection of material were assumed to occur at the same time that the crack penetrated the free surface (i.e. at time t_2), even though the explosion happens after passivation breakthrough.

The results of the simulation of a 0.3 μJ laser energy are displayed in Figure 2.10(a). As seen in the graph, an upper-corner crack was initiated at time t_1 = 5.5 ns and the stress at the upper-corner was released instantly. The stress releif at the lower-corner can be found from 6.4 ns to 6.7 ns and it indicates that most stress relief occur at a time when the crack reaches the free surface and the ejection of material occurs though the stress starts to be released from the time of cracking initiation.

The time for complete melting of the metal structure was calculated (by the

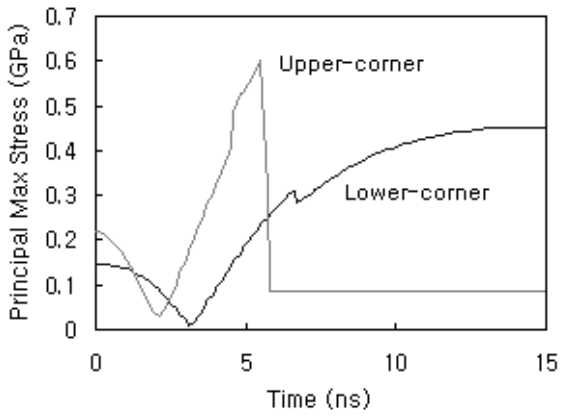

(a)

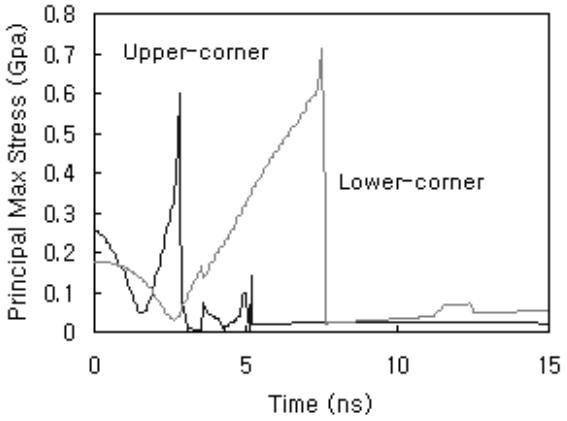

(b)

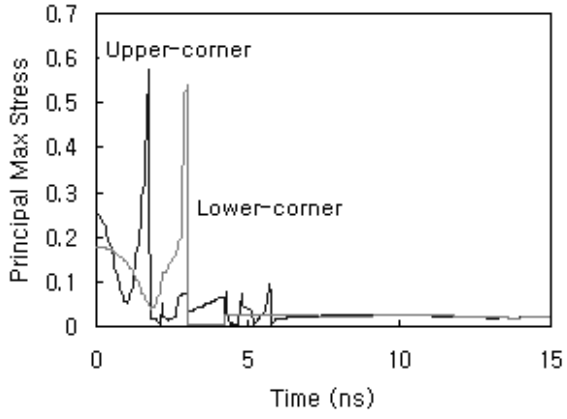

(c)

Figure 2.10: Results of finite element simulation with various laser energies, spot size: 2.5μm $1/e^2$ diameter. Laser energies: (a) 0.3μJ, (b) 0.5μJ, and (c) 1.2μJ.

simulation program) to occur at 8.0 ns. Therefore, from the simulation for a 0.3μJ laser energy, at time t_2 the heat diffusion from the surface did not melt the entire metal structure. As mentioned above, this incomplete melting causes some aluminum to remain at the bottom of the cut-site after the ejection of material.

When the laser energy was increased to 0.5μJ, initiation of the upper-corner crack was simulated to begin at time $t_1 = 2.8$ ns. The simulation results are displayed in Figure 2.10(b). In this case, the diffusion of heat in the aluminum line caused the aluminum to completely melt at the same time that the crack penetrated to the free surface ($t_2 = 3.8$ns). Therefore, all the molten aluminum, as well as the passivation layer of the cut-site, was ejected by the cut process. However, the stress curve at lower-corner kept increasing after the passivation break and crack was initiated at the corner at a time of 7.5 ns. This occurred due to the impossibility of simulating molten metal flow. Therefore, the stress development after passivation break should be ignored.

When a laser energy of 1.2 μJ was applied, initiation of the upper-corner crack was simulated to occur at time $t_1 = 1.7$ ns. The simulation results for this case are displayed in Figure 2.10(c). For this case, however, the diffusion of heat in the metal structure caused the entire structure to melt (at time $t = 2.4$ ns) before the crack reached the free surface (at time $t_2 = 2.7$ ns). Also the lower-corner stress (*Lower-corner*) reached σ_c before t_2. This results in the development of a lower-corner crack. Therefore, cracking initiated at lower-corner at time $t = 2.4$ ns.

From the results of the three cases, it is apparent that the stress difference between the upper and lower-corners (for the same instant of time) increases when the laser energy is increased. However, a higher energy also increases the lower-

corner stress curve (*Lower-corner*). A steeper slope for *Lower-corner* indicates that the lower-corner stress achieves the critical value faster. Therefore, the chance that lower-corner cracks will develop is increased. Also, it is noticed that the cracking initiate at a slightly lower temperature than Al melting temperature. However, it is noted that the properties of Al used for simulations were from pure Al and the metal line of Al including 1 % Si and 0.5 % Cu has a lower coefficient of thermal expansion. Therefore, this will compensate the lower temperature at the real time of cracking.

Laser Cut Process Window

The "process window" is a figure of merit used to describe the optimum range of laser energies for cutting metal lines. A lower-bound for reliable processing is given by the minimum energy needed to perform a cut without leaving any remaining metal at the cut-site. An upper-bound for reliable laser processing is given by the maximum energy which can perform a cut without creating a lower-corner crack [30]. The process window is thereby determined by taking the ratio of the upper-bound energy over the lower-bound energy.

The simulation results indicate that the laser energy, used for cutting, must fall within a specific range, or process window. The wider the process window is, the higher the possibility that a reliable cut will be performed. The range of the process window depends on many factors such as the metal line width, thickness, and passivation thickness, as well as on the parameters of the laser pulse. These variables and the consequent results of various process windows will be addressed in a later section of this chapter.

2.4 Experimental

2.4.1 Process Parameters and Test Setup

The test wafer, with the aluminum lines, was fabricated using a standard 2-level metal CMOS process. The upper-level metallization (the metallization used for this study) was sputtered $Al(1\%Si,\ 0.5\%Cu)$ etched to form 1.2μm wide and 0.75μm thick lines. A passivation layer, consisting of 0.7 μm of Si_3N_4 over 0.3μm of SiO_2, covered the metallization. The Al lines were undercoated and overcoated with a 0.09μm thick layer and a 0.05 μm thick layer of TiN respectively.

The laser system used to perform the cuts was an *XRL 525* laser process system. The system employs a *Spectra Physics* diode-pumped, Q-switched, Nd:YLF laser (1047nm) operated in the saturated single-pulse mode. Pulses, with lengths of approximately 15ns, were directed through focusing optics to produce a beam $1/e^2$ diameter of approximately 4.25μm (at focus). The positioning accuracy of the laser system was approximately 0.5μm. For the experiments, a series of laser energies, between 0.05μJ and 1.535μJ (in steps of 0.015μJ) were used.

Electrical measurements of processed cuts revealed unreliable data due primarily to the difficulty in completing the removal of the TiN barrier layer. Thus, we concentrated on studying the phenomenon of lower-corner cracking through FIB analysis since it was able to yield more consistent results that could be modeled by our FEA software. Of course we can not ignore the subsequent removal of the lower barrier material. Other considerations that were not addressed in this study include laser offset and the optical interference effects due to the thicknesses of the passivation layers.

Analysis of the laser cut processing was performed using a *Dual Beam 620D*

focused ion beam (FIB) and scanning electron microscope (SEM) system manufactured by FEI. The system was used to obtain cross-sectional images of the processed cut-sites and to investigate the crack evolution at the upper and lower-corners. The FIB cross-sections were made perpendicular to the wafer surface and parallel to the direction of the laser beam.

2.4.2 Experimental Observations

Figure 2.11(a) displays the cross-sectional view of a cut-site processed with a laser energy lower than the threshold energy needed for the aluminum to break through the passivation. The image clearly reveals that the laser energy was not high enough to perform the cut operation. The passivation layer was not removed by an explosion, therefore the metal could not be ejected from the cut-site.

In the case of Figure 2.11(a), a laser energy of 0.095μJ was used. Instead of the ejection of material, *Al*-filled lower-corner cracks were generated by the failed cut-process. Although upper-corner cracks were initiated, the stress-relief effect caused by them was not enough to prevent the lower-corner stress from generating cracks. The *Al*-filled, lower-corner cracks in Figure 2.11(a) also indicate that the heat diffusion, generated by the laser energy, was able to melt the *Al* metal all the way down to the bottom of the structure. This melting, without the occurrence of an explosion, was achieved even at a low laser energy.

The physical characteristics of the cracks provide hints about the development of stress over time in the metal structure. Due to imperfect processing, the metal line did not possess a rectangular cross-section. Instead, the cross-section was trapezoidal, with upper-corners of obtuse angles. This geometry seems to have resulted in the development of greater stress at the lower-corners. Consequently,

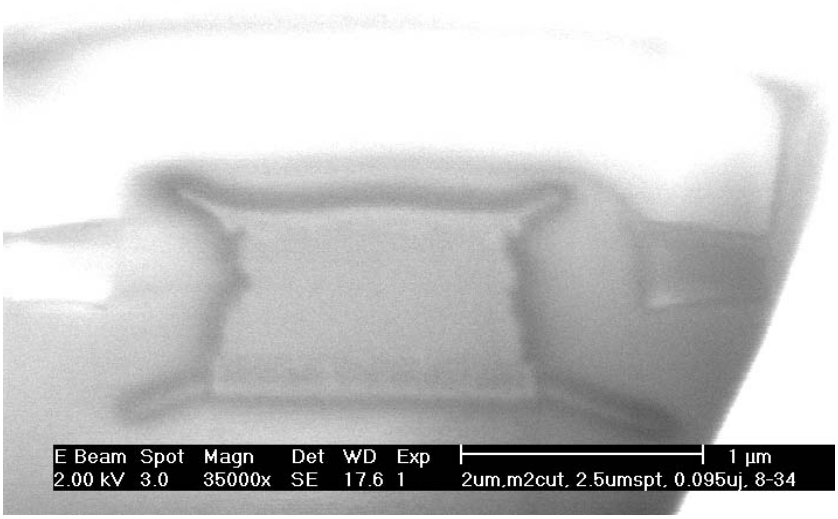

(a)

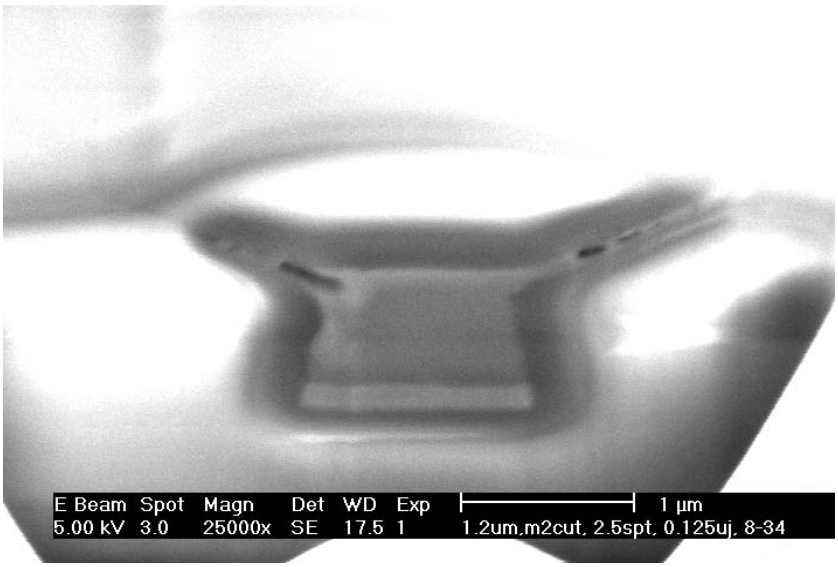

(b)

Figure 2.11: FIB cross-sectional images of laser-cut sites processed with energies below the process window, spot size: 4.25μm $1/e^2$ diameter. Laser energies: (a) 0.095μJ and (b) 0.125μJ.

lower-corner cracking was initiated at the same energy as upper-corner cracking.

The low energy development of lower-corner cracks may have been caused by the presence of the hard silicon nitride overcoating of the metal structure. Silicon nitride, which is harder than the silicon dioxide, seems to have retarded the propagation of the upper-corner cracks. Therefore, the stress at lower-corners of the structure prevailed in the process.

Figure 2.11(b) shows a cross-sectional view of a cut-site processed using a laser energy higher than threshold energy necessary to break the passivation completely (passivation-break threshold energy). In this case, a laser energy of 0.125μJ was used. Although the passivation was broken, the laser energy was still below the lower-bound needed to process reliable cuts.

The figure shows the successful break of cracks from both upper corners, through the passivation, to the free surface. Lower-corner cracks, on the other hand, did not develop. This indicates that lower-corner cracks are not as likely to develop as the laser energy is increased above the passivation-break threshold energy. Thus we see that the passivation break by the upper-corner cracks relieves stress from the lower-corners. This stress-relief is large enough to avoid lower-corner cracks.

A higher energy, such as the one used to process the cut-site in Figure 2.12(a) (0.2μJ), produces similar effects to processing with shorter laser pulses. That is, both methods heat up the upper section of the metallization within a very short period of time. Therefore, both methods accelerate the upper-corner cracks.

The image reveals that the upper-corner crack was initiated and propagated to the free surface (thereby initiating the explosion) well before the entire metal structure was able to melt. Therefore, metal remained at the bottom of the cut-

(a)

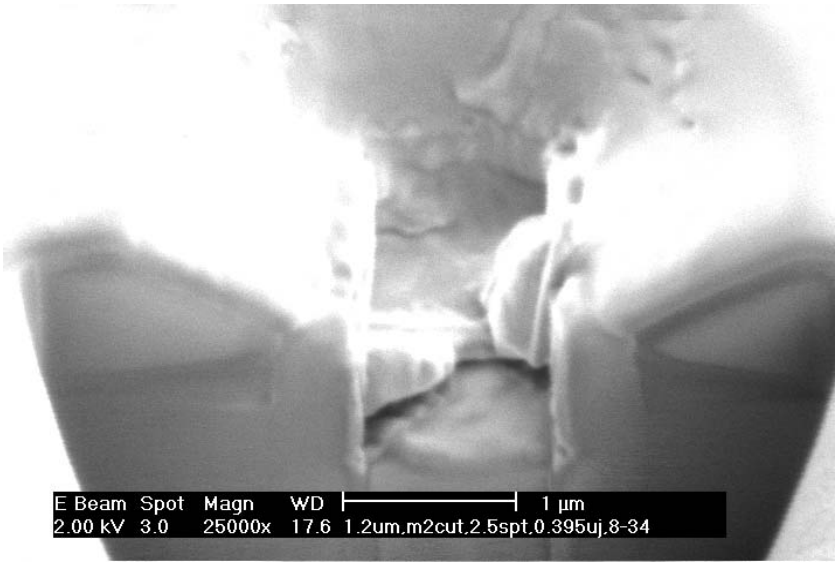

(b)

Figure 2.12: FIB cross-sectional images of laser-cut sites processed with energies between the passivation-break threshold energy and the upper-bound of process window, spot size: 4.25μm $1/e^2$ diameter. Laser energies: (a) 0.2μJ and (b) 0.395μJ.

site. Notice how the TiN underlayer, in Figure 2.12(b), was beginning to peel off at this laser energy.

In the case of Figure 2.12(b) a laser energy of 0.395μJ was used. The cross-sectional image portrays a clean, reliable cut. All of the aluminum, as well as the TiN undercoating, was removed by the cut process. The absence of lower-corner cracks indicates that the melting of the entire Al structure and the explosion occurred at approximately the same time. Therefore, the image indicates that the laser energy used was within the process window. However, lower-corner cracks may develop, even if an energy within the process window is used, if errors, such as a positioning offset of the laser spot, are introduced into the cut processing of narrow metal line.

The results of using high energy laser pulses to process cuts are displayed in Figure 2.13. These figures illustrate the effect of using a laser energy above the process window. In the first case, a laser energy of 0.8μJ was used. The image reveals unfilled lower-corner cracks which indicate that lower-corner cracking was initiated before the Al structure fully melted. In this state, the Al line is considered to be a superheated solid at the time of crack initiation, due to the high pressure induced under the hard passivation. When the pressure is released, in a dramatic manner, the metal is likely to melt instantly and explode.

The laser energy used to obtain Figure 2.13(b) was 0.980μJ. This energy is far beyond the process window. The image clearly shows the long, undesirable lower-left corner crack. The length of the crack poses a reliability concern, since it may form a short-circuit or damage surrounding structures. The asymmetric cracking is due to the laser-spot positioning offset.

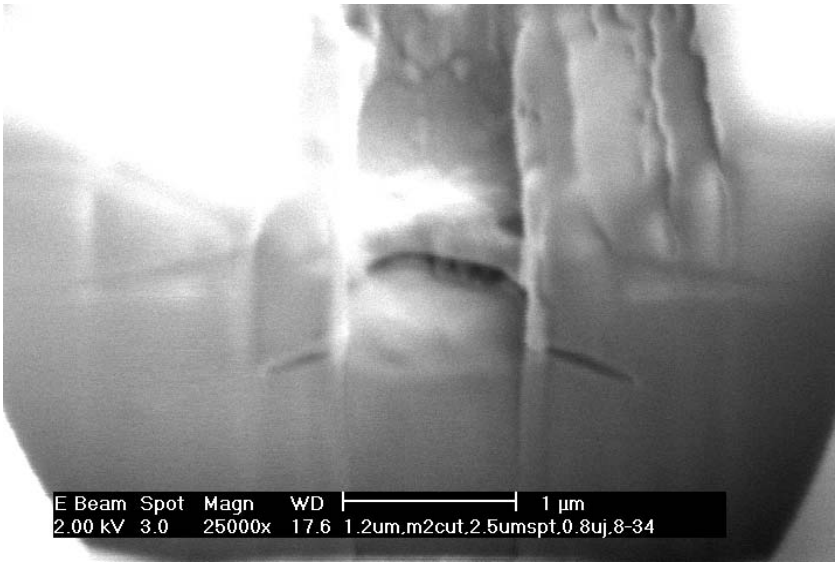

(a)

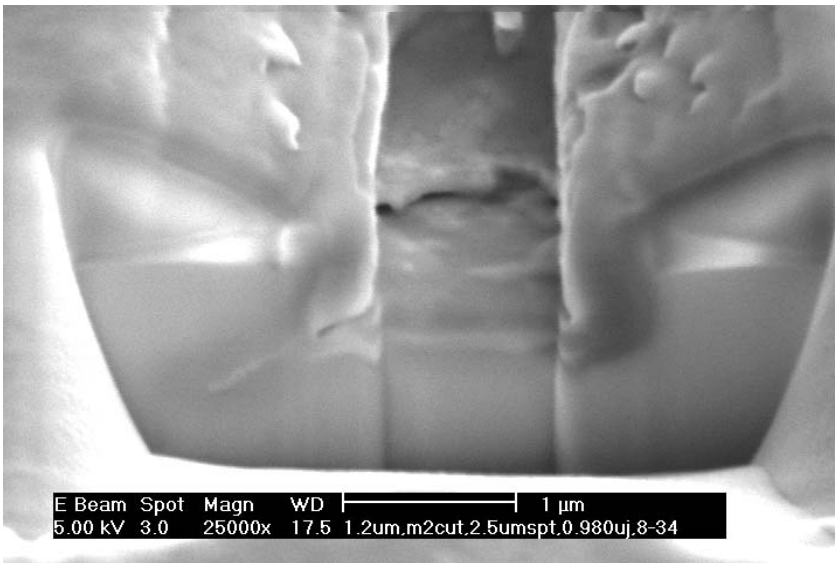

(b)

Figure 2.13: FIB cross-sectional images of laser-cut sites processed with energies above the process window, spot size: 4.25μm 1/e^2 diameter. Laser energies: (a) 0.8μJ and (b) 0.98μJ.

2.5 More Simulations Results

Various metal structure designs and laser parameters were simulated to understand their effects on laser process windows. Specifically, the effect of the metal width, metal thickness, passivation thickness, and laser pulse length on the process window were considered.

It has been reported that narrower metal line increases the probability of generating cracks from the lower-corners as well as upper-corners of Al metal line [34]. Our simulation reveals consistent results with the earlier work. The narrower the metal width, the narrower the energy process window. This is due to the fact that a wider line increases the stress difference between the upper and lower-corners. Therefore, greater laser energy can be adopted for wider metal lines without failure. Unfortunately, this is contrary to the industrial trend of decreasing the fuse pitch by using narrower lines.

Laser cut structures with different metal and passivation thicknesses were also simulated in order to determine how they influence the energy process window. Figure 2.14 illustrates the process windows obtained using various combinations of passivation and metal thicknesses. For these simulations, four different passivation thicknesses (0.2μm, 0.6μm, 1.0μm, and 1.8μm) and three different metal thicknesses (0.4μm, 0.6μm, and 0.8μm) were used.

Figure 2.14 shows that the maximum possible energy process window obtainable from these combinations is 6:1. This process window occurs when using a 0.6μm metal thickness and a 0.6μm passivation thickness. From the graph, it is also apparent that it is difficult to obtain an acceptable energy window, even using a 1.8μm passivation thickness, when adopting 0.8μm metal thickness. We can conclude that an optimal passivation thickness for a specific metal thickness,

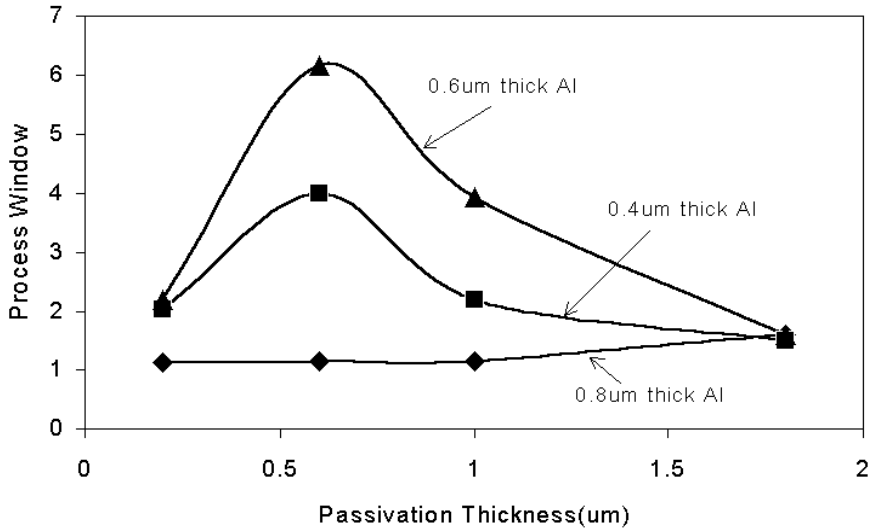

Figure 2.14: Laser energy process window with various combinations of passivation and metal thicknesses(laser pulse : 15ns).

under a specified laser pulse length, exists. From the simulations, a 0.6μm thick passivation is optimal for both 0.4μm and 0.6μm thick aluminum lines (using a 15ns of laser pulse).

There is also an optimal metal thickness for a specific passivation thickness (under specified pulse length). From Figure 2.14, it can be seen that a 0.6μm thick aluminum line is optimal for all of the passivation thicknesses that were simulated (using a 15ns laser pulse).

The results of similar simulations with laser pulse of 5ns reveal that the process windows for thin metal line and passivation layer increase. Especially, the process window for 0.4μm thick aluminum line with 0.2μm passivation layer is prominently increased. The reason for such behavior stems from the fact that the thermal diffusion length in aluminum is proportional to $\sqrt{t}$. Equation (2.1) in-

dicates a simple calculation based on the simulation results to get optimal metal thickness(T_{metal}) from the pulse length of the laser used(t_{pulse}).

$$T_{metal} = 0.167\sqrt{t_{pulse}} \tag{2.1}$$

The calculations show that 0.65μm and 0.37μm of Al line thickness are optimal for 15ns and 5ns laser pulse, respectively. Further studies are being continued to simulate other pulses consistent with more modern laser repair systems.

2.6 Discussion

Experimental observations showed obvious stress-relief at the moment of passivation breakthrough as simulated. Our experimental observations also revealed asymmetric lower-corner cracks in case of narrow metallization(1.2μm wide) after laser pulses through the various laser energies, including even very low energies(lower than passivation-break threshold energy), due to the lack of stress-relief within small aluminum structure. Improved laser positioning accuracy will help avoid asymmetric lower-corner cracks caused by biased stress development. As the metal width increased, no lower-corner crack was found at very low energy levels as well as within process window.

A shorter, or faster rise-time, laser pulse for processing can also be used to avoid this lower-corner cracking. A shorter laser pulse is desirable because it develops a steeper temperature profile within the aluminum [31]. This steeper temperature profile will increase the slope of the upper-corner stress curve(*Upper-corner*) and decrease that of the lower-corner stress curve(*Lower-corner*), in Figure 2.9, thereby resulting in a larger gap between the two (for the same instant

of time). This will cause the upper section of the structure to heat up and expand fast, thereby decreasing the stress for lower-corner cracking and accelerating upper-corner cracking.

Chapter 3

Analysis of Process Window of Pad-Cut Structures

3.1 Background

Ever since the laser cut processing has become a standard technology in industry, the improvement of cut processing has been an important issue. There have been a variety of researches focused on the optimization of cut structure as well as laser parameters. So far, the most common metal cut structure has a shape of a simple line, and sometimes a line with shrunken cutting area was used as displayed in Figure 3.1 (a) and (b).

The simple line structures, however, have small areas absorbing laser energy and large amount of energy which is not absorbed in metal will be radiated on the substrate where is not shielded by metal line. Therefore, a novel structure with extended area for cut was proposed as shown in Figure 3.2. It has a metal pad instead of a narrow line for cutting area, so the pad structure can absorb more laser energy with a smaller laser spot and less energy can escape out the thinner lines. Also, the pad structure will help avoid the laser radiation damage.

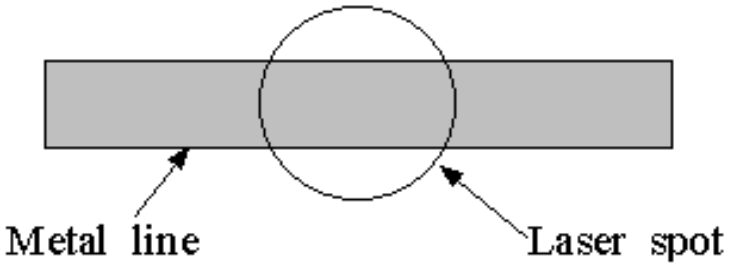

(a)

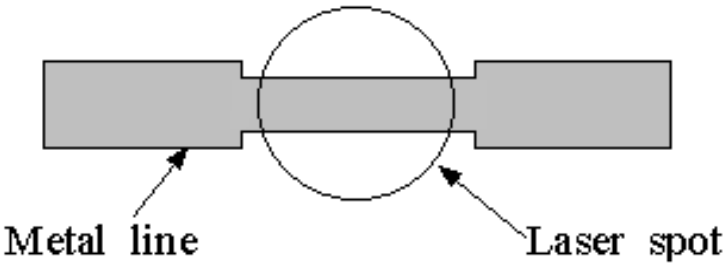

(b)

Figure 3.1: Conventional metallic line-shaped laser cut structures (a) straight line structure and (b) shrunken-cutting-area line structure.

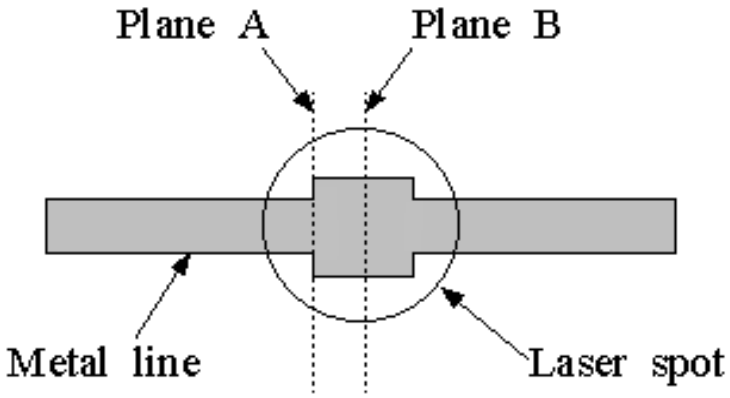

Figure 3.2: Pad-shaped laser cut structure.

Furthermore, based on experimental and simulation results in previous chapter, it is considered that the fracture across the line from the corners occurs more efficiently. In other words, the pad structure will increase the stress on the upper corner over time and trigger the cracking earlier than line structure. Hence, the pad cut structure will increases the time from upper corner cracking to lower corner cracking to make the latter less likely due to the stress-relief effect by upper-corner cracking. The theory will be detailed in this chapter with both experimental and simulation results.

3.2 Simulations

To determine the temperature in Al and stresses at the upper and lower corners of Al line during a laser pulse, a finite element model was created using MSC *Mentat* software. Figure 3.3 describes the 3-dimensional finite element model. The elements near the metal corners and along the boundary between Al and SiO_2 have smaller sizes in order to get better computation with better accuracy. This can be seen from the size of square shaped faces of elements on the top.

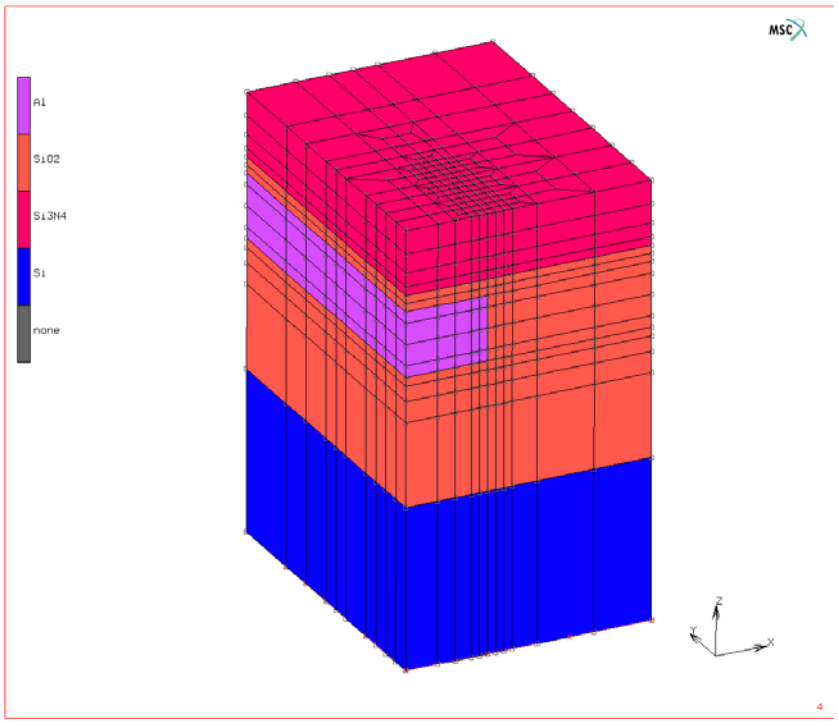

Figure 3.3: 3-Dimensional finite element model for laser-cut simulation.

The colors indicate different materials used and each material has specified material properties. For the sake of simplicity, only the four primary materials involved were included in the model: aluminum, silicon dioxide, silicon, and silicon nitride. The material properties used in the model are detailed previously in section 2.3.2.

Unlike the previous conducted 2-D finite element models, hexahedron-shaped elements were used for simulation in order to increase the accuracy of computation. On the other hand, a rough density of elements can be noticed in parts where less displacement and stress development are expected in Figure 3.3 to save computation time. Also a quarter of the whole structure was used due to the geometrical symmetry of each structure for the same reason.

Figure 3.4 displays finite element models without passivation over metal, so

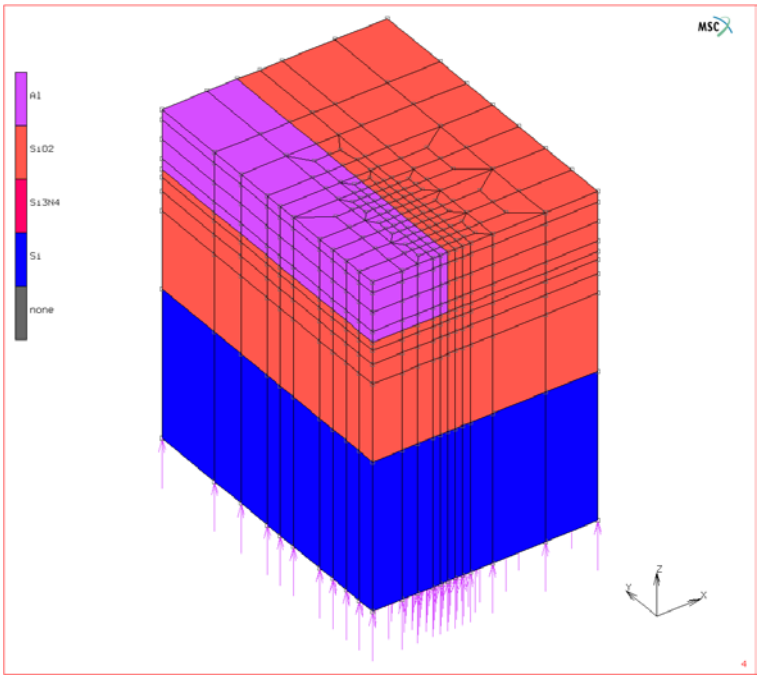

(a)

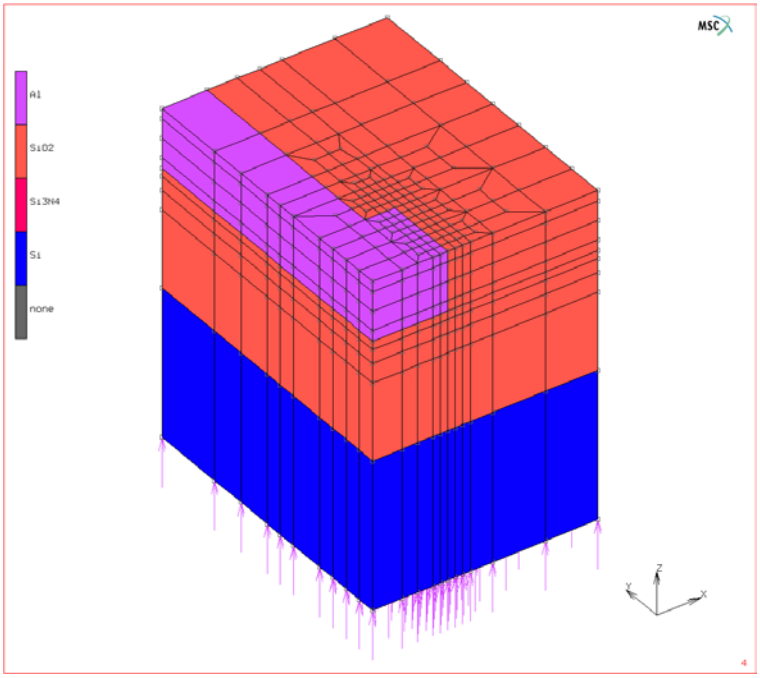

(b)

Figure 3.4: 3-D Finite models, (a) line cut structure and (b) pad cut structure.

the two different aluminum structures can be distinguished. It is noted that the width of the pad in a pad cut structure need to be the same as the width of a line cut structure in order to observe the different effects depending the structure. The simulation includes two consecutive steps; the first one is a thermal simulation step and a following mechanical simulation step using the results of thermal simulation. This is to help decrease the computation time needed for 3-D model and it does not lose the accuracy compared with a coupled simulation.

The following simulation results are based on a line cut structure with a width of 2 μm and a pad cut structure with a 2×2 μm square pad connected to 1.2 μm wide metal lines. A 1 μm thick passivation consisting of silicon dioxide and silicon nitride covering the metal link are used for the simulation to be comply with the test wafer which will be presented later in the following experimental section.

Figures 3.5 and 3.6 show the temperature profiles under a 15 ns laser pulse. Each figure consists of two curves and the upper one indicates the temperature profile on the node inside aluminum which is closest to the upper corner of aluminum from the cross-sectional view of center of laser spot (Plane B in Figure 3.2) while the lower curve indicates the temperature profile on the node inside aluminum closest to the lower corner of aluminum in Plane B. The results in Figure 3.5 are from a simple line structure while Figure 3.6 shows the results of pad cut structure.

It is noted that Gaussian distribution with 3 μm in $1/e^2$ spot size in diameter was considered for the laser spot in the simulations. The laser pulse has a peak at 3.25 ns and this can be noticed by the small shoulders on the upper corner temperature curves in both Figures 3.5 and 3.6.

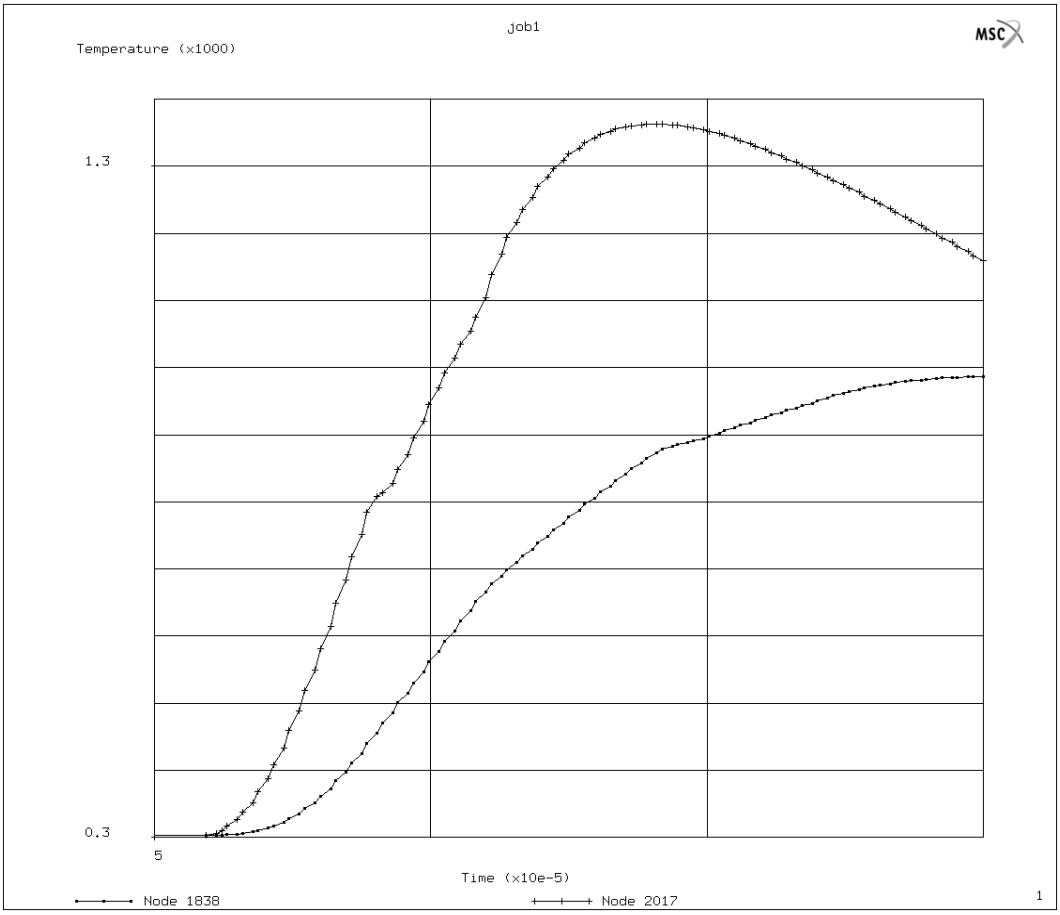

Figure 3.5: Temperature profiles at the upper and lower corners of the line cut structure in the center cross section (same spot of Plane B in Figure 3.2.

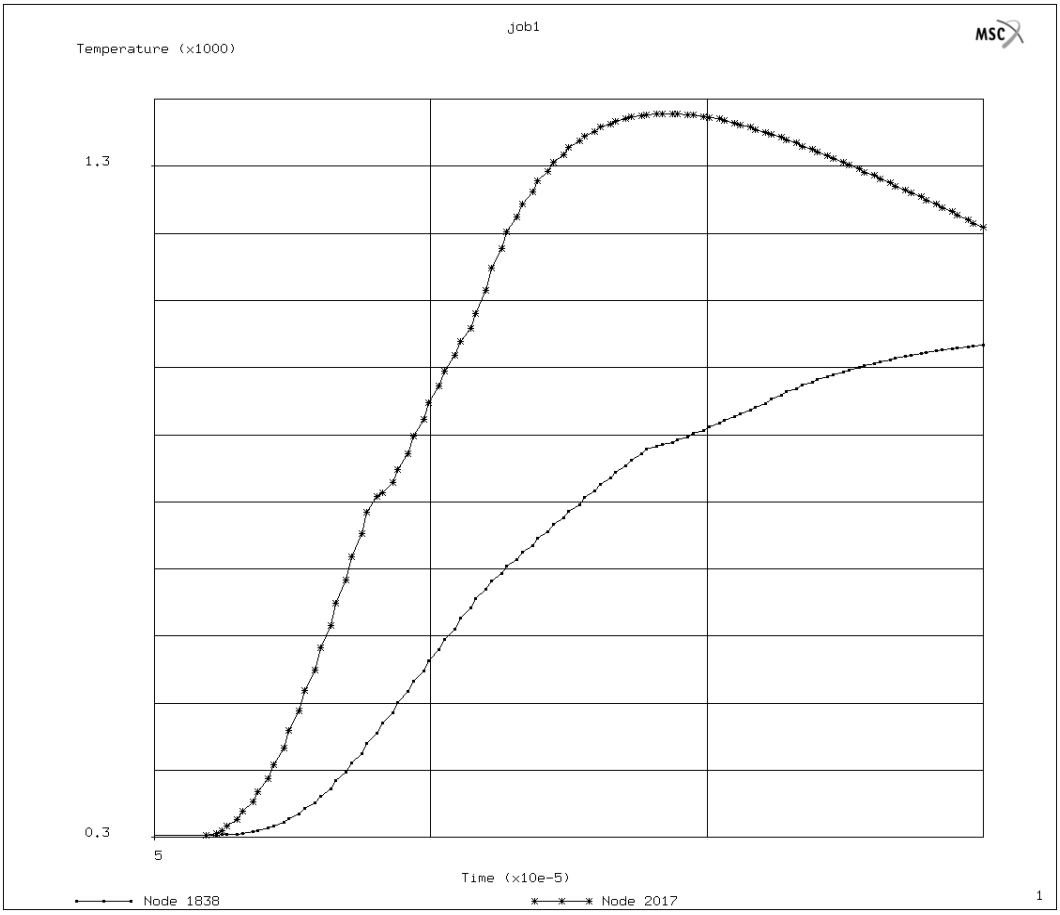

Figure 3.6: Temperature profiles at the upper and lower corners of the pad cut structure in the center cross section (Plane B in Figure 3.2.

In both cases, it is shown that the temperature curves diverge at the earlier stage of a pulse and converge again together with the prevailing thermal diffusion afterwards. There is a slight difference of temperature over time between two structure cases and the pad cut structure has a slightly higher temperatures on both upper and lower corners of aluminum over time than the line cut structure. This is a reasonable result when the thermal diffusion is somewhat limited along the thinner line in case of pad cut structure. However, it does not seem to have a significant effect on cracking.

Figure 3.8 shows temperature profiles on the upper and lower corner at the cross section of 90° angled spot of a aluminum pad (Plane A in Figure 3.2), and the curves in Figure 3.7 are from the same nodes in line structure even though there was no angle. Since those nodes were off the center of laser spot and, also, Gaussian distribution was assumed, the temperatures on the angled spots are much lower than those on the center. As was expected, the temperatures on both the upper and lower corners of pad structure are higher than those of line cut structures due to the restricted thermal diffusion along the line. In a point of upper corner temperature curve, the difference was close to 200 °C and usually upper corners show bigger difference of temperatures. Therefore, it is certain that the restricted heat diffusion along the thinner line in case of pad cut help hold more energy within the pad.

The onset of the dielectric fracture on a upper corner can be seen in Figures 3.9 and 3.10and the stress change at the moment corresponds to the abrupt release of the stress at the original crack initiation point as shown in Figures 3.11 and 3.12. The time was 5 ns after applying a laser pulse in case of Figure 3.9. The crack continues to advance along the path of stress concentration. The

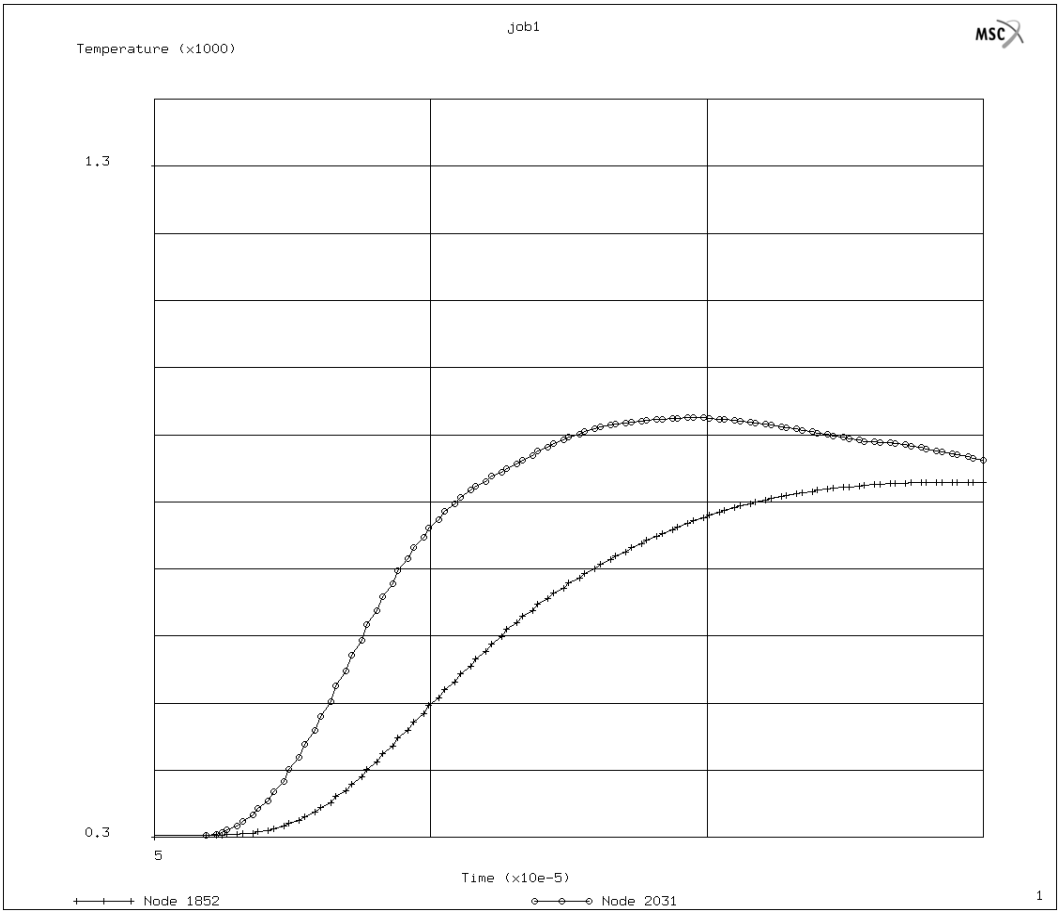

Figure 3.7: Temperature profiles at the upper and lower corners of the line cut structure in the corner cross section (same spots of Plane A in Figure 3.2).

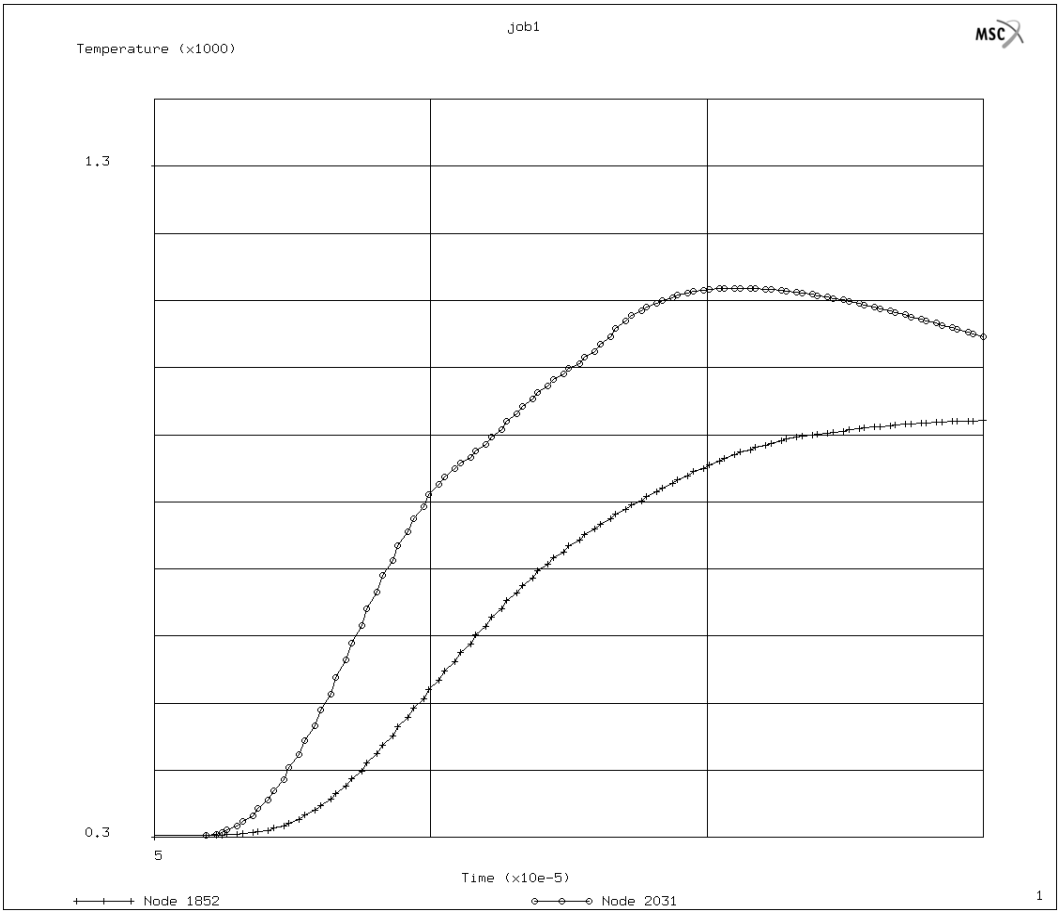

Figure 3.8: Temperature profiles at the upper and lower corners of the pad cut structure in the corner cross section (Plane A in Figure 3.2.

maximum tensile stress at the moment is always found at the crack tip and it can be located with slightly blight spot around upper corner in Figure 3.9 and it passed three elements to the right in Figure 3.10 showing the crack path. Also, the stress developed on the lower corner of metal with time can be observed in Figure 3.10. 12 ns after the application of laser pulse has passed at the moment of Figure 3.10.

Although, the crack trajectory is predicted by following the maximum principal tensile stress concentration path, the crack path in Figure 3.10 as well as the time for propagation are not realistic since the elements around the upper corner still too rough and big. This is because the 3-D simulations can include limited elements to save the computation time and it is noted that high density mesh should be created when using finite element method to predict the cracking path in brittle material. However, this is beyond the scope of this current research, so the minor error of crack trajectory will be ignored in the following discussion.

Figure 3.11 shows the stress changes at the two closest nodes to aluminum upper and lower corners in silicon dioxide in Plane B. Figure 3.11 is from the case of line cut structure and the Figure 3.12 is from pad cut structure. Compared with Figure 3.11, the stress on the upper corner of aluminum in case of pad structure shows slightly higher in every point on the curve. This was expected from the fact that the pad cut structure has a slightly higher temperatures on both upper and lower corners over time than line cut. This will result in the faster fracture on the upper corner in Plane B in case of pad structure than that of line structure. The slightly higher stress profile was also noticed at the lower corner of pad structure.

The stress developments on upper and lower corners in Plane A were simulated

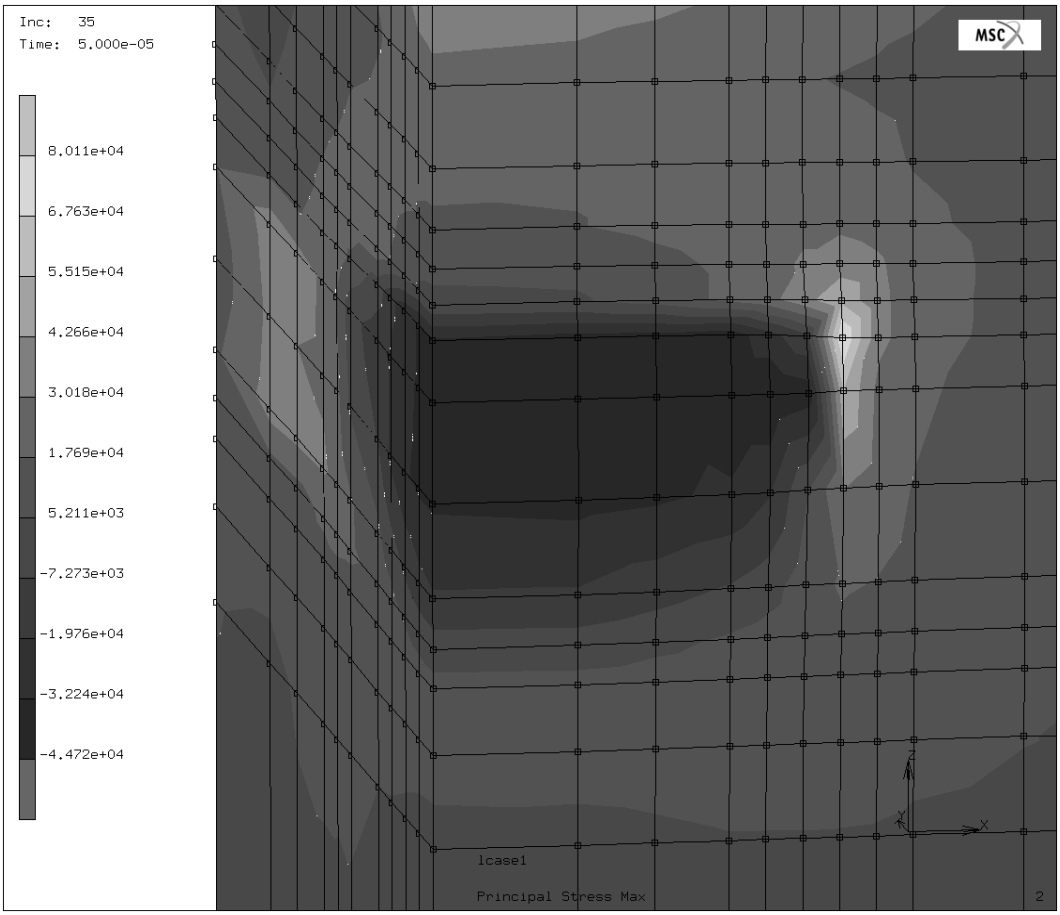

Figure 3.9: Contour pictures of the maximum principle stress for the line cut structure at a time of 5 ns.

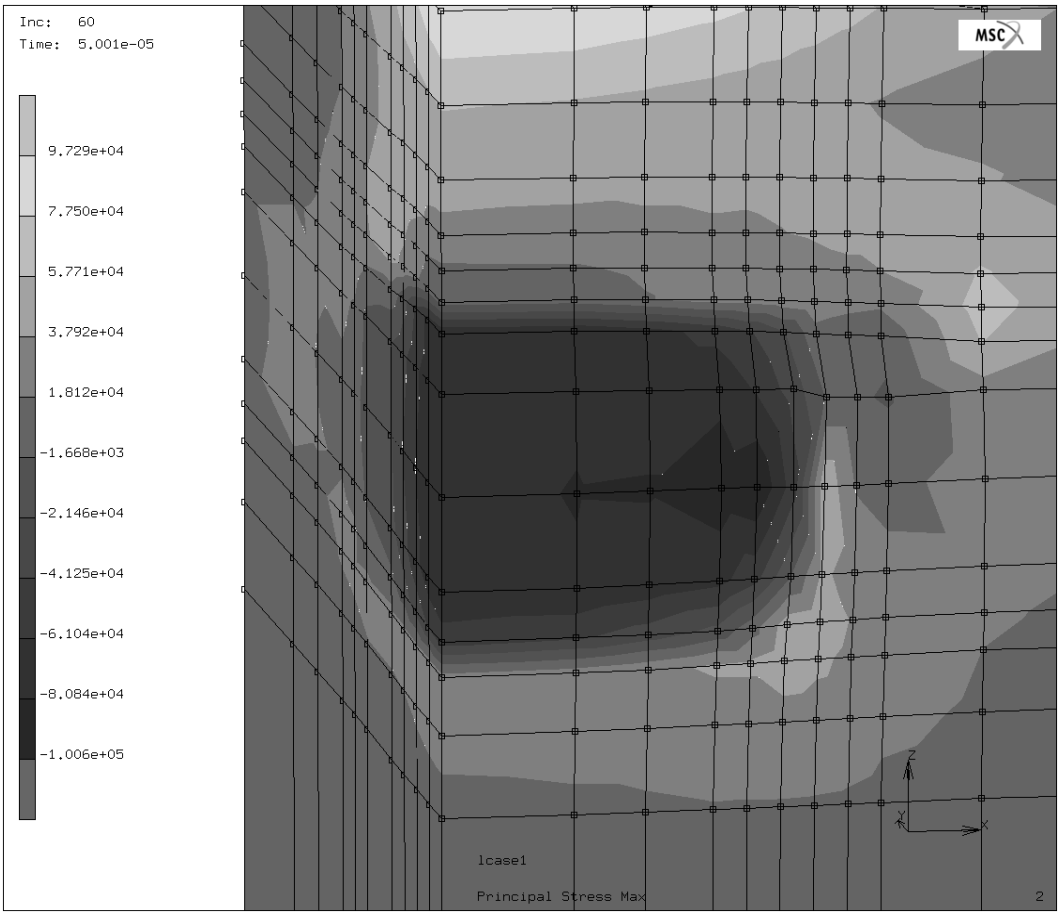

Figure 3.10: Contour pictures of the maximum principle stress for the line cut structure at a time of 12 ns.

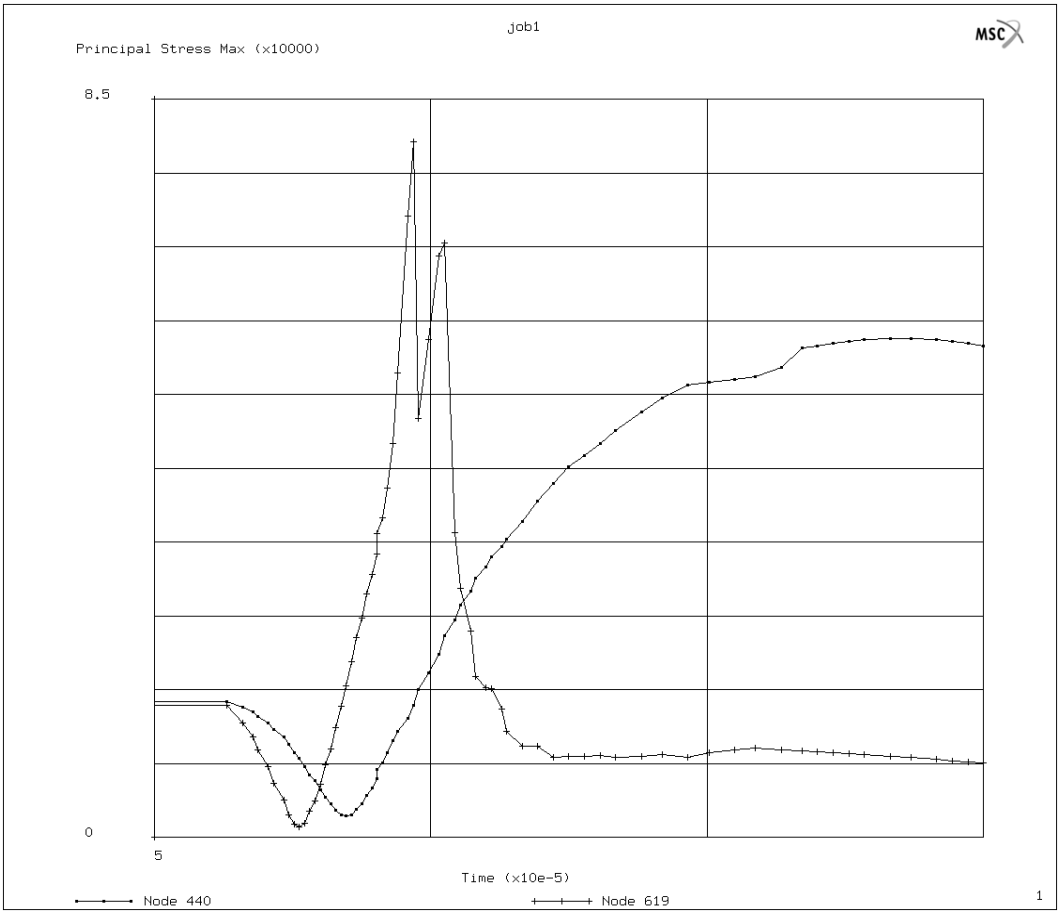

Figure 3.11: Stress profiles at the upper and lower corners of the line structure in the center cross section (Plane B).

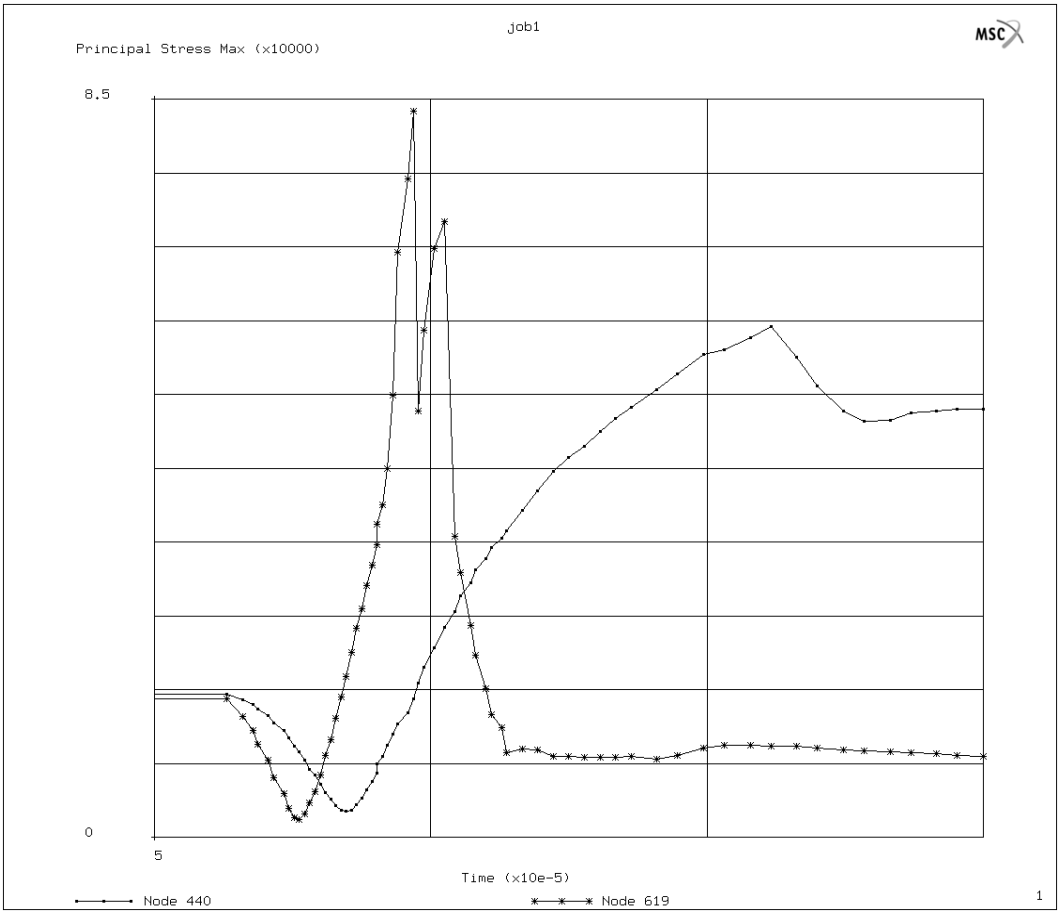

Figure 3.12: Stress profiles at the upper and lower corners of the pad cut structure in the center cross section (Plane B).

for both structures and the results are displayed in Figures 3.13 and 3.14. It is shown that the stress on the upper corner in Plane A of pad structure developed fairly faster than that of line structure and concluded with earlier fracture on the upper corner. The difference between the two stresses on the upper corners for both structures is larger than the case of Plane B and this indicates less thermal diffusion along the thinner line in the case of the pad structure. Also, it is certain that the geometry with an angle in the case of pad structure definitely helped the higher stress development on the upper corner in Plane A.

It is interesting to see the changes of stresses on lower corners for both cases. In the beginning stage of laser pulse duration, up to the first 5 ns, the stress on the lower corner of pad structure , as can be seen in Figure 3.14, was lower than that of line structure. This is due to the residual stress from fabrication. As time goes on, the stress on the lower corner of pad structure developed faster than that of line cut structure (Figure 3.13 and prevailed for 2 ns. After that, the two curves cross again each other and the lower-corner stress of line structure prevails. From the Figures 3.7 and 3.8, the temperatures in both nodes of pad structure was higher than those of line structure throughout the laser pulse. Nonetheless, the lower-corner stress of pad structure is much less than that of line structure after the first 7 ns of the laser beam radiation. As a result, the lower corner stress was relieved faster in the case of the pad structure than the case of line structure and this will help increase the process window. As mentioned earlier, it is noted again that the increase of time interval from upper corner cracking to lower corner cracking is beneficial to increase of process window since it will make the lower corner cracking less likely.

From the 3-D simulation, the cracking was found to initiate from the upper

corner in Plane B first and propagate to along the edge of upper corner during the propagation in dielectric to the free surface.

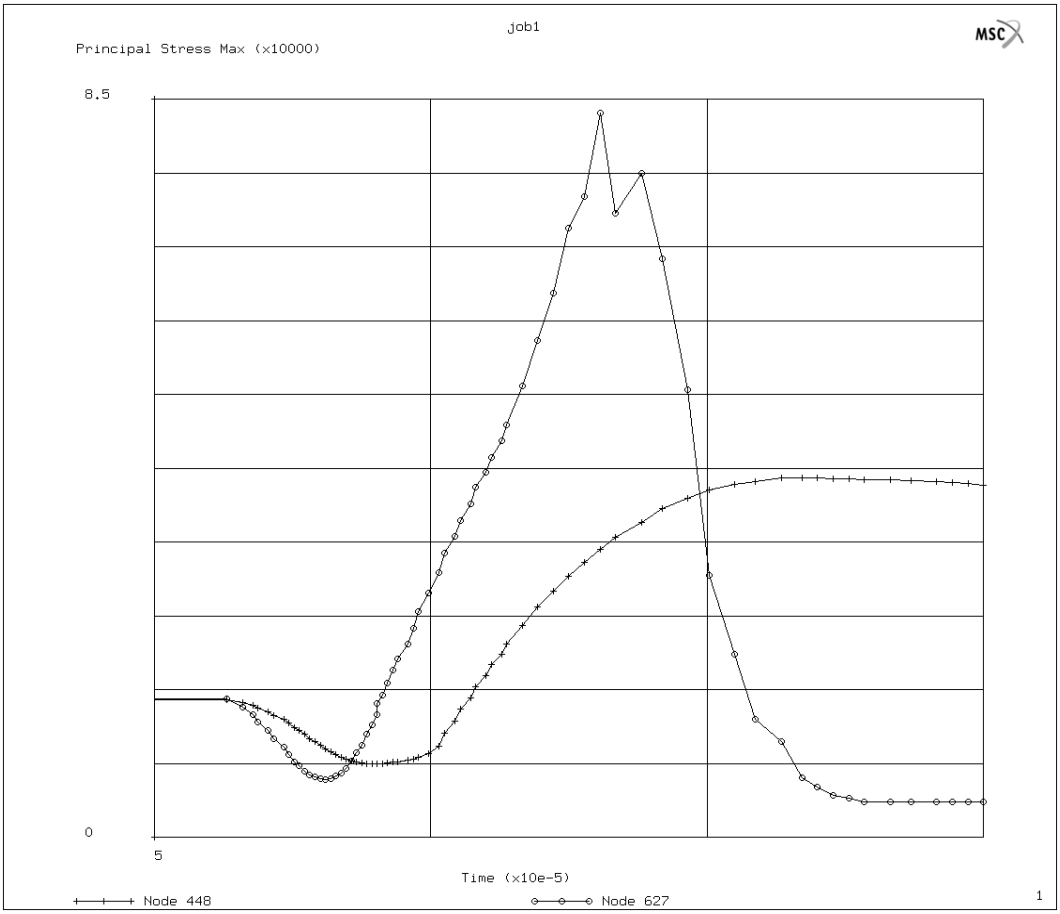

Figure 3.13: Stress profiles at the upper and lower corners of the line structure in the corner cross section (Plane A).

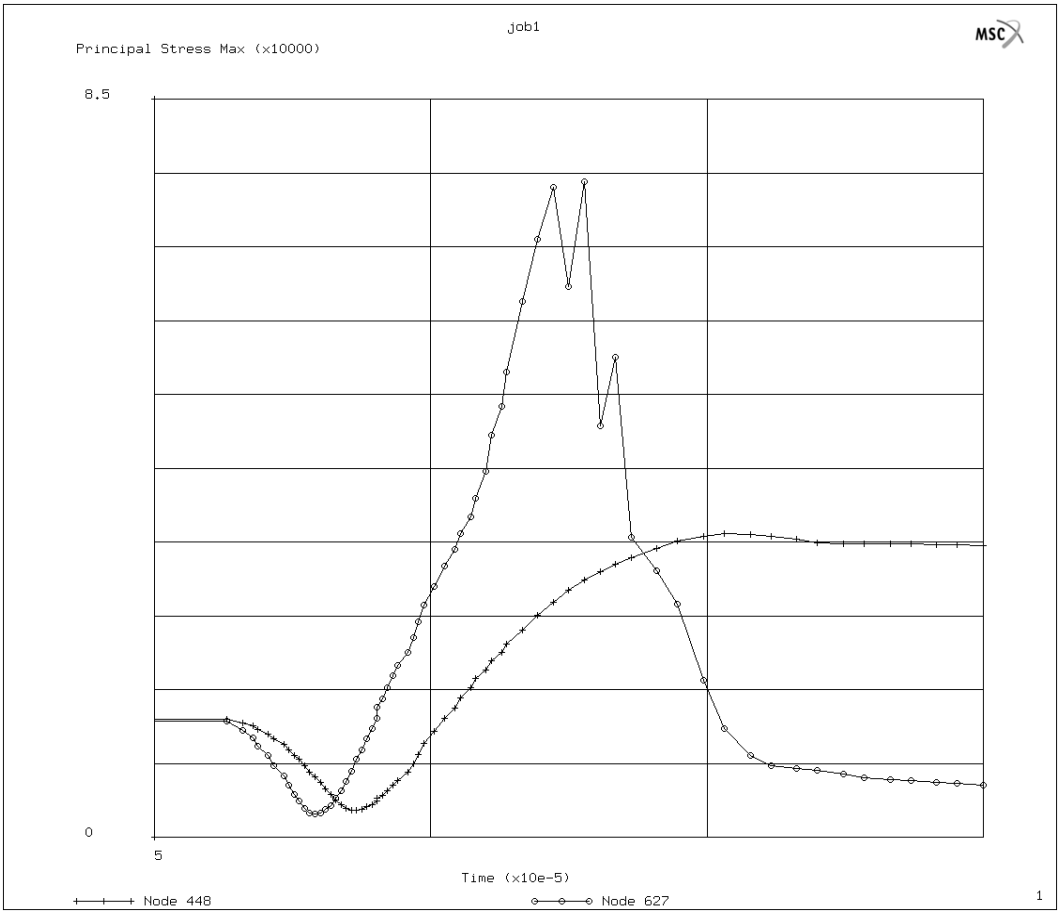

Figure 3.14: Stress profiles at the upper and lower corners of the pad structure in the corner cross section (Plane A).

3.3 Experimental Observations

The sample metallization are aluminum based with 1% silicon and 0.5% copper. The thickness of metal was 0.8 μm and it was deposited on silicon dioxide deposited on the silicon substrate. The metal lines used in this experiment were two different structures, line cut structure with a width of 2 μm and pad cut structure with 2×2 μm pad connected to 1.2 μm wide line in order to be consistent with simulation results.

In this study, the laser spot size defined to be $1/e^2$ diameter set to 4.25μm. Two kinds of metal line, line and pad structure, was zapped at a series of energies using XRL laser system with an IR wavelength of 1.047 μm.

Figure 3.15 (a) shows the cross-sectional view of a metal line cut link processed with a laser energy of 0.095 μJ. The energy was not high enough to cause any cracking in dielectrics. Unlike the results described in Chapter 2, this figure displays no lower crack at low energy due to the large dimension of metal link. The result of using higher energy laser pulse to process is displayed in Figure 3.15(b). This figure illustrates the effect of using a laser energy of 0.11 μJ and the successful break of passivation by thin crack from left upper corner of aluminum. Small initiation of right upper crack can be also observed. This energy used to process this cut site is right above the passivation-break-threshold energy.

Figure 3.16(a) shows the cross-sectional view of a metal pad cut link processed with a laser energy of 0.05 μJ, which was the lowest energy the laser system can get. At this low energy, upper corner cracking was initiated and reached the free surface on the right corner. Compared with the results of line cut link processed with 0.095 μJ shown in Figure 3.15(a), the crack initiated at much lower energy and this indicates pad structure helped start the cracking earlier

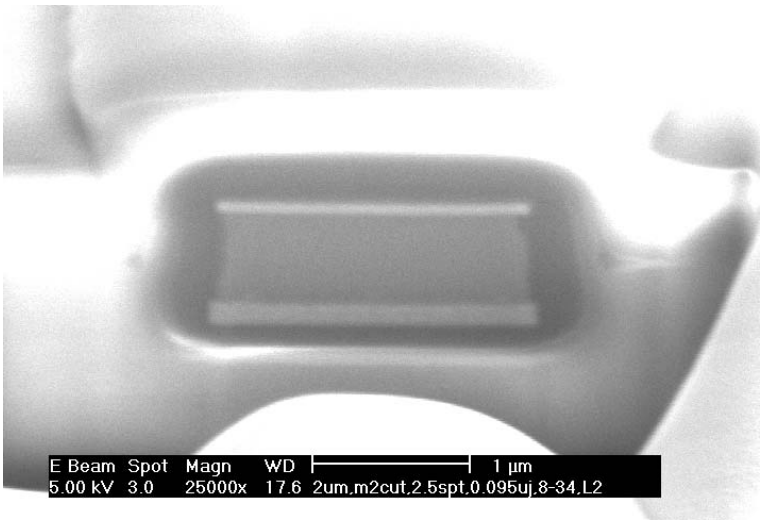

(a)

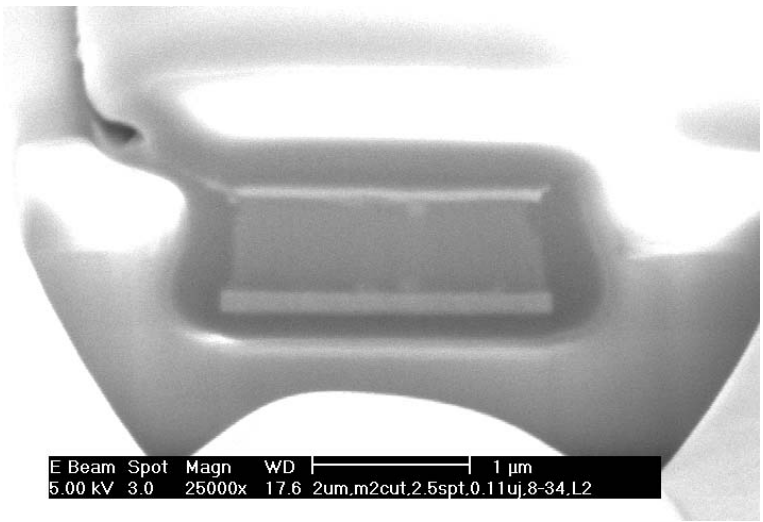

(b)

Figure 3.15: FIB cross-sectional images of line cut structures processed with energies below the cracking initiation energy to the passivation-break threshold energy, spot size: 2.5μm FWMH diameter. Laser energies: (a) 0.095μJ and (b) 0.11μJ.

than line structure. More reserved energy within the pad due to thinner line definitely heat up the metal and developed higher stresses on upper corners as shown in simulation results.

The result of using higher energy laser pulse to process is displayed in Figure 3.16(b). This figure illustrates the effect of using a laser energy of 0.11 μJ and this energy was the passivation-break-threshold energy in the case of line structure. Even though the laser energy used was the same as the case of the link cut structure shown in Figure 3.15, the difference is noticeable. Voids caused by metal flow around the top part of metallization as well as the successful break of passivation by metal expansion can be seen clearly. Small initiation of left upper crack can be also observed and this asymmetrical cracking is considered to be attributed to the laser offset.

Figure 3.17 and 3.18 present SEM images of top view of processed cut sites with a series of energy run in order to calculated average passivation rupture energy for each structure. A energy of 0.195 μJ $\pm$ 0.000122 was calculated as the average passivation rupture energy for processed line-cut structures shown in Figure 3.17 and 0.176 μJ $\pm$ 0.000109 for pad cut structures shown in Figure 3.18. Other structures with different dimension were also measured and the detailed discussion will be presented in next section.

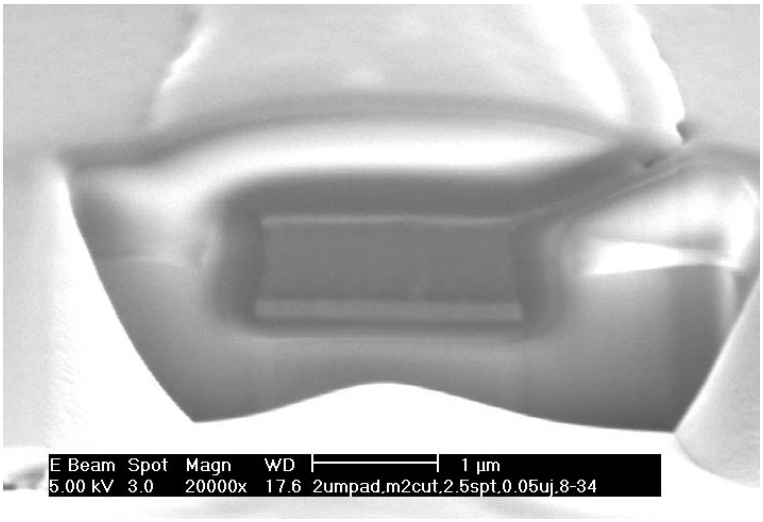

(a)

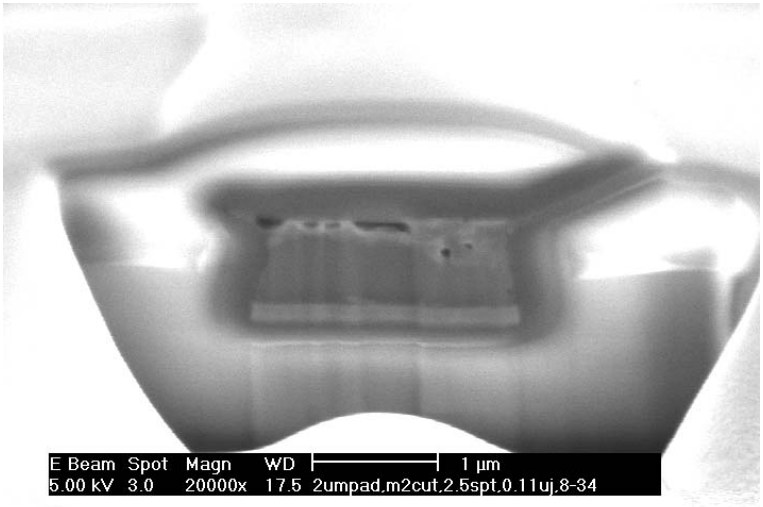

(b)

Figure 3.16: FIB cross-sectional images of pad cut structures processed with energies above the cracking initiation energy, spot size: 2.5μm FWMH diameter. Laser energies: (a) 0.05μJ and (b) 0.11μJ.

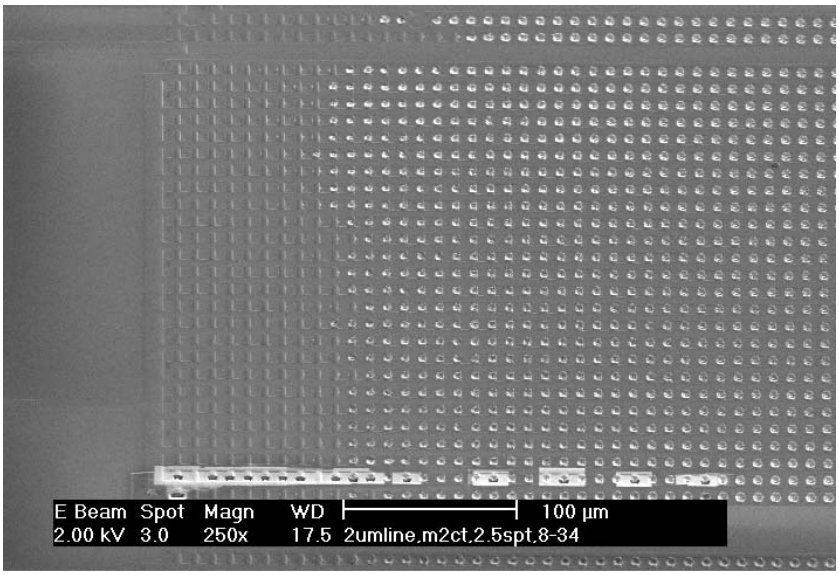

Figure 3.17: Top view of laser-processed cut sites, 2μm wide line cut structure, laser energy started from 0.05μJ at the far left site and increased by 0.015μJ every one site to the right.

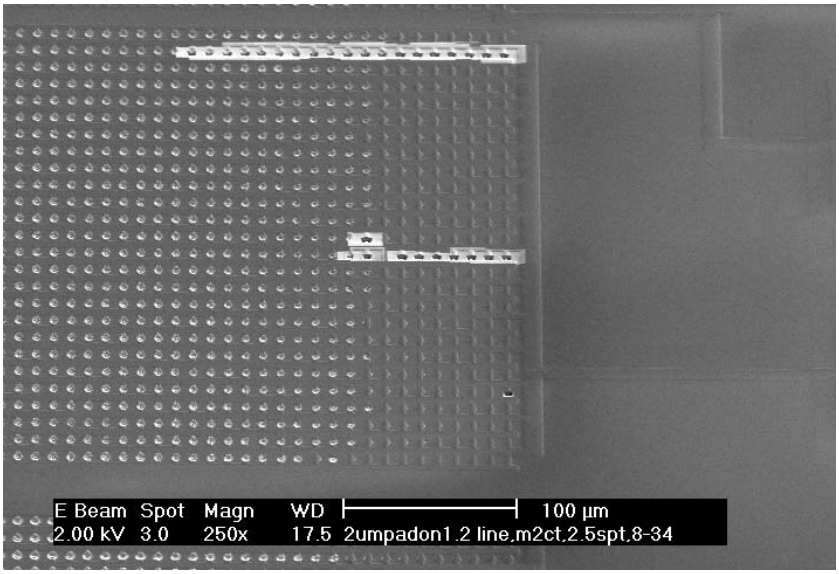

Figure 3.18: Top view of laser-processed cut sites, pad cut structure with 2×2μm pad on 1.2μm line, laser energy started from 0.05μJ at the far right site and increased by 0.015μJ every one site to the left.

3.4 Discussion

Experimental observations showed obvious shifts of both cracking and passivation-break-threshold laser energies to lower levels for the cases of pad cut structures. The 3-D simulation results showed the initiation of passivation cracking occurs in the center part (Plane B) and the cracking is observed to be delivered along the edge of line in both structures. Therefore, the earlier cracking seems to stem only from the fact that the pad cut structure absorbs more laser energy since less can escape out the thinner line.

Considering the simulation results, the stress difference between two different structures reflects the temperature difference effects much more than the geometry effects. This is because the cut link dimensions used in simulations were too small and it didn't have enough impacts on the stress development results. In addition, the big and rough element size is considered to keep the computation from getting accurate results.

However, the higher upper corner (both in Plane A and B) stress curves in case of pad cut structure indicate the earlier cracking of upper corners than line cut structure even if slightly . In addition, big shifts of cracking and passivation rupture energies based on experimental observations imply the geometry with angle (pad), along with the effect of restricted thermal diffusion, had more effects on the cracking initiation energy.

One more thing needs to be noted. The temperatures in any nodes of pad structure were higher than those in the same nodes of line structure throughout the laser pulse as can be seen in Figures 3.7 and 3.8. Nonetheless, the lower-corner stress of pad structure, in Figure 3.14, was relieved faster than that of line structure in Figure 3.13 after the first 7 ns of the laser beam radiation. This help

increase the time from the upper corner cracking to lower corner cracking and thereby, avoiding the lower cracking under the laser beam with high energy.

Table 3.1 shows the threshold laser energy for cracking on a upper corner and passivation break for the cases of various pad cut and line cut structures. The results also show the shift of critical energies to low levels in the case of pad or thinner line structures, and they are consistent with the previously mentioned explanations. Structures with narrower lines connected to the same size pad show lower threshold energies and this explains the importance of thermal diffusion along the line.

Table 3.1: Critical laser energies comparisons of line cut and pad cut structures.

Geometry	Average energy of cracking initiation (μJ)	Average energy of passivation rupture (μJ)
2μm wide line	0.11	0.195 $\pm$ 0.000122
2×2μm pad on 1.2μm line	0.05	0.176 $\pm$ 0.000109
3×3μm pad on 2μm line	0.155	0.218 $\pm$ 0.000474
3×3μm pad on 1.2μm line	0.125	0.198 $\pm$ 0.000246
4×4μm pad on 2μm line	0.194	0.275 $\pm$ 0.000558
4×4μm pad on 1.2μm line	0.179	0.246 $\pm$ 0.000107

When we calculate the ratio of passivation-rupture energy to the cracking initiation energy the in cases of various pads connected to 1.2 μm line, it shows decreasing trend with a increase of pad size. They are 0.126, 0.073 and 0.067 for 2×2, 3×3 and 4×4 pads, respectively. Pads connected to 2 μm line also show approximately the same trend. This shows that the energy difference between the cracking initiation and passivation rupture gets smaller and the time from

crack initiation to passivation-break gets shorter with a increase of the pad size. The smaller ratio of passivation rupture energy to the cracking initiation energy, the more desirable and reliable the cut process is.

Chapter 4

Analysis of Laser Cut Process of Cu Fuse

4.1 Introduction

Copper has expanded its usage as metallization in semiconductor industry due to it superior material properties to any other metals. Usually, the fabrication method of copper metallization is different from the typical fabrication to form aluminum metal line, so it is considered that the mechanical phenomena under laser heat is not exactly the same as that of Al fuse.

Also, there has been found some difficulties in the laser processing of Cu fuse. The problems are considered to stem from the different material properties of Cu, such as lower CTE than that of Al and higher melting point than Al.

On the other hand, there have been efforts to increase the process window for reliable cuts using various wavelength laser. A short green laser wavelength of 0.532μm has been tried for cut link process [40]. In spite of the better optical coupling efficiency in the metal links of the green laser energy, the overall processing results by the 0.532μm laser beam were not any better than that by 1.047μm laser for both poly-Si and metal links. Smaller absorption depth of link material at the 0.532μm laser was blamed for the poor results based on the criterion of

temperature distribution uniformity within the link [40].

Y. Sun worked on the available laser wavelength with less damage on the Si substrate and realized that the reduction of light absorption with Si longer than the wavelength of 1.2μm while the absorptive behaviors of most metals do not change much within the wavelength range from 1 to 2 μm [16]. He suggested to use laser wavelengths longer than 1.2μm to increase the higher bound of process window.

In this work, the laser blowing processing of copper fuse is explored briefly through experimental energy runs and SEM image observations. Also, the processing of the 1.340 μm wavelength laser is studied and compared with the case of processing using 1.047 μm wavelength laser.

4.2 Fabrication Steps and Structure of Cu Fuse

The test wafer used for the analyses of blowing of copper fuses described in this chapter was fabricated by using a commercial metal CMOS process. The metallization was formed from 100% copper. The followings describe the detailed fabrication process of the test wafer.

Before the deposition of Cu, 0.6 μm of SiO_2 was deposited on the SiO_2 field oxide, which was thermally grown on the silicon substrate, using tetraethylorthosilane (TEOS)-based plasma enhanced chemical vapor deposition (PECVD) at 400 °C. A 0.07 μm thick layer of SiN (Si_3N_4) was deposited on the SiO_2 layer to control the later etching process of trenching for Cu metallization. 1 μm of SiO_2 was deposited again and this layer was patterned and etched down using dual trench damascene process.

TaN was deposited to form a 0.045 μm thick barrier layer followed by the

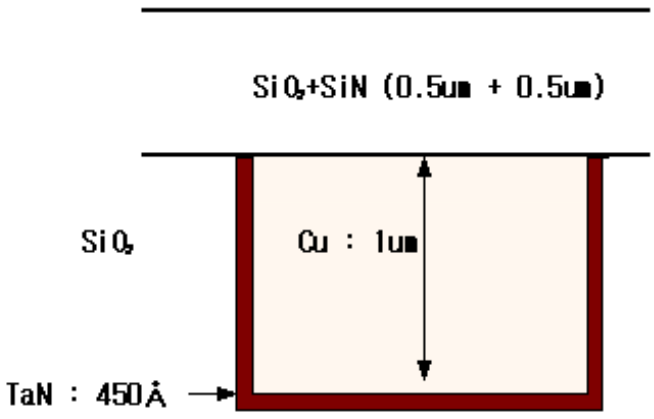

Figure 4.1: Schematic of cross-sectional view of Cu fuses.

etching process and, then Cu was deposited to fill the trenches for metallizations using Electro Deposition. Chemical Mechanical Polishing (CMP) has been performed to form a 1 μm thick and 0.77 μm wide Cu metallization. Due to the CMP processing, the cross section of the metal fuse possesses a rectangular geometry with flat top surface as can be seen in Figure 4.2 in spite of the difficult copper processing.

Dielectric layers in the order of 0.07 μm of SiN (diffusion barrier layer), 0.5 μm of SiO_2 and 0.5 μm of SiN from the top of metallization were deposited at 400 °C using PECVD after CMP. Therefore, the metallization was coated with SiN sandwiched between two SiO_2 layers and the thickness of the whole dielectric passivation over metallization was around 1 μm. Figure 4.1 shows the schematic of cross-sectional view of Cu metallization surrounded by dielectrics.

It is noted that two different dielectric layers which are deposited each right

under and on the metal layer, SiO_2 and SiN, are not sticky enough each other, so they are easy to peel off upon tensile stress. Furthermore, the CMP process makes the peeling even easier. Consequently, it is certain that there is weakness against tensile stress near lower and upper corners of metal lines.

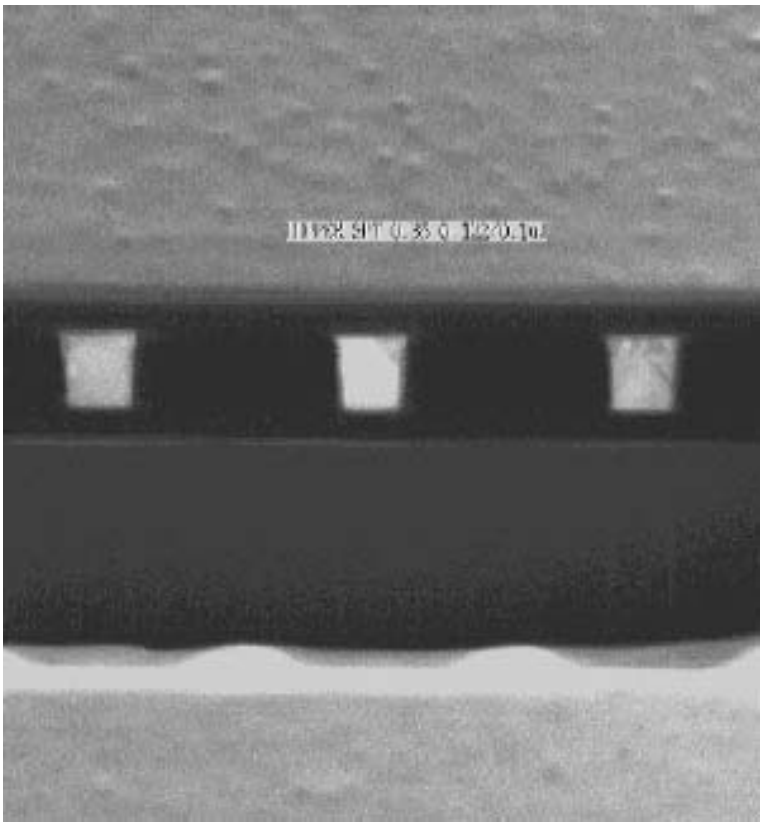

Figure 4.2: Cross-sectional view of Cu fuses before laser processing.

Cu has a 8.96 g/cm^3 of density at room temperature, melting point of 1083.4°C at atmosphere and a very high thermal conductivity, 385W/mK. Compared with aluminum, copper has a lower thermal expansion coefficient and this is thought to delay the cracking on corners. However, it is noted that Cu has a higher Young's modulus, 110 GPa, than Al and this will contribute the compensation of lower

thermal expansion coefficient in aspect of cracking.

Figure 4.2 shows the cross-sectional image of Cu links before laser processing. The center fuse in the figure was zapped with a very low laser energy of 0.123 μJ, and it shows no big difference compared with the other two unzapped fuses except for the grain size.

4.3 Experimental Observations

4.3.1 Cut Processing by 1.047μm Laser

Basically, the laser processing of Cu fuse has the same mechanism as that of Al fuse blowing. Once the laser impinges on the target which is the top of Cu link with passing through overlying dielectric layer of SiO_2 and SiN, metal heats up and expands, thereby developing tensile stress on the upper corners of Cu metal line.

When the tensile stress reaches the critical stress of dielectric, cracks initiate and propagate within dielectric perpendicularly to the local maximum principle tensile stress. However, the dielectric layer has the weakness point around the upper corners due to the CMP process as well as the boundary between SiN and SiO_2, so the critical stress for cracking is considered to be lower than that of previously detailed aluminum fuse. Therefore, the cracks tends to take a different path which follows the weak boundary. This is shown well in Figure 4.3. Figure 4.3(a) is an image of a link processed with a 0.192μJ laser energy. The spot size was 3.5 μm in $1/e^2$ diameter throughout the whole processing covered in this chapter.

It is clearly shown that cracks initiated from the upper corners of metal line

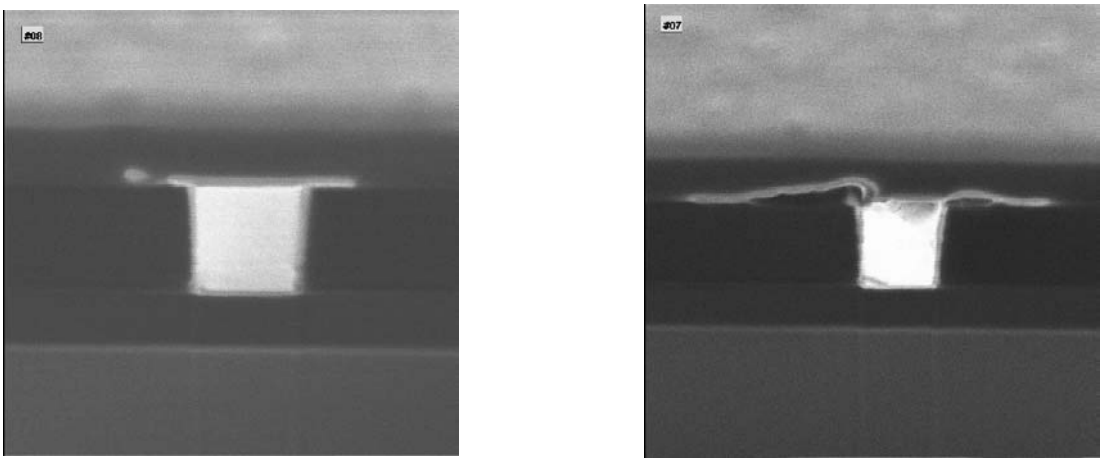

(a) (b)

Figure 4.3: FIB cross-sectional images of laser-cut sites processed with energies below the passivation-pop-off threshold energy. (a) laser energy: 0.192μJ, and (b) laser energy: 0.215μJ.

and propagated in parallel direction due to the aforementioned reason. There is no lower corner crack, which was observed in the analysis of Al zapped with low energy, in spite of the boundary layer right under Cu links and this is because of the TaN barrier layer covering the metal line. TaN layer is hard to break and, thereby preventing the lower corner from cracking in spite of whole melting of metal to the bottom. In addition, Si substrate beneath the metal line helps prevent from lower cracking.

In Figure 4.3(b), the cracks are larger and longer than the those in Figure 4.3(a) because of the higher laser energy used. The energy was 0.215 μJ and it seems to initiate the cracks in the direction perpendicular to the local maximum tensile stress. However, the crack direction has been changed along the boundary of two dielectric layers. It is thought that the hard SiN passivation layer also

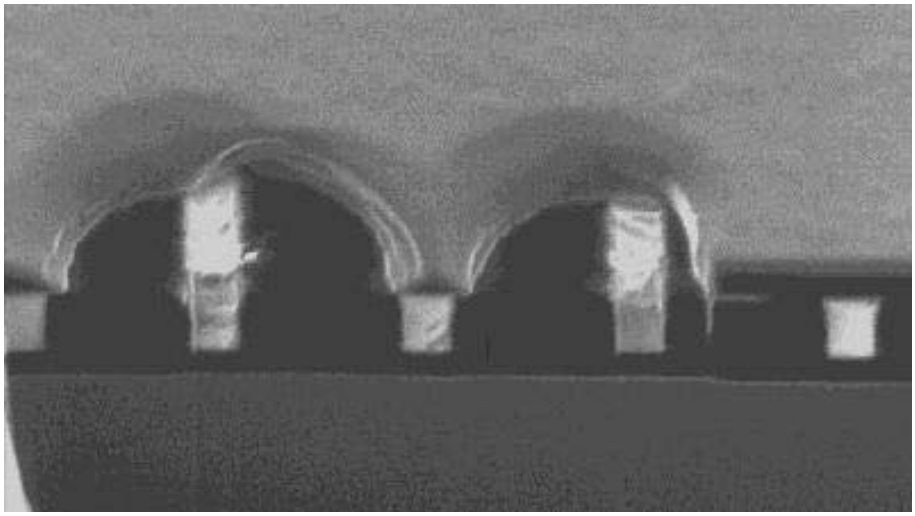

Figure 4.4: FIB cross-sectional images of laser-cut sites processed with energies below the process window. ; laser energies: 0.261μJ and 0.238μJ from the left.

help change the direction of cracks.

Laser beam is thought to have been offset to the left since the image displays the left side crack is larger and steeper than the right one. Still, the laser energy was not enough to break the passivation and reach the free surface.

From the two figure in Figure 4.3, it is clear that the Cu blowing process is initiated by the upper corner cracking just like Al blowing. Also, we are able to predict that the lateral linking between two metal lines on the same level will work perfectly with Cu metallization with the same fabrication steps by observation of the direction of cracks.

Figure 4.4 displays the cross-sectional view of cut sites processed with laser energies higher than the threshold energy to pop off the passivation. In these cases, the laser energies used were 0.238 μJ and 0.261 μJ for right and left one respectively.

Although the passivation was popped off, the laser energies was not enough to get reliable cuts. In the analysis of Al processing, it was mentioned that the chance to have lower corner cracks decreases when the cracks break the passivation break and blow away. This result should be consistent with the case of Cu blowing process. Furthermore, the metal is covered by TaN barrier layer, even without considering thermal conductivity or CTE of Cu, so the chance is even less than the case of Al link. Metal remaining at the cut sites indicates unreliable cut and reveals the upper corner cracking was initiated and propagated to the free surface (thereby initiating the explosion) well before the entire metal structure was able to melt.

The figure shows wide craters caused by the passivation explosion compared with the case of Al rupture. The physical characteristics from the fabrication process can also provide hints about the big size of crater, which is two different layers of SiN and SiO_2 and CMP. Upon the laser beam, the cracks initiated on both sides of upper corners and propagated following the weakest point near upper corners; thereby producing big cavities.

Figure 4.5 shows the top view of cut sites processed with laser energies from 0.284 μJ (right top one), to 0.537 μJ (left bottom one). The energy range shown in this figure is below the lower bound of process window for reliable cuts and metal remaining can be observed clearly.

The decrease of metal remaining at the bottom of metal line can be seen with the increase of laser energy. The craters after passivation explosions are large throughout all the processed links. Also, metal debris near each of the cut sites can be observed. It seems that there is no big difference of cavity size depending on laser energy as long as the passivation explodes.

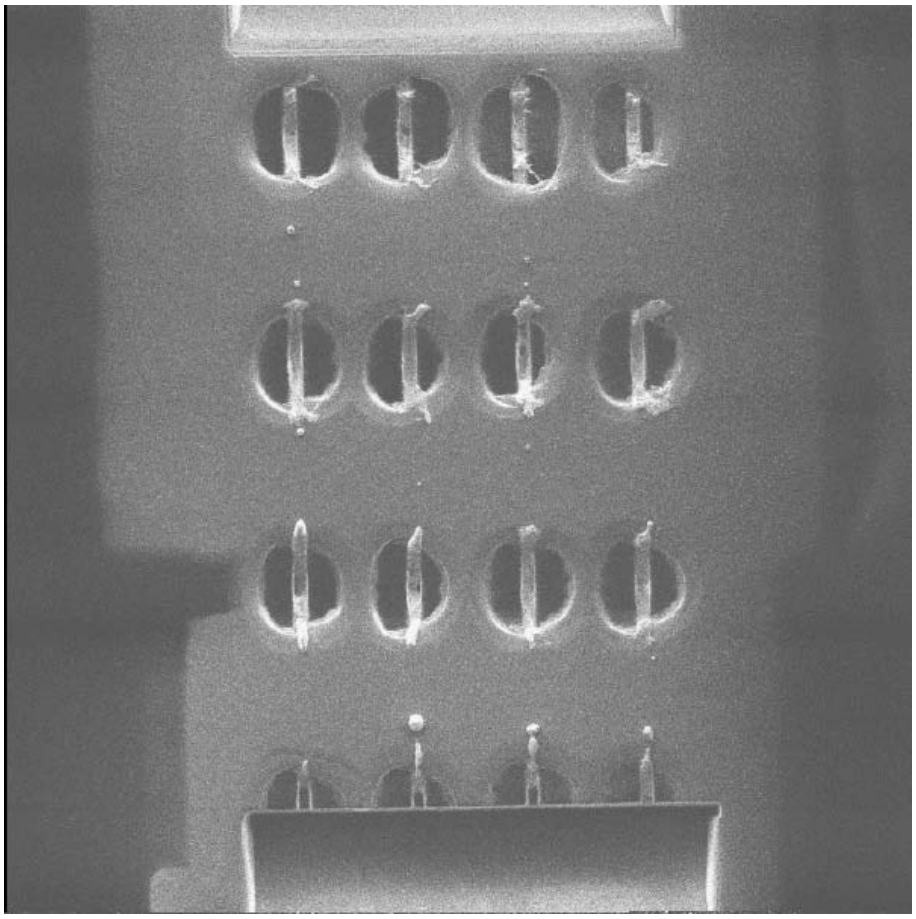

Figure 4.5: SEM image of top view of laser-cut sites processed with various energies below the process window. ; laser energies: from 0.284μJ to 0.537μJ.

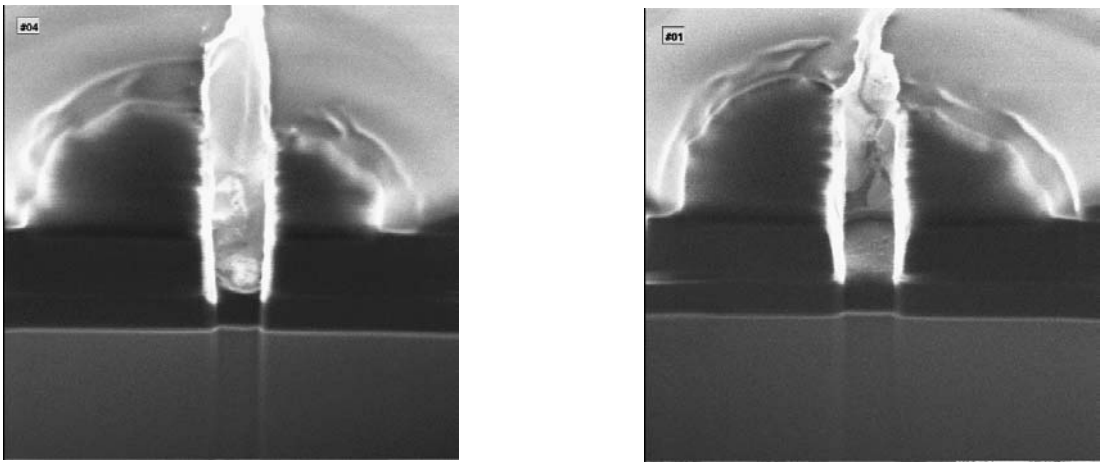

(a) (b)

Figure 4.6: FIB cross-sectional images of laser-cut sites processed with energies near the lower bound energy of process window. (a) laser energy: 0.56μJ, and (b) laser energy: 0.629μJ.

In case of Figure 4.6(a), a laser energy of 0.56 μJ was used. This is the energy right before the lower bound of process window for reliable cuts. On the other hand, a laser energy of 0.629 μJ was used to process the link shown in 4.6 (b). This cross-sectional image portrays a clean, reliable cut. All of Cu, as well as the TaN undercoating layer, was removed by the cut process. Therefore, the image indicates that the laser energy used was within the process window.

However, the cavity size becomes a critical issue when it comes to the achievement of fine fuse pitch. On the other hand, the high energy required for reliable processing also becomes significant since it will increase the chance to damage the nearby links. Consequently, the spot size of laser beam is a important issue.

These figures in Figure 4.7 illustrate the effect of using laser energies above the high end of process window. In the case of Figure 4.7 (a), a laser energy of

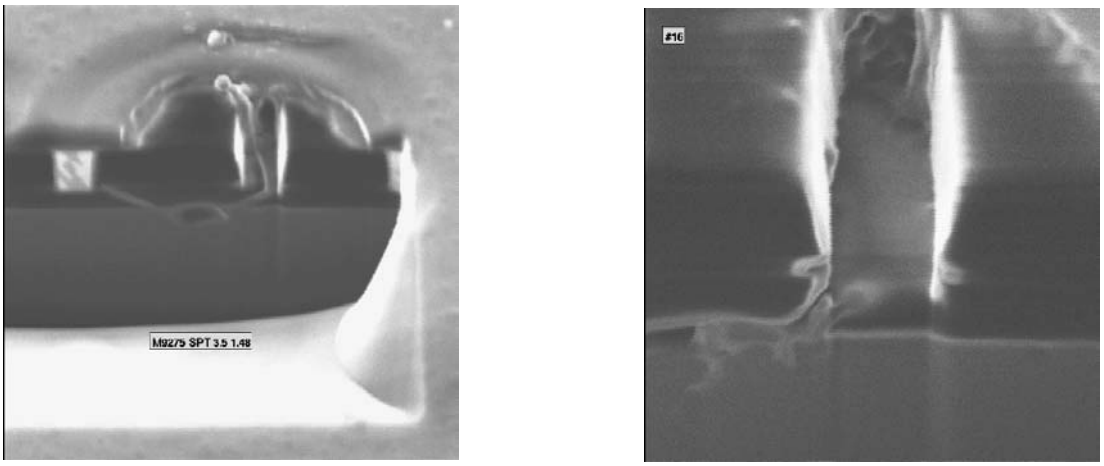

(a) (b)

Figure 4.7: FIB cross-sectional images of laser-cut sites processed with energies beyond the process window. (a) laser energy: 1.48μJ, and (b) laser energy: 1.664μJ.

1.148μJ was used. The image reveals the Si-substrate damage on the left side of link even though the link was cut clearly. This substrate damage was caused by the laser beam which did not hit the link and it pose a reliability concern because it connects the link to substrate or other link nearby.

The fissure filled with molten Si emanating from unzapped link on the left is formed by combination of Si substrate damage and lower corner cracking of the adjacent link. Although it was filled with molten Si, it is thought that the stress developed by lower corner of left side link helped the cracking due to the edge laser energy in Gaussian. Also, the damage of adjacent link can be noticed by observing the change of grain size.

The laser energy used to obtain Figure 4.7(b) was 1.664μJ. This energy is far beyond the process window. The image clearly show the small lower corner

cracks as well as big lower corner fissure connecting to Si substrate, thus it is a failed cut.

4.3.2 Cut Link Processing by 1.340μm Laser

Laser pulses with a 1.340μm wavelength were tried on the same fuse structure to analyze the dependence of cut process on laser wavelength. The laser repair system used for processing was, diode-pumped 1.3μm wavelength laser with acousto-optic Q-switch, ESI *Memory Repair System 9350*. The pulsewidth used for the processing was 9ns at 12,000Hz repetition rate. Spot size of laser beam was consistent with the previous experiment, which was 3.5 μm in $1/e^2$ diameter and the energy distribution was also the same, which was Gaussian. Laser energies from 0.12 μJ to 1.7 μJ were used for this experiment.

Figure 4.8 displays the cross-sectional views of cut sites processed with laser energies lower than the threshold energy needed to pop off the passivation. Therefore, the metal could not ejected from the cut sites. In case of Figure 4.8(a), a laser energy of 0.12μJ was used. Small tiny upper corner cracks can be seen. The cracks look more like peeling off the dielectric layer than those cracking phenomena observed in Al processing due to the aforementioned physical characteristic.

It is interesting to see the dim lower corner cracks at the cut site processed with such a low energy despite the hard TaN undercoating layer. This indicates that heating at the bottom of metal line was faster and the metal had a more uniform temperature profile vertically, thereby cracking faster than in case of cut processed with a 1.047μm wavelength laser

The laser energy used for processing of the cut site in Figure 4.8(b) was 0.186μJ. Asymmetric upper corner crack indicates the laser offset to the left and

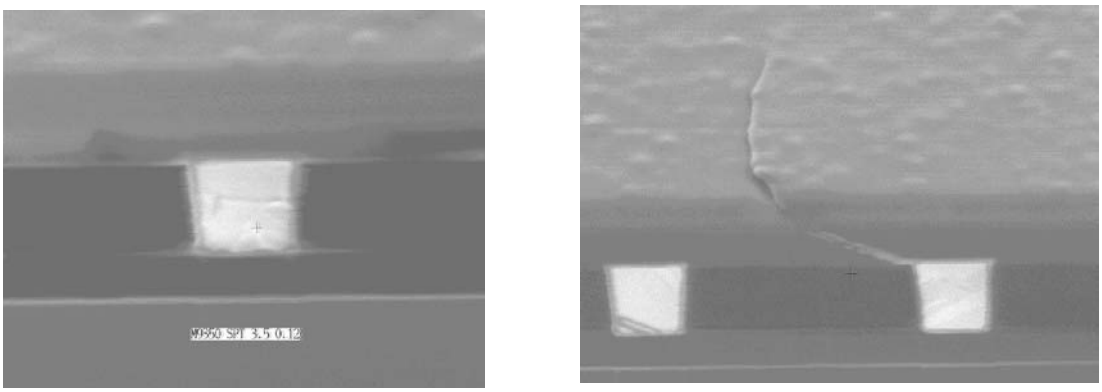

(a) (b)

Figure 4.8: FIB cross-sectional images of laser-cut sites processed with energies below the passivation-pop-off threshold energy. (a) laser energy: 0.12μJ, and (b) laser energy: 0.186μJ.

this can be noticed from the grain boundary of adjacent link. Unlike the parallel cracks formed by 1.047μm wavelength laser, the upper corner crack propagate with an angle of around 40° from the parallel line in spite of CMP processing. The cracking with this angle was shown from Al cut processing and this implies the hint that the direction of tensile stress developed on the upper corner was enough to break the passivation in 40°. In other words, the vertical temperature profile was more uniform than that of metal processed with 1.047μm laser. This phenomena will be mentioned in the discussion section.

Figure 4.9 shows cross-sectional views of cut sites processed using laser energies higher than the threshold energy necessary to pop off the passivation completely. However, the images reveal that the laser energies were not high enough to perform the cut operation. In the case of Figure 4.9, the laser energy was 0.208 μJ. Even in this picture, the steeper crack angle can be confirmed by the small cavity size compared to that in Figure 4.4. Figure 4.9(b) is an image of cut site

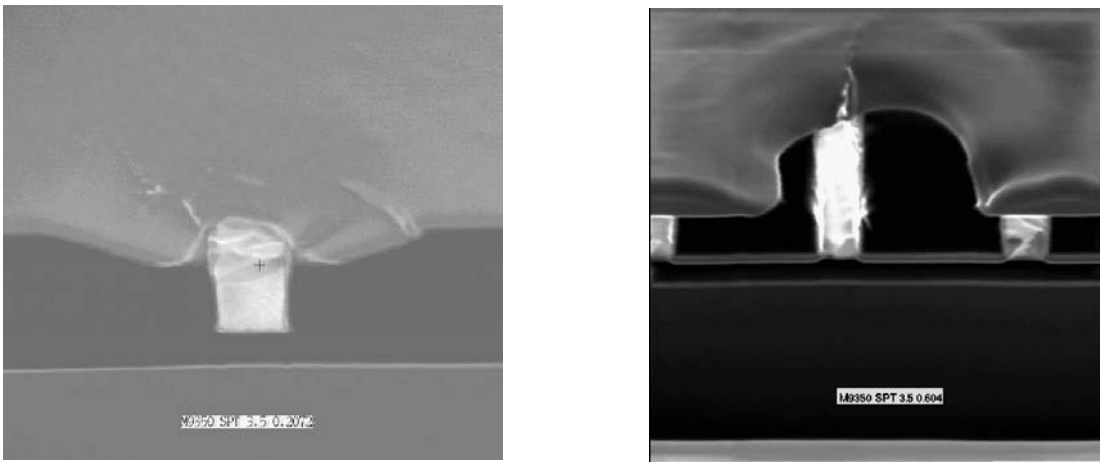

(a) (b)

Figure 4.9: FIB cross-sectional images of laser-cut sites processed with energies below the passivation-pop-off threshold energy. (a) laser energy: 0.192μJ, and (b) laser energy: 0.215μJ.

processed with a laser energy of 0.604μJ. It shows a somewhat bigger crater than that in Figure 4.9(a), but it is still smaller than those of other cuts processed with 1.047 μm wavelength laser.

The lines connecting two adjacent lower corners seem to be gaps caused by the peeling of SiO_2 and possibly a little filling of molten Cu. These lines were observed only in the cut-site process with the longer wavelength and this also gives another hint of a more uniform temperature distribution.

Figure 4.10(a) is an FIB cross-sectional image of cut site processed with a laser energy of 1.506 μJ and it portrays a clean cut within process window. It shows a smaller cavity size, which was consistent throughout the other cuts in this section. However, the peeled line connecting two lower corners of two adjacent links can be seen and this pose a reliability concern.

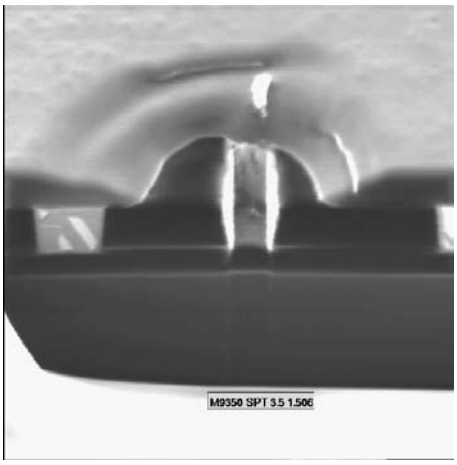

(a)

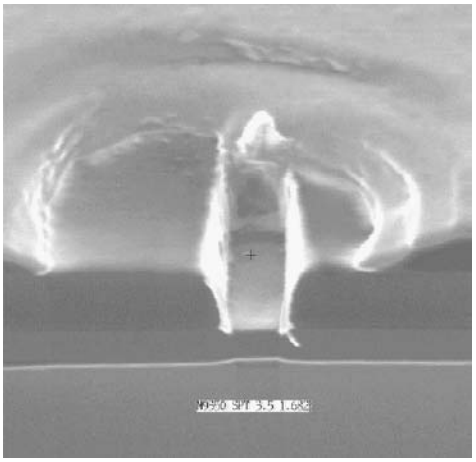

(b)

Figure 4.10: FIB cross-sectional images of laser-cut sites processed with energies beyond the process window. (a) laser energy: 1.506μJ, and (b) laser energy: 1.66μJ.

The cut site in Figure 4.10(b) was processed with a laser energy of 1.66μJ. The image clearly reveals a small lower crack directed to the substrate. Even though there is no substrate damage at this high level laser energy, this is thought to limit upper bound of process window for a reliable cut as mentioned in the analysis of Al cut energy process window.

4.4 Discussion

Laser processing of Cu fuse with two different wavelength laser has been analyzed. Unlike the Al processing, parallel-directed cracking was noticed in the upper and the lower corner. From the ideas of paralleled upper and lower cracks, lateral make-link proposed by J. B. Bernstein [29] is suggested for the repair process instead of cut structure.

For improvement of Cu processing, it is of importance to modify the fabrication process, so the two layers of dielectric can stick to each other better. This will keep the crack from going to parallel direction and, thus the crater will have a smaller size.

Smaller crater was observed from the cut sites processed with longer wavelength. This is considered from the longer wavelength and there exists a quantum mechanical effect change depending on the laser wavelength. However, this is beyond the scope of this work and left for more investigation.

Chapter 5

Metallic Vertical Make-Link

5.1 Introduction

As prevously mentioned, laser technology has found widespread applications in the repair of integrated circuit chips, which exhibit large-scale redundancy in their designs, for yield enhancement [15].

However, the laser cutting of the deeply buried metal lines has become increasingly difficult with the development of multi-level metallization technologies. Moreover, the cracks formed at the lower corners of a metal line during laser processing and molten metal filling the crack, which is unfavorable to the electrical disconnection of the fuse, has been reported as an ultimate limit for the laser energy processing window of the cut resulting in the low yields of the processing [30].

As a complementary scheme, various laser-induced metal antifuse (make-link) structures have been proposed and some of them have shown much wider process windows and higher yields [18, 41, 29, 42]. Make-link technique in redundancy involves a linkable redundant region to include new devices that were not previously present in the system by laser restructuring. It has been shown that the

make-link has potential applications as extensive as the laser cut link. Furthermore, the ability to both make and cut links allows for a much broader range of repair algorithms.

Recently, J. B. Bernstein *et al.* have developed direct metal-to-metal connections between two adjacent metal lines on the same level of metallization (lateral link) as a result of the cracked dielectric formed by the thermal expansion of metal from a laser energy and the molten metal filling the crack [29, 43]. Vertical connections between two different levels of metallization (vertical link) which involves the same mechanism as that of the lateral linking process have also been reported with laser parameters which resulted in solid metallic connections with perfect yield [26].

Compared with the lateral link, the vertical link has several advantages such as; smaller size, no undesirable side links [34] and higher reliability [27]. Furthermore, the laser process has a broad laser energy process window and forms a robust link. This vertical link formed within the process window has cracks that are completely terminated on the upper metal lines with no damage to the passivation.

In this chapter, vertical metallic make link is introduced with the chip architecture, the mechanism and the finite element modeling with and without latent energy.

5.2 Chip architecture

This make link structures are built in the same wafer detailed in section 2.4.1. The following is the more detailed fabrication steps.

The aluminum lower metallization was deposited on SiO_2 field oxide grown

on the silicon substrate. Between the metal levels there was an inter-level dielectric (ILD) consisting of planarized SiO_2 deposited from tetraethylorthosilane (TEOS)-based plasma enhanced chemical deposition (PECVD) at 389 °C followed by a layer of spin-on-glass (SOG). Aluminum vias connected the upper metal lines (metal 2) down to the lower metal lines (metal 1) through the dielectric. Each level of metallization was deposited by sputtering to form $0.75\mu m$ and $0.55\mu m$ thick lines for the upper and the lower metal lines respectively. The metal lines were coated with a $0.09\mu m$ undercoating and a $0.05\mu m$ overcoating layer of titanium nitride(TiN). Metal 2 was coated with SiO_2 (silane PECVD at 400 °C and SOG) followed by a passivation layer of silicon nitride (Si_3N_4, again PECVD at 400 °C). The oxide is expected to exhibit a compressive stress of about 200MPa or less at a room temperature.

It is noted that the top-layer metallization and the next one have been defined as metal 2 and metal 1 respectively for simplicity throughout this work, though they are metal N and metal N-1 in the current multi-level metallization, where N is the total number of metal layers. Figure 5.1 illustrates the cross-sectional view of the chip.

5.3 Making a Vertical Link

First, a substrate must be mounted beneath the laser which is focused on the linking target as depicted as a double-dashed circle in Figure 5.2 (a). The target in our test structure is metal 1. Once the spot is centered and is impinging within the annular region of metal 1, the laser pulse is emitted. The laser energy passes through the Si_3N_4 and SiO_2 until it encounters the surfaces of metal 1 where it is quickly absorbed.

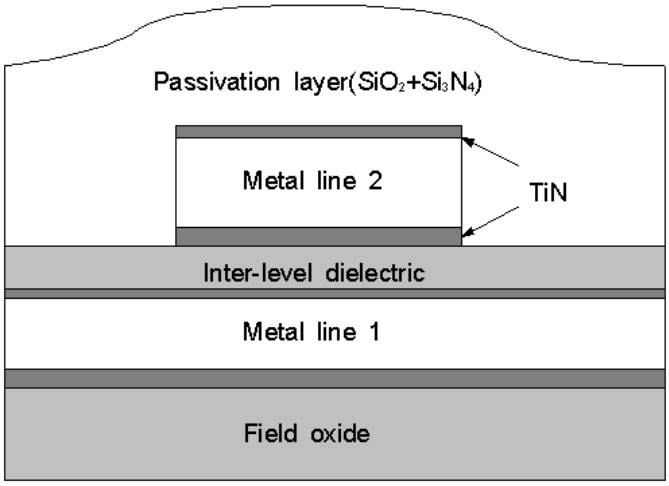

Figure 5.1: Block diagram cross-section of chip architecture with relevant dimensions given(not drawn to scale).

Figure 5.2 (b) displays the cross-sectional view of designed link spot. As the aluminum in metal 1 within metal 2 frame heats up from the absorbed energy, it expands. Aluminum undergoes a large volumetric increase as it expands, and the sudden expansion induces tensile stresses within the surrounding SiO_2. The maximum stresses are situated around the upper corners of the aluminum lines due to its rectangle-shaped geometry from the cross-sectional view. In order to release the stress caused by the expanding aluminum, cracks initiate in the SiO_2 from the aluminum corners. Due to the stress concentration in the oxide, the upper-corner cracks from the line propagate toward metal 2. Once the cracks meet the bottom of metal 2, a fissure is formed between the metal 1 and metal 2 giving the heated and molten Al an avenue for pressure release. When the aluminum flows into the fissure from metal 1, it creates a connection from metal 1 to metal 2, forming a link.

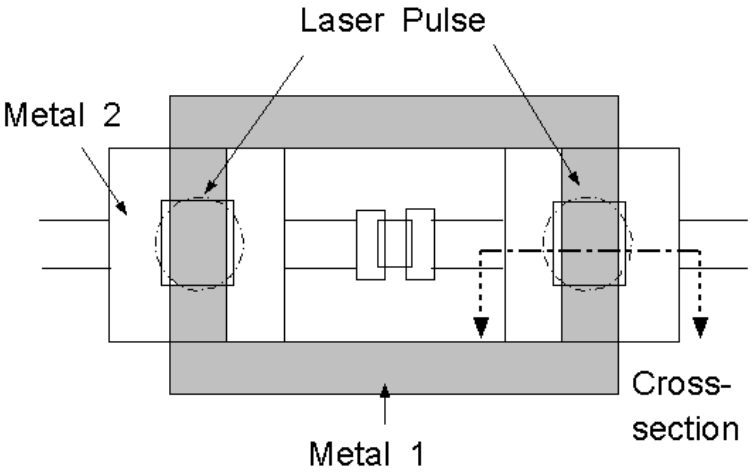

(a)

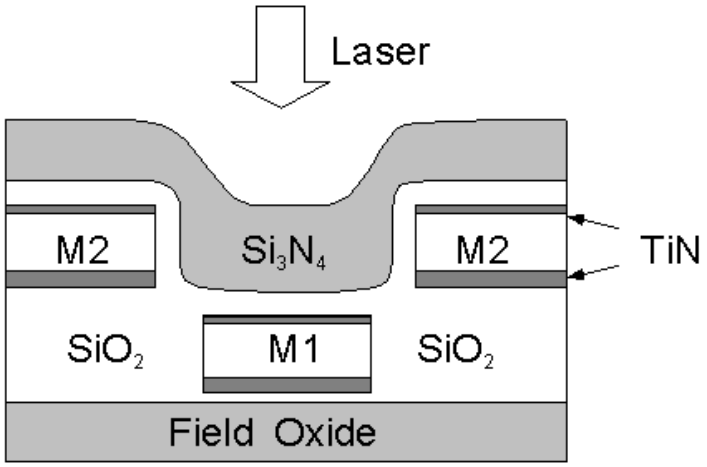

(b)

Figure 5.2: Schematic of vertical link structure before a laser pulse, (a) top view of link-designed structure, (b) enlarged cross-sectional view of link-designed structure.

5.4 Results

The technology uses the existing metallization layers without modifying the standard CMOS process. Very high yield (greater than 99.99%) has been reached in a broad range of laser energies and spot sizes. The electrical resistance of the link depends on laser conditions for each structure. In case of a 0.7 μJ laser energy and a round $1/e^2$ spot size of 3.0 μm in diameter, the link resistance has been reported to be less than 0.8 Ω [42].

Experimental results are displayed in Figures 5.3. It is the FIB cross-sectional images of the plane indicated as dashed line in Fig 5.2 (a) after appropriate laser processing. Solid metallic connections form as the results of the cracked dielectric between the two levels and the molten metal filling of the cracks.

In the case of Figure 5.3(a), a 0.4 μJ laser pulse with a 5 μm spot size was applied to the link structure possessing 3 μm wide metal 1 line and 4×4 μm metal 2 square frame hole. The voids in upper-left metal indicate the laser pulse has been offset to the left side of the structure a little bit. However, it shows a solid link sheet between two levels of metal lines. 0.6μJ laser pulse with a 6μm spot size was applied to the link structure with 4μm metal 1 line and 6×6 μm metal 2 frame hole in case of Figure 5.3(b).

From the both figures, the link can be seen to have been formed from extruded metal from the lower level. Since all the material that flowed in the cracks originated from that one thin layer, there is a deficit of metal which remains in the line. The dark regions in the metal 1 line are a result of the displaced metal. The metal flows due to the thermal expansion while it is hot. Then, as it cools, there will be voids left in the link sheet as well as in the metal.

To have a reliable make-link, the laser energy parameters are very important.

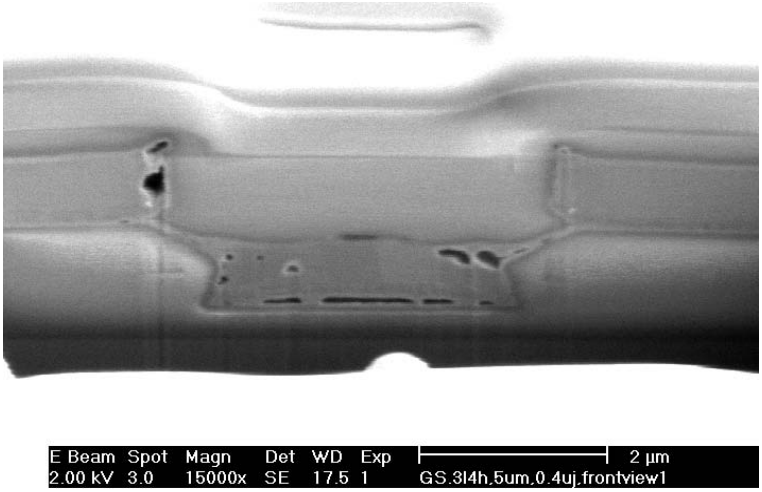

(a)

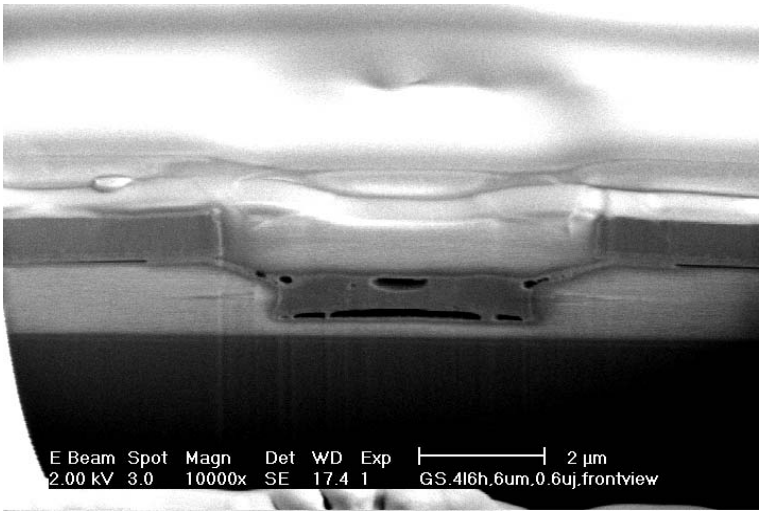

(b)

Figure 5.3: FIB cross-sectional images of vertical links (a) link between 3μm wide metal 1 and two sides of the hole in metal 2 (4×4μm square hole), (b) link between 4μm wide metal 1 and two sides of the hole in metal 2 (6×6μm square hole)

In the case of wider metal line, it tends to have wider range of process window in terms of laser energy. This means that the larger metal 1 line structure has higher upper bound of laser energy process window for linking. The energy process window analysis of scaled make-link structures will be followed in Chapter 7.

Ideally, the link sheet should end on the corner of upper metal structure in order to reduce the volume of voids in metal 1 after processing. However, the link sheets on both sides missed each of the lower corners of upper metal line and end up at the bottom of undercoating layer of TiN in case of Figure 5.3(b). Thus, the metal used for the link sheet was wasted.

It is noticed that the thickness of link sheet is a very important parameter in terms of its reliability. As the link sheet gets thicker, it make the link more reliable. It is a laser energy that decide the thickness of link sheet. On the other hand, too much energy causing too thick link sheet is also against the reliability of make-link. That is, the volume reduction of metal from the first metal level accounts for the increased resistance due to too much laser energy. Similarly, if not enough energy is delivered to metal 1, there is insufficient metal in the link sheet accounting for the higher resistance on the low energy side.

Therefore, we can assume that there exists an optimum range of $V_{link\ sheet}/V_{metal\ 1}$ to have reliable link for a specific link structure. This will be discussed in more detail in next chapter with the scalability calculation of make-link structure.

5.5 Simulations

To simulate the link formation process, a custom finite element model (FEM) was utilized. The model was simulated using the same MSC *Mentat* software which was also used for the cut link simulation. The results are briefly shown in

Figures 5.4 and 5.5, and the cracking indicates the path of a link connecting two layers of metallization.

The structure with 4 μm wide metal 1 with a 6×6 μm square metal 2 frame was used in case of Figure 5.4 and 5.5, and the each figure shows that only half of cross-sectional structure used for simulations, so the time for computation could be saved. It is noted that the simulations were 2-dimensional and turned out that this did not lose its significance. The laser energy and pulse duration were 0.22 μJ and 15 ns respectively.

Figure 5.4 shows a maximum principal stress contour picture at a time of 4.8 ns after a laser beam of 0.35 μJ. This is the moment right before a crack initiation on the upper corner of metal 1. Thermal expansion of the lower metal caused by laser heating induces stress concentration at both the upper and lower corners of the metal, so the surrounding dielectric (SiO_2) has the propensity to be cracked from the locations where the stress exceeds the critical stress. As used in cut link process simulation, 1 GPa was used for the critical stress of dielectric [38]. Mostly, the stress in dielectric concentrates around the upper corner of metal 1 in the beginning of the laser pulse. This is because the laser hit on the top surface of metal and the extinction depth of aluminum for the laser beam is too small, and, therefore the dielectric cracking starts from the upper corner earlier than the lower corner.

The crack continues to advance along the path of stress concentration which is perpendicular to the developed tensile stress. Figure 5.5 shows two major steps of cracking after the stage of Figure 5.4. Both of the figures are drawn by simulator with contours of maximum principal total strain. Figure 5.5 (a) shows a crack propagation from the upper corner of metal 1 to lower corner of metal 2. It was

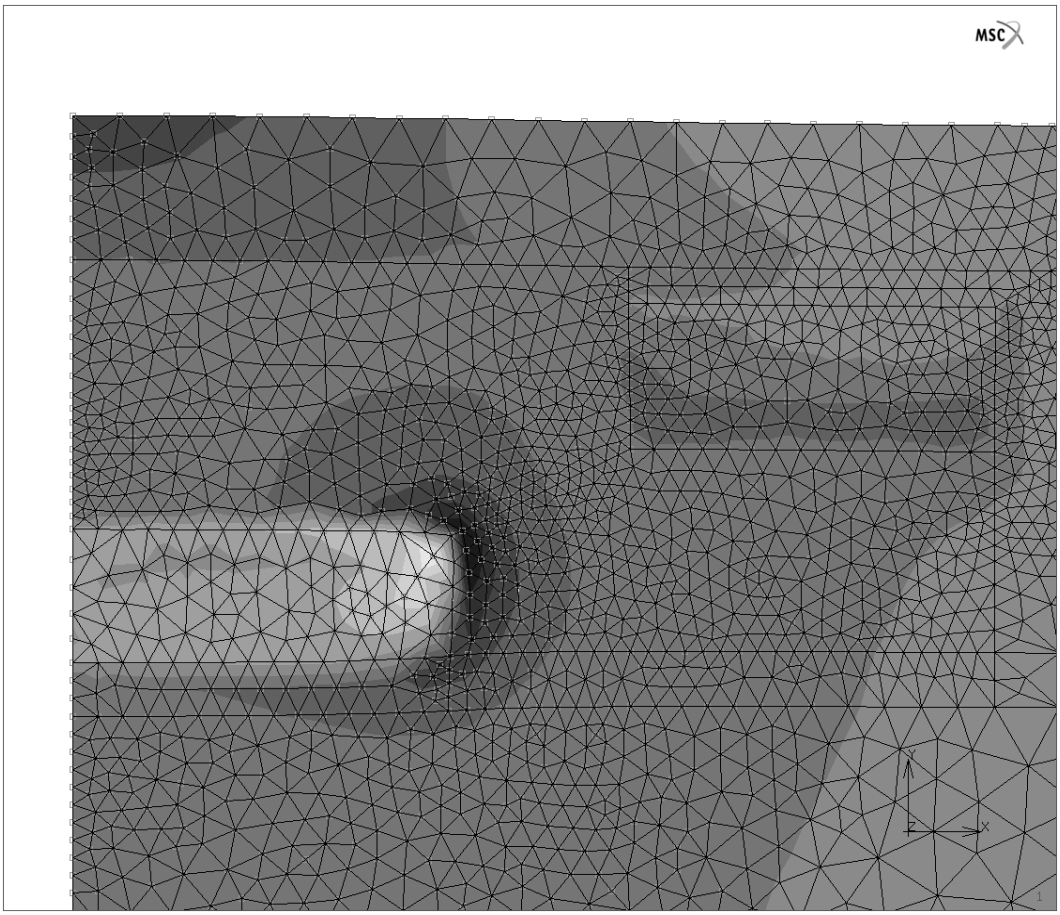

Figure 5.4: Finite element simulation result showing the maximum principal stress in the dielectric at the upper corner of metal 1, 4μm wide metal 1 with a 6×6μm square metal 2 frame, laser energy = 0.35μJ, time = 4.8ns.

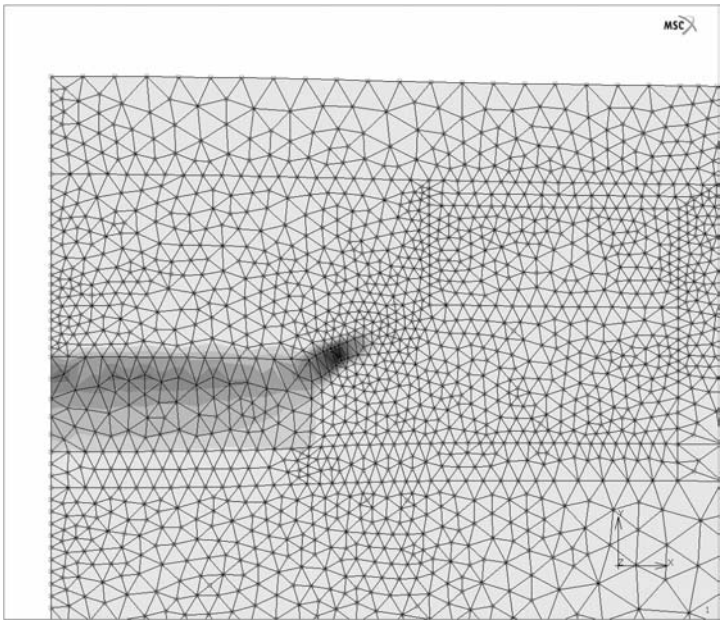

(a)

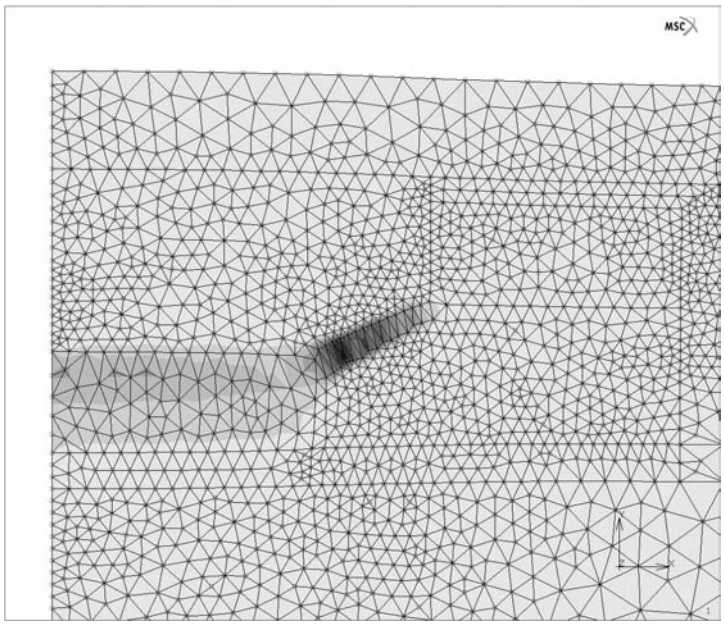

(b)

Figure 5.5: Finite element simulation results showing development of link between two layers of metal lines, maximum principal total strain contour pictures, 4μm wide metal 1 with a 6×6μm square metal 2 frame, laser energy = 0.35μJ, (a) time = 5.5ns (b) time = 6.7ns.

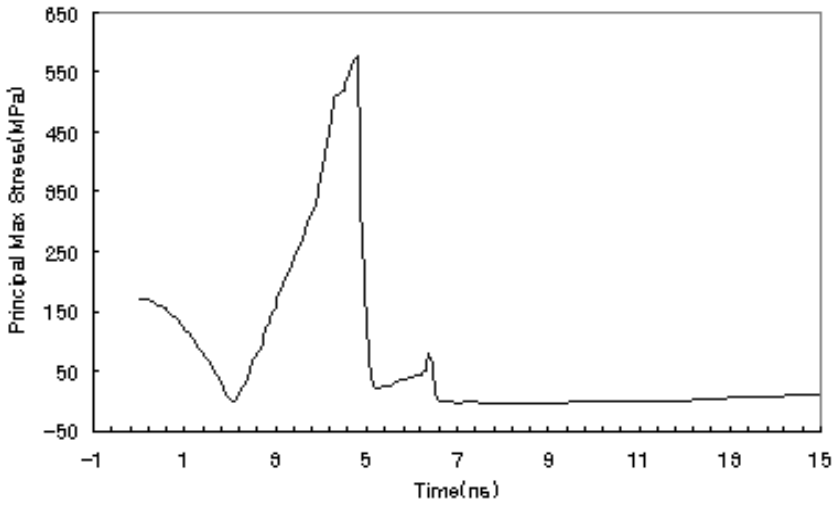

Figure 5.6: Maximum principal stress in the dielectric around the upper metal corner.

taken at a time of 5.5ns after a laser pulse. The contours within metal 1 indicates the crack was caused by the expansion of the metal.

A complete crack made between two layers of metallization can be seen in Figure 5.5(b). 6.7 ns of a laser pulse with a 0.35 μJ energy irradiated at the moment of this figure. The strain energy drives the crack propagation and less than 2 ns was taken for the complete linking from crack initiation. It is noted that the metal 2 frame also acts as a cracking stopper as long as the laser energy is not too big. Therefore, a properly designed frame width and gap can effectively extend the process window in terms of laser energy. The failure criterion at high energy end for make-linking is defined by the passivation break caused by the excessive laser energy absorbed by the metal 2 frame. [44].

As mentioned earlier, the stress accumulates with the increase in temperature

until a crack initiates. The onset of the dielectric fracture corresponds to the sudden release of the stress at the original crack initiation point and it can be seen in Figure 5.6. At the moment of cracking initiation on upper corner, the temperature of the top of lower metal was 1,161K, which is over the melting temperature of aluminum. However, the results are based on the superheating of aluminum and it is considered that it melts with the pressure release caused by cracking. This will be more detailed in the following section.

5.6 Superheating under a Laser Beam

Laser processing is a phenomenon in which energies large enough to melt (or even vaporize) condensed substances can be applied in a time interval much shorter than the time for the transformation to take place [45].

Figure 5.7 shows a conventional phase diagram where path 1 is followed under normal equilibrium conditions. If a quantity of energy, E_a (which is sufficient to the melting), is rapidly deposited into the system, the path taken is that along the equipartition energy line, path 2. Depending on the peak power of the laser pulse and the system in question, the range over which super heating occurs is several thousand degrees. The time, τ_{MELT}, is then the actual material-dependent melting time. The departure of path 1 from the equipartition line is indicative of defect formation [46].

S. Williamson and coworkers reported that the time required to melt the aluminum increases exponentially with decreasing fluence and at $1.4 \times F_{melt}$ the phase transition time increased to about 1ns [45]. They used the picosecond electron diffraction technique to provide time resolution of laser-induced melt evolution in aluminum. During the delay time, the two phases coexist as a

heterogeneous melt while the superheated solid is being continuously transformed into liquid and they interpreted the results in the context of the defect theory of melting.

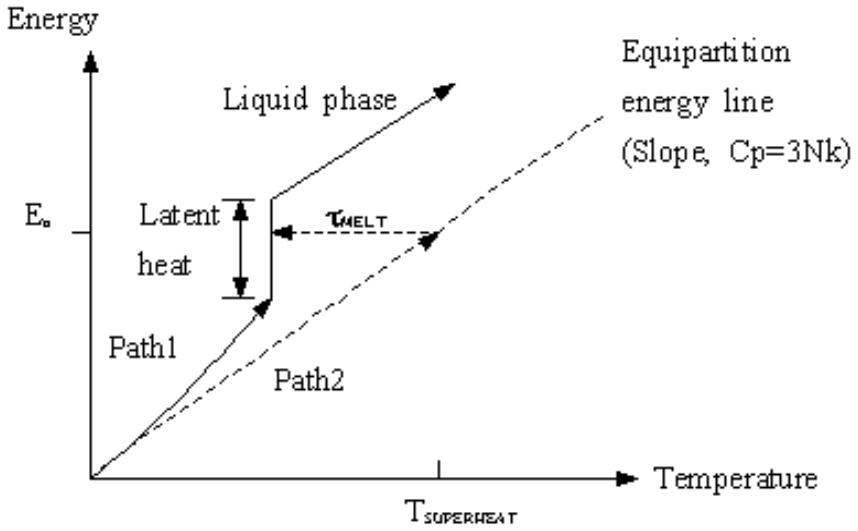

Figure 5.7: Caloric diagram of the solid and liquid phases for a simple metal. Path1 is followed when the energy is deposited on a time scale slower than the defect formation time. Path2 is followed when the energy is deposited instantaneously [46].

Based on this defect theory of melting, all the make-link simulations were done assuming the superheating of aluminum under the laser beam. On the other hand, it is noted that a simulation including latent heat considering aluminum melting was conducted.

The two temperature profiles are shown in Figures 5.8 and 5.9 for a comparison. Figure 5.8 is a result from a simulation with superheating assumption and Figure 5.9 is a result of the simulation with consideration of latent heat. The laser energy used for both simulation was 0.3 μJ and the structure was the same

as the one used in previous section. Both figures show the temperature changes of three spots on the top surface of aluminum and the higher temperature curve indicate the temperature closer to the center of top. The lower the curver is, the closer to the upper corner of Al line. As can be noticed there is a slight shoulder on each curve in Figure 5.9 and that indicates the moment of aluminum melting.

However, it did not make significant changes on the results other than those and it is considered that it is because the simulator, MSC *Mentat*, can not simulate the flow of molten metal after melting. In these modeling works, the abrupt changes on material properties upon melting of metal have been considered and all the convergence problems were resolved. However, the metal flow and displacement caused by the laser was not able to be included. At this point, more sophisticated material modeling is needed to include more detailed information on the metal phase change and the flow of molten metal. The stress release from the flow of metal can not be ignored and it will be the key factor to understand the whole procedure of laser processing. At this moment, it is left for the future work.

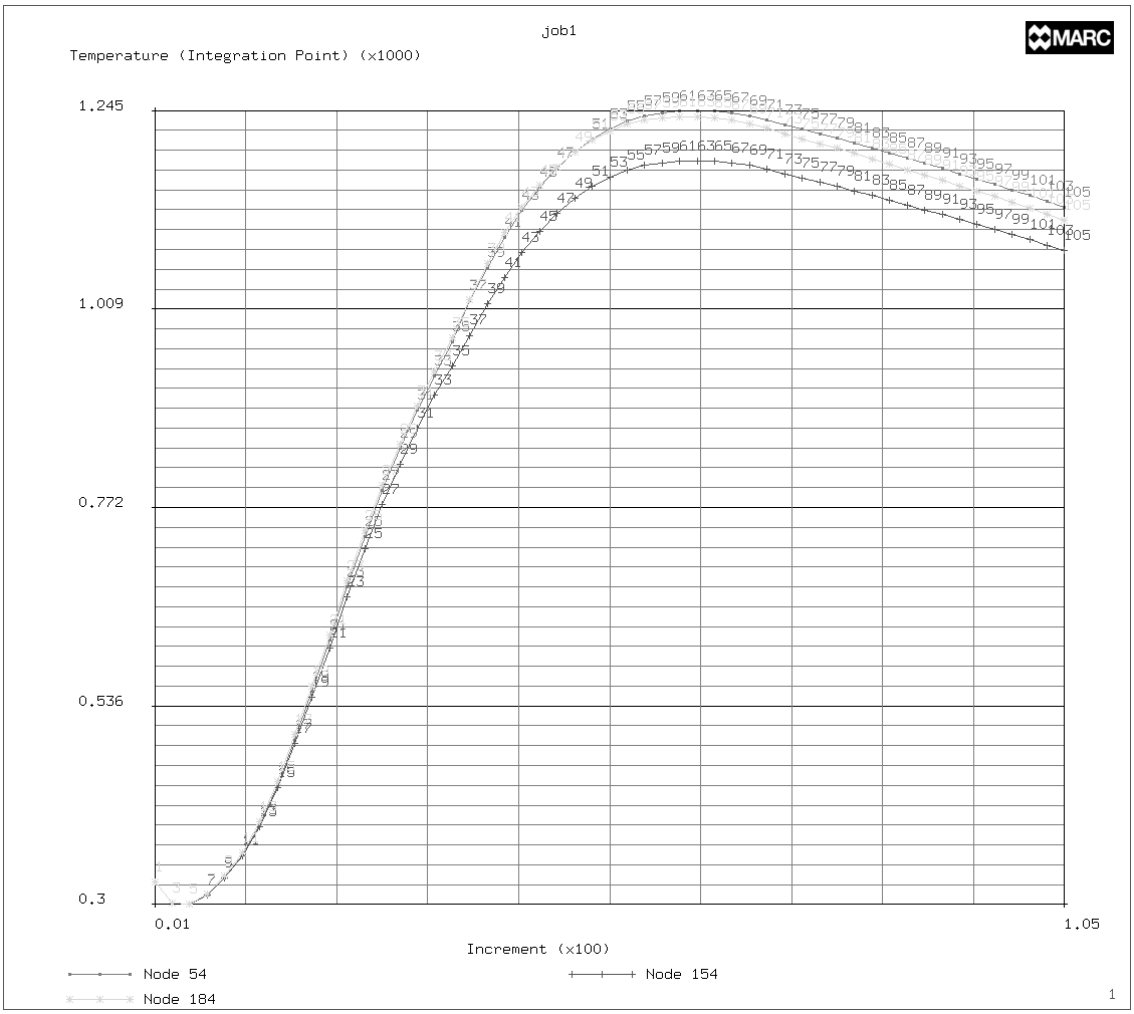

Figure 5.8: Temperature profiles of three spots on the top surface of aluminum obtained from simulations, the highest curve : temperature in the center of aluminum, the lowest curve : temperature on the corner of aluminum, a simulation result without consideration of latent heat.

Figure 5.9: Temperature profiles of three spots on the top surface of aluminum obtained from simulations, the highest curve : temperature in the center of aluminum, the lowest curve : temperature on the corner of aluminum, a simulation result including latent heat.

Chapter 6

Scalability of Laser-induced Vertical Make-link Structure

6.1 Introduction

The continuous shrinking of device dimensions of Si MOS technology has dominated the scaling of repair technologies. Since the density of memory cells has been of primary importance in reducing their cost, the reduction in cell size has been achieved by the use of smaller interconnect line width as well as by the cell structure complexity [47].

With this trend, the laser vertical linking process should be incorporated seamlessly with the shrunken line widths and spacings in order to be compatible with today's semiconductor technology. In this chapter, an estimation of the scalability for a vertical link structure is presented to show that vertical metallic link meet the current processing technologies.

6.2 Experimental

6.2.1 Link Structure Parameters and Test Setup

The metallization, Al ($1\%Si$, $0.5\%Cu$), was sputtered and etched to form 2, 3, 4, and 6μm wide and 0.55μm thick lines for lower-level metallization (metal 1) and 3×3, 4×4, 6×6, 8×8 μm square frames for upper-level metallization (metal 2) with 0.75 μm thickness. The inter-level dielectric (ILD) with 0.75μm thickness was sandwiched between the two levels of metallization. The schematic of a vertical link structure is shown in Figure 6.1.

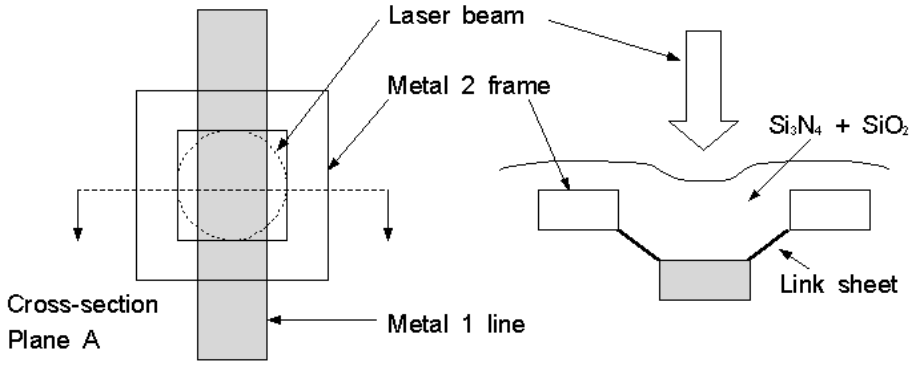

Figure 6.1: Schematic of a vertical link structure after a laser pulse, (a) layout and (b) cross-section from Plane A.

A passivation layer consists of 0.7 μm of Si_3N_4 over 0.3μm of SiO_2, covering the metallization. The Al lines were undercoated and overcoated with a 0.09μm thick layer and a 0.05 μm thick layer of TiN respectively.

The laser system used to perform the linking was an *XRL 525* laser process system. The system employs a *Spectra Physics* diode-pumped, Q-switched, Nd:YLF laser(1047nm) operated in the saturated single-pulse mode. Pulses, with

lengths of approximately $15ns$, were directed through focusing optics to produce a $1/e^2$ beam diameter of approximately 5, 6 and 8μm (at focus) for each structure. The positioning accuracy of the laser system was within approximately 0.5μm.

Analyses of the processed vertical links were performed using a *Dual Beam 620D*, focused ion beam (FIB) and scanning electron microscope (SEM), system manufactured by FEI. The system was used to obtain cross-sectional images of the processed link-sites and to investigate the volumes of link sheets and their ratios to each metal 1 pad under respective metal 2 square hole. The FIB cross-sections were made perpendicular to the wafer surface and parallel to the direction of the laser beam in Plane A to analyze the volume of link sheets.

A second set of experiments was performed using a *9200HT PLUS* laser processing system manufactured by ESI. The vertical link structures used in this set were a metal 1 line with 0.8 and 1.2μm width aligned underneath a metal 2 square frame of 1.6×1.6 and 2.2×2.2 μm. A round $1/e^2$ spot size of 2.4μm in diameter was used for these processes in order to avoid the possible damage to the metal 2 frame. For the resistance measurement of these structures, four-terminal structures were probed in order to get more accurate resistance of link sheets.

6.2.2 Observations Results

From the earlier experiments, it was proven that the yield of the link process, for a specific structure, can reach higher than 99.99% under appropriate laser conditions [42].

Figure 6.2 displays the cross-sectional images of link sites processed with a laser energy of 0.6 μJ with round $1/e^2$ spot sizes of 6.0 and 8.0 μm in diameter for (a) and (b) respectively. The images clearly reveal that the link sheets connecting

the upper corners of metal 1 with the lower corners of metal 2.

Figure 6.2(a) portrays a vertical link consisting of a 2μm wide metal 2 frame with a 6×6 μm square hole aligned over 4 μm wide metal 1 line. The ratio of the volume of voids to the volume of metal 1 remaining looks higher than that of Figure 6.2(b), which is a structure having 6 μm wide metal 1 line and a 8×8 μm square hole of metal 2 frame. This stems from the fact that the density of laser energy on metal 1 in Figure 6.2(a) is larger than Figure 6.2(b).

The voids were produced in the metal 1 line due to the transport and re-solidification of molten metal during the link formation. This voiding mechanism can not be eliminated by simply adjusting laser conditions or link structures. Therefore it is an intrinsic defect of the process which poses reliability concern. The evaluation of electromigration reliability of the vertical link structures has been conducted through accelerating electromigration test and the results are detailed in [27].

In that work, we have shown that the links exhibit a commercially acceptable lifetime (38 years at room temperature with constant current density of 3.0MA/cm^2) and a modified vertical link structure was proposed to improve the electromigration reliability.

In Figure 6.2(b), it is interesting to see the angle of link sheets is a little bit steeper than that in Figure 6.2(a) and terminated right on the lower corner of metal 2. This angle appears to be related to the energy densities of the laser pulse. That is, the angle tends to be steeper as the impinged laser energy density decreases. It is important that the crack trajectory terminates on the lower corner of metal 2. This is not only because the contact resistance between Al metallizations is less than that between Al and TiN layer, but also because the

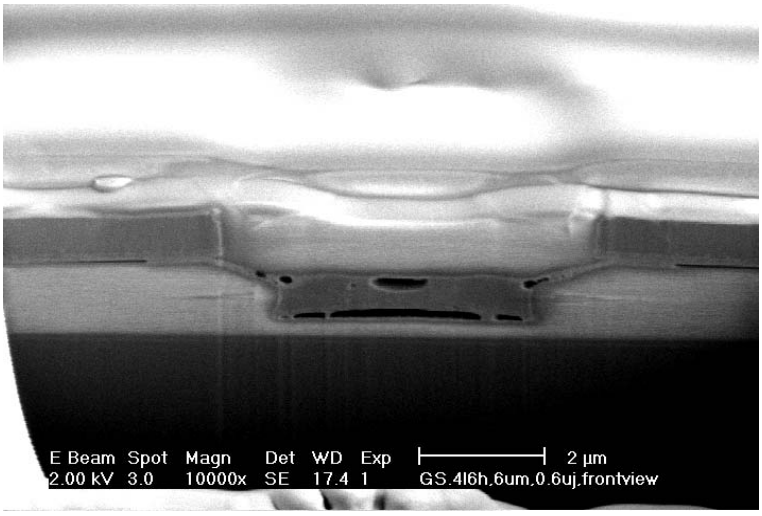

(a)

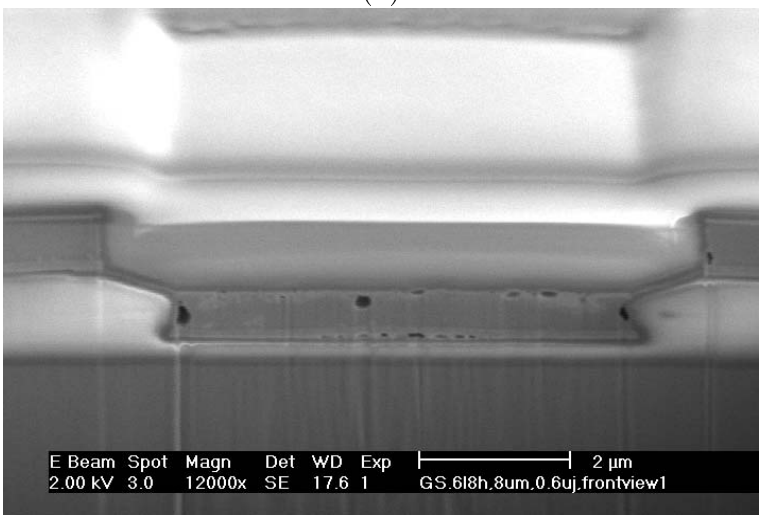

(b)

Figure 6.2: FIB cross-sectional images of vertical links (a) link between 4μm wide metal 1 and two sides of the hole in metal 2 (6×6μm square hole), (b) link between 8μm wide metal 1 and two sides of the hole in metal 2 (8×8μm square hole).

metal quantity used for linking from metal 1 line can be saved due to the molten-metal-flow blocking effect of metal 2. Therefore, it is important to find optimal laser conditions for a specific structure in order to make a reliable link without wasting metal 1. This will be detailed in the next chapter with an analysis is energy process window of make link.

6.3 Measurements of Link Sheets

Table 6.1 shows the laser parameters, yields, measured resistances of links and the ratios of the volume of link sheet to the pre-processed volume of metal 1 under the metal 2 square hole of metal 2, V_l/V_{m1}, measured with FIB. The data reflect links with perfect yields with a specific laser condition for each structure. Each set of data represents 1320 links and the average resistance of each structure was calculated.

Two-terminal structures were probed for resistance measurements including the resistance of metallization as well as the link sheets. Therefore, the resistance tends to decrease as the size of the link structure increases. This trend is also partially caused by the amount of metal remaining in the metal 1 line after linking.

The average thickness of a link sheet was measured in the center of one side link sheet(wing shaped) when cross-sectioned in Plane A, which means we consider a thickness in the center of the thickest part of the link sheet as the overall average thickness. Here, it is noticed that the link sheet has been simplified as a two sided geometry within metal 2 square frame hole to investigate the link sheet volume, while in reality, the link sheet forms like an annulus around the inside of the link area.

Table 6.1: Calculations of $V_{linksheet}/V_{metal1}$.

	Energies (μJ)	Spot (μm)	R. (Ω)	V_l/V_{m1} (%)
2 μm wide M1 4×4 μm M2	0.4-0.6	4	7.72	20.5
3 μm wide M1 4×4 μm M2	0.4-0.6	5	4.10	11.1
4 μm wide M1 6×6 μm M2	0.5-0.7	8	1.78	29.0
6 μm wide M1 8×8 μm M2	0.6-0.7	8	0.79	2.4

Throughout the structures, the average thicknesses of link sheets, for various structures, are less than 200 nm except for the case of link structure with a 4 μm wide metal 1 line and a 6×6 μm square hole of metal 2 frame. Its thickness is as thick as 220 nm. The thinnest one is 130 nm from the structure with a 6 μm wide metal 1 line and a 8×8 μm square hole of metal 2 frame due to the insufficient laser energy compared to the size of metal 1 structure.

The V_l/V_{m1} shows very low value in case of the link with a 6 μm wide metal 1 line and a 8×8 μm metal 2 square frame due to the large amount of metal 1 pad under the square hole and insufficient laser energy density as mentioned above. Nonetheless, this does not mean that the thin link sheet(130 nm) of this case is not reliable under operational conditions since the reliability test in [27] was conducted at such an accelerated condition, at a temperature of 300 $^{\circ}C$ and a current density of 3 MA/cm^2. A link sheet of this size was determined to be

sufficiently reliable so as to be used in dense circuit.

From the experimental observations, it has been revealed that the values of V_l/V_{m1} vary depending on the laser parameters. Considering that the link sheet is the main reliability concern, it is desirable to have a thick link sheet. However, too thick link sheets are not favorable either, in terms of the reliability, since it coincides with a lack of metal remaining in metal 1 and increase the overall resistance. We learned from the earlier experiments that the lifetime and resistance show opposite trends with the maximum lifetime corresponding to the lowest electrical resistance [27]. Thus, there exists an optimal laser energy for a specific link structure and the overall resistance will increase with lower or higher energy.

It has been shown through the reliability test that vertical link with a 4 μm wide metal 1 line and a 6$\times$6 μm metal 2 frame hole, which has the largest value of V_l/V_{m1}, 29%, was the most robust link [27]. This result was expected since it was obvious that the thicker link sheet is more reliable to some extent as long as the lower metal line bears enough metal. Effort has been made to find the optimal ratio for a reliable link of each structure and a 45% of V_l/V_{m1} was calculated by W. Zhang *et al.* [48]. This ratio will be taken as an optimal ratio for a reliable link, which indicates the link of minimal resistance, in the scalability estimation to follow.

6.4 Four-Point Probe Measurement of Scaled Link

The smaller link structures configured for four-point probing were processed with a round $1/e^2$ spot size of 2.4 μm and a laser energy of 0.35 μJ with the ESI laser processing system.

Figure 6.3 shows statistical resistance data of link structures of a 0.8 μm wide metal 1 line aligned underneath a 1.6×1.6 μm square hole of metal 2 frame and a 1.2 μm wide metal 1 line aligned underneath a 2.2×2.2 μm square hole of metal 2 frame. Each set of data represents 1024 links and were probed for link resistance. The average resistances of both links are 10.80 Ω and 9.95 Ω respectively. These results are likely to be more accurate due to the measurement method. Consequently, the increasing trend of resistance with decreasing size of link structure, as can be seen in Table 6.1, was preserved, but not as dramatic as would be extrapolated from the two-point probe measurement. It is noted again that the resistance varies depending on the laser parameters used and the lowest resistance will be obtained under optimal laser conditions.

6.5 Scalability Calculations

As is well known, device feature sizes for memory chips have been scaled down approximately 70% every generation [49]. Therefore, it is important to reduce the vertical link structure as small as possible to make it commercially viable.

The link sheet is the primary reliability concern in the link structure; thus, it is necessary to have sufficient metal in the sheet. And it is certain that the volume of link sheet required for the optimal laser linking processing will change with the

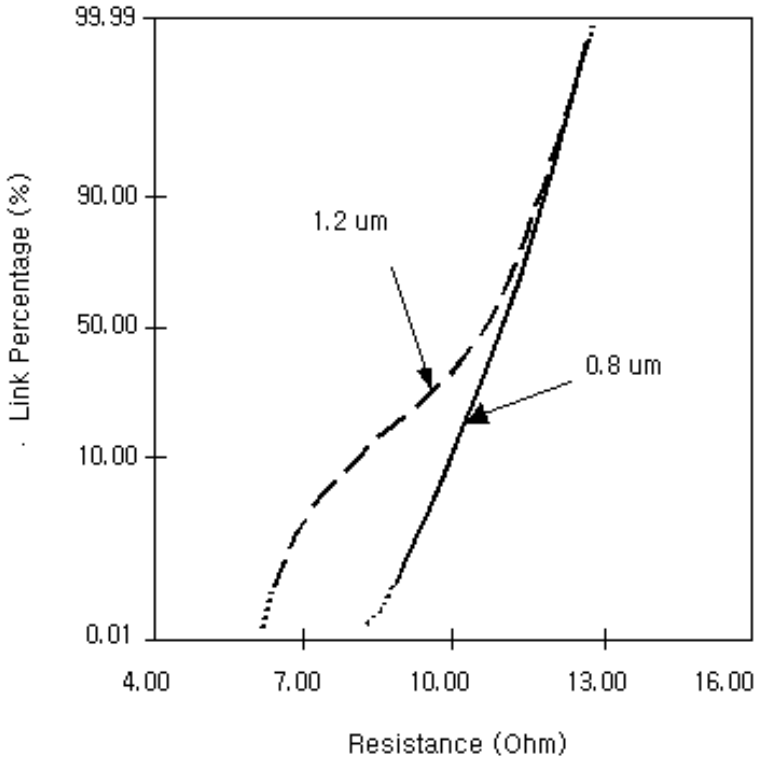

Figure 6.3: Statistical resistance data of small vertical link structures, $1/e^2$ spot size : 2.4 μm, laser energy : 0.35 μJ.

variations of the thickness of ILD. On the other hand, the ratio, V_l/V_{m1}, depends on the thickness of the metal 1 line for the structures having the same width. Therefore, it can be concluded that the capability to scale down the link structure is mainly dependent on the thicknesses of metal 1 line and ILD assuming they are processed with optimal laser parameters. A 2-dimensional approximation of the link (Plane A) is made for simplicity in the calculations to get the relationship between the width and thickness of metal 1 line and the thickness of ILD.

A 130nm link sheet thickness was utilized for the estimation of a possible minimum width of metal 1. The length of the link sheet approximates to the thickness of ILD since there is a step existing around each of the upper corners of metal 1 due to the nature of processing. As calculated previously [48], a 45% of the volume ratio has been adopted to estimate the vertical link scalability. It is noticed that Plane A is the cross-section where the largest void volume exists and the assumption of a larger void fraction decreases the minimum width of metal 1. Nonetheless, we chose the same volume ratio of 45% for a 2-dimensional analysis for the purpose of optimization considering reliability and resistance.

"$\mathbb{A}_{\mathrm{l}}$ and $\mathbb{A}_{\mathrm{m1}}$" stand for the areas of one side link sheet and metal 1 before the linking process, respectively, in the cross-sectional view of Plane A.

$$\begin{aligned} 0.45 \times \mathbb{A}_{\mathrm{m1}} \ \ (\mu\mathrm{m}^2) &\geq 2 \times \mathbb{A}_{\mathrm{l}} \ \ (\mu\mathrm{m}^2) \\ 0.45 \times t_{m1} \times W_{m1} &\geq 0.13 \times t_{ILD} \times 2 \\ W_{m1} \ \ (\mu\mathrm{m}) &\geq 0.58 \times (t_{ILD}/t_{m1}) \end{aligned} \tag{6.1}$$

- t_{ILD} *: the thickness of ILD, which is about the same as the length of a link sheet.*

- t_{m1} *: the thickness of the metal 1 line.*
- W_{m1} *: the predicted minimum width of a metal 1 line from* t_{ILD} *and* t_{m1}*.*

From the calculation, it is shown that the possible minimum width of metal 1 line is proportional to the thickness of ILD and inversely proportional to the thickness of metal 1 line.

In current technologies, device performance improvement has been required with reduction in device size. To meet this requirement, the thickness of ILD films have tended to be kept constant at about 0.5 μm to reduce capacitances [47]. Therefore, the possible minimum width of metal 1 line is mainly dependent on the thickness of the metal 1 line.

It is noted that extensive efforts are being spent to find a material exhibiting a lower dielectric constant for ILD; thus, it is expected that the thickness of ILD will change. This may pose concern of lateral offset between the upper and lower metal lines in the cross-sectional vertical make-link structure. However, it is not a matter of concern due to the steps around the upper corners of the metal 1 line, formed during the processing. That is, metal 2 frame will be closer to metal 1 line laterally and the lateral offset can be avoided if the size of square frame reduces considering the modern laser system can be focused down small enough, to process smaller metal 2 frames. Rather, the decreased size of frame is beneficial to scale down the link size. Even if the link sheet terminates in the middle of metal 2 frame, which is higher than the lower corner, it will help improve the resistance and avoid an excess of the lower metal that does not contribute to linking.

It is also a current trend in the semiconductor industry to increase the thick-

ness of metallization so that low sheet resistance can be maintained for interconnect with decreased line widths for increased circuit density. The architecture of the 256M DRAM built in 0.25 μm technology has achieved up to a 2.5:1 aspect ratio of interconnect [50].

Both trends will help decrease the thickness of ILD and it will result in a decrease in the metal required for link sheet in the future. In turn, it will contribute to the reduction of the line width of metal 1 required for a vertical link.

In the previous section, the results of the second experimental set have shown that the processed links on 1.2μm and 0.8μm wide metal 1 lines are robust and reliable. The quality of links can be improved even more by developing the optimal laser processing parameters. On the other hand, we think that the variation and the difficulty in processing the small link structure lies more on the spot positioning error than the lack of metal 1 remaining.

From the equation 6.1, the minimum width of a metal 1 line for a reliable link in the test wafer can be calculated as 0.79 μm based on a 0.75 μm of the thickness of ILD and a 0.55 μm of the thickness of metal 1 lines. If the thickness of the metal 1 line is increased to 0.6 μm, a width of less than 0.5 μm is possible for metal 1 line assuming 0.5 μm of ILD thickness. This result demonstrates strong potential for practical implementation in 256M DRAM technology.

Furthermore, it is expected that the aspect ratio of interconnects will increase as the quality of processing improves, which will decrease the minimum width of a metal 1 line for the vertical link. For instance, the metal interconnect in SRAM or Flash memory chips has a larger thickness than that of interconnect in DRAM and this will make the laser linking process easier and more reliable with small line width of metal 1, assuming larger positioning technologies can also keep up

with this trend.

If one considers all these semiconductor manufacturing trends, it is clear that cut-link processing will not be capable of disconnecting interconnect with high aspect ratios. In contrast to the disadvantages of the cut-link technique, make-link is expected to show better reliability and yield as the metal in lower-level interconnect becomes deeper and thicker. This indicates strong potential for far-reaching practical restructuring applications in future semiconductor technology.

Chapter 7

Energy Process Window Simulation of Scaled Make-Link and Dense Link Layout

7.1 Introduction

Laser-induced vertical metallic make link has been reported as an alternative to replace the laser metal cut fuse due to its advantages over the conventional metal fuse, such as a wider energy process window with high yield [26], possible processing of the deeply buried fuse without any etching process in multi-level metallization technology, no exposed metal and no damage to passivation after processing [42]. In the previous chapter, the scalability of a vertical link structure was estimated through experimental observations and the vertical metallic make link was expected to have denser integration potential.

The quality of make-linking process is affected by a variety of factors and they include the shape and length of laser pulse, laser spot size and the alignment accuracy as well as the link structure design. Among the various laser parameters for laser processing using commercial Q-switched laser positioning systems, the laser energy is the most important factor, which can control directly the metal

melting as well as dielectrics cracking through the thermal expansion of metal.

In this chapter, the energy process window of shrunken vertical make-link structures is investigated by using a finite element modeling package, MSC *Mentat*. The energy process window for various make-link structures were conducted assuming no laser positioning error. In addtion, the energy process window from experimental observations will be compared with the results from 2-dimensional simulations in order to show that this technique is seamless with today's semiconductor technology. Also, a dense layout of the link structures utilizing a calculated minimum vertical link structure compatible with the current processing technologies is proposed.

7.2 Experimental

7.2.1 Link Structure Parameters and Test Setup

The sample wafer used in this experiment is the same one as described previously in Chapter 6.2.1, except for the addition of the smallest make-link structure with 1.2 μm wide and 0.55μm thick lines for lower-level metallization (metal 1) and 2.2×2.2 square frames for upper-level metallization (metal 2) with 0.75 μm thickness, instead of the largest link structure. The inter-level dielectric (ILD) with 0.75μm thickness was also sandwiched between the two levels of metallization.

Pulses were directed through focusing optics to produce a $1/e^2$ beam diameter of approximately 3.4, 5.1 and 6.8 μm (at focus) for each 2, 3, 4 μm wide metal 1 structure using *XRL 525* laser process system. Different laser spot size was selected for each structure so that approximately 50 % of laser energy could be delivered on to the top of metal 1. The positioning accuracy of the laser system

was within approximately 0.5 μm.

The experiments of smallest make-link structure (a metal 1 line with 1.2 μm width aligned underneath a metal 2 square frame with 2.2×2.2 μm opening) was performed using a *9200HT PLUS* laser processing system manufactured by ESI, which is more advanced system with better laser alignment and energy stability. A round $1/e^2$ spot size of 2.1 μm in diameter was used. Throughout the experiments, each sample link was exposed to a single laser pulse focused on metal 1 with a wavelength of 1.047 μm and a pulse length of 15 ns. Processed samples were then examined both electrically and microscopically to see the connection of a series of link structures.

Microscopic analyses of the processed vertical links were performed using the same *Dual Beam 620D* (FIB and SEM) system.

7.2.2 Experimental Observation Results

There exists available energy ranges for each structure to get acceptable link formation, and the low end of the energy process window is defined as the complete connection of metal link sheet between two levels of metallization. As energy increases, the link sheet gets thicker at a cost of using more metal in lower metal line. The detailed observation results with a series of energies are presented in [44]. The high end of the energy process window for make-linking is defined by excessive material loss in the metal 1 or passivation cracking caused by the expansion of overheated metal 2 frame. A FIB image of a failed link site processed with a laser energy beyond the high end is shown in Fig. 7.1. It shows badly voided metal 1 and 2 lines and cracked passivation due to too much laser energy. In this case, the spot size was 3.4 μm in $1/e^2$ diameter and the laser energy was

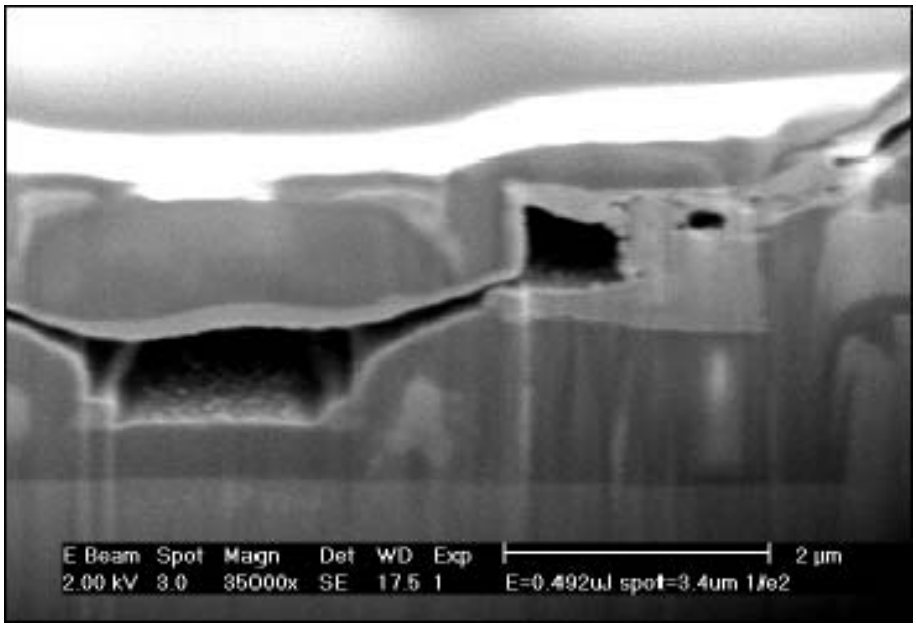

Figure 7.1: FIB cross-sectional image showing a make-link site processed with a laser energy above the high end of process window, a failed link between 2μm wide metal 1 and one side of the metal 2 frame (4×4μm square opening).

0.49 μJ.

With this criterion for the energy process window of make-linking, applicable energy ranges along with the relative process window for each structure are displayed in Fig. 7.2. The ratio of the available energy range (E_{high} - E_{low}) to the average energy (E_a) was adopted as the relative process window. This is done in order to eliminate the dependence of the absolute energy window on the characteristics of different laser systems. Therefore, the relative process window is a normalized and non-dimensional term [44].

Fig. 7.2 shows the relative process window as well as the available energy range increases for the larger make-link structures. For the structures with 1.2, 2, 3 and 4 μm wide metal 1 lines, the relative process window were 0.83, 0.87,

0.9 and 0.96. The upward shift in energy range for the smallest structure is attributed to the calibration difference in relative energy between XRL and ESI laser systems.

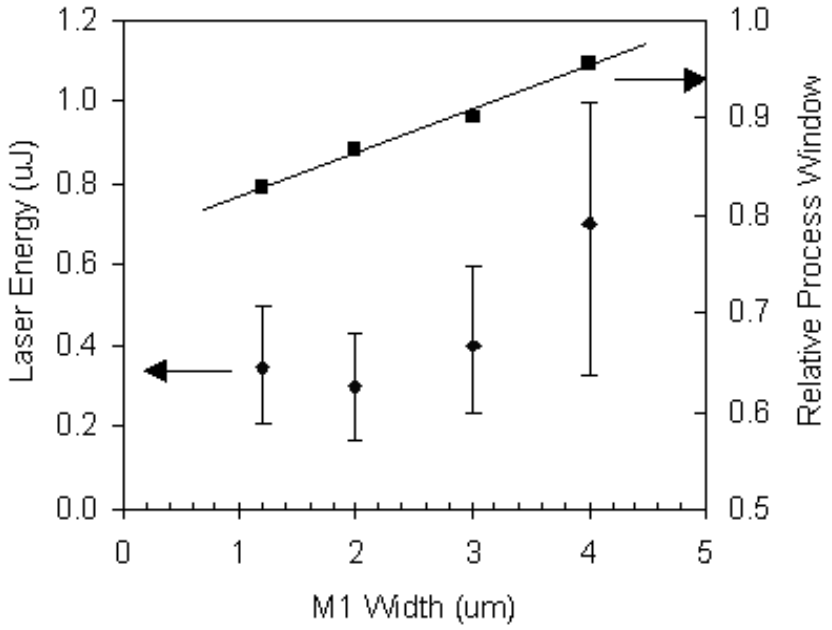

Figure 7.2: Available laser energy range and relative process windows for various link structures.

The results suggest that decreased process windows for scaled links have more limitation of laser parameters. Also the possible damage to the passivation by heated metal 2 frame with laser energy should be more sensitive in case of smaller links and this would ease the initiation of dielectric cracking from upper corners of metal 2 frame. Therefore, the decreasing relative process window with shrunken link structure indicates that more accurate laser parameters are required with scaling-down of link size, such as positioning accuracy and laser energy stability.

7.3 Simulation Results and Discussion

Fig. 7.3 displays the results of finite element modeling of the cross section of failed scaled make-link caused by a laser energy above the high end of energy process window. It shows the cracked passivation caused by the thermal expansion of metal 2 frame which is heated by absorption of high laser energy. The width of metal 1 was 1 μm and the 1.8 μm wide frame of metal 2 had a 2.2 $\times$ 2.2 μm square opening in this case.

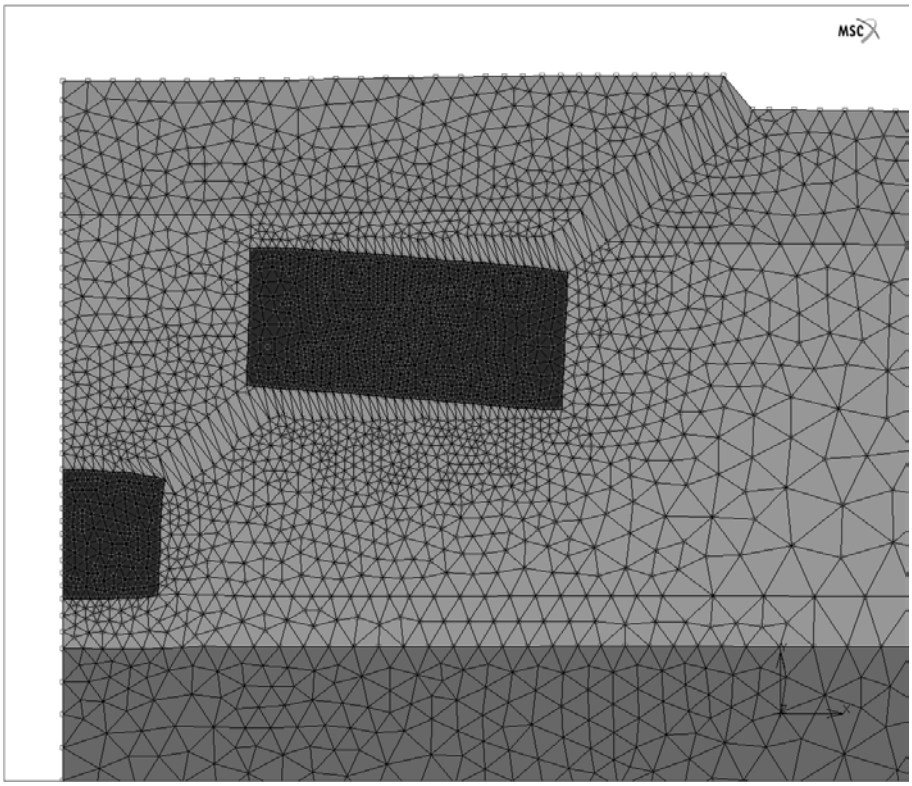

Figure 7.3: Results of finite element analysis showing passivation cracking caused by a laser energy above the high end of process window, scaled link structure with 0.5μm M1 and M2 frame with 1.5$\times$1.5 μm square opening, 0.6.μJ, spot size : 2.1μm in 1/e^2 diameter.

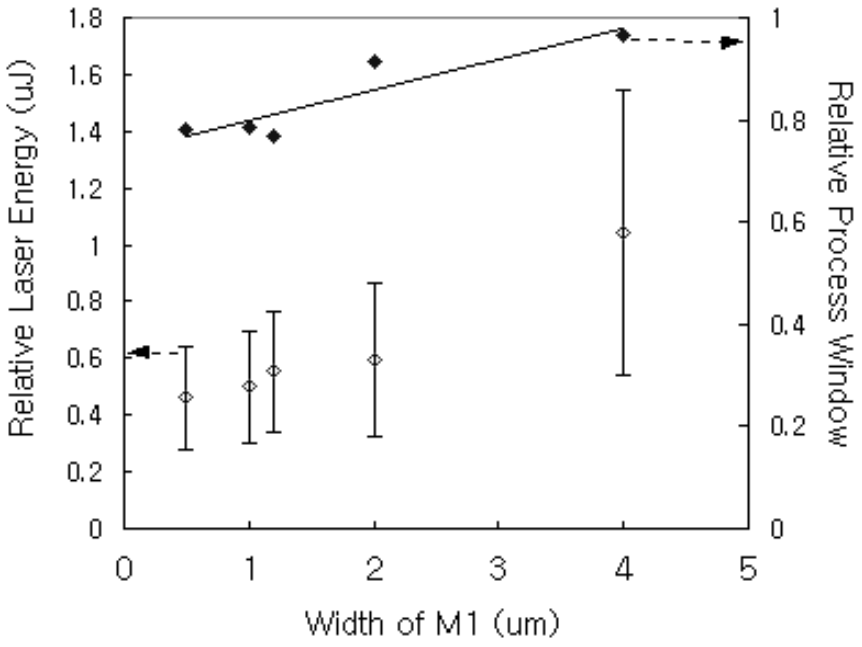

Figure 7.4: Simulation results of make-linking showing relative process windows and calculated available energy ranges for different link structures.

Figure 7.4 shows the simulation results showing the relative process windows and calculated available energy ranges for various make-link strucutres. The decreasing trend of relative process window with shrunken links is consistent with the experimental results shown in Figure 7.2.

The relative process window results from simulations were increased for very small structures since larger energy is needed to break the passivation with a smaller metal 2 frame. It is noted that the widths of metal 2 frame was scaled into 1.8 and 0.5 μm for 1 and 0.5 μm metal 1 line respectively while the width of other structures was 2 μm. Therefore, an excessive material loss in the lower metal line is the failure criterion for the high end of the process window for very small links rather than the passivation cracking.

The simulation results with a various size of vertical metallic make-link structure compared with experimental results are displayed in Figure 7.5. It shows only the relative process windows for each structure from both experiments and simulations. The graph demonstrates clearly that simulation results are very consistent with the trend of the decreasing relative laser energy window with a decrease of link structure size.

The normalized energy window extrapolates to no less than 0.75 for a zero width metal 1 line in case of experimental results. Simulation results show that a value of approximately 0.73 was extrapolated for relative energy process window of a zero width metal 1 line. The difference may be induced by other practical factors such as lens effect. As a result of both experiments and simulations, there appears to exist an acceptable energy process window for any scaled links as long as the lower metal line can share the metal with the resulting link sheet. Another key factor is the smallest spot size and the alignment accuracy that the laser system can make. Simulation suggested that the spot size used in each linking process played an important role in deciding the process window. It was found to be important to decide the absorbed energy by metal 2 as well as that by metal 1 to have a broad process window. Efforts have been made to find the optimum ratio of the absorbed energy densities within metal 2 to metal 1, and the ratio was found to be around 40 % to 50 % as determined by simulations.

We have learned that the laser energy absorbed in upper metal frame helps cracking from the upper corners of metal 1 and lead them to the right lower corners of metal 2. However, too much energy absorbed in upper metal frame will induce earlier passivation cracking, thereby decreasing the high end of process window. From simulations, it was observed that smaller energy absorbed in

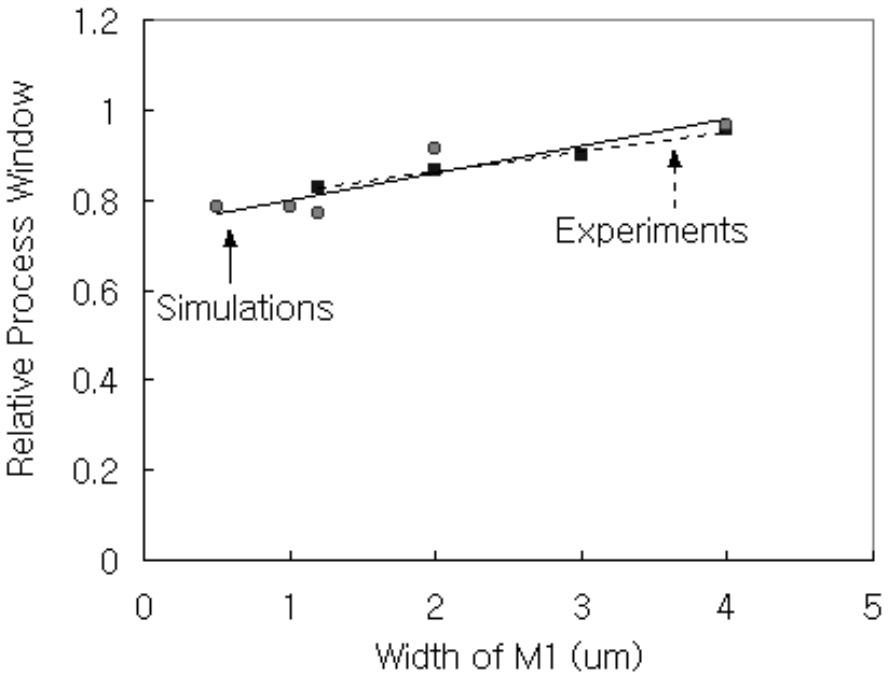

Figure 7.5: Simulation results of make-linking showing relative process windows and calculated available energy ranges for different make-link structures.

metal 2 frame than a specific ratio of energy densities absorbed by two levels of metallization caused another failure mode by cracking at a different point in the passivation, the center of metal 2 opening. This can be considered as the passivation damage caused by the lower metal cracking mixed up with upper corner cracking from metal frame in the direction of the metal 2 opening. This failure was not experimentally observed because all structures were irradiated by laser pulses with the spot size equal to about twice the width of each lower metal line in order to have a uniform temperature distribution throughout the top surface of metal 1. Therefore, this does not bring the less ratio of energy density absorbed in metal 2 which might otherwise cause the different failure mode.

In case of large links (structures with 2, 3, or 4μm wide metal 1 line), a ratio of around 50% was found give the most broad process window. For scaled links (1.2μm, or 0.5μm wide metal 1), a ratio of 40% or so was sufficient for the ratio of energy density in metal 2 to metal 1. This is because more energy needed to initiate the cracking from metal 1 with a smaller line width. Assuming Gaussian distribution in TEM_{00} mode, the irradiance at a distance from center, r, is described by

$$I_r = I_0 \times exp(-2r^2/w^2) \tag{7.1}$$

- w : Spot size in $1/e^2$ diameter.

Based on this equation, the optimum spot size can be decided from the ratio of energy density on the surface of metal 2 to that of metal 1. Table 7.1 shows the spot sizes used for simulations of various links to get broad process windows. It is noted that all the values in the table were calculated based on the 2-dimensional finite element models. The values for density in each metal can give the relative ratio of each energy density to the other other. And the values for absorption in each metal show the percentage of laser energy absorbed in each metal to the total effective energy. Lens effect was ignored in these calculations and the substrate damage from the gap was assumed to be negligible.

The spot size was selected to find the specific ratio of energy density ratio of metal 2 to metal 1, around 40% to 50% and this was the criterion in the decision of spot size. Figure 7.6 displays the optimum spot sizes in $1/e^2$ diameter for various widths of metal 2 opening in make-link structures, obtained from the results of simulations. The equation 7.2 is a simple equation to evaluate the optimum spot size in $1/e^2$ diameter acquired from the curve in Fig 7.6.

Table 7.1: Laser spot size used for simulations (unit : μm)

W_{M1}	Gap	W_{M2}	Spt $1/e^2$	Abs in M1	Abs in M2	Density Ratio in 2-D Model
4	1	2	7.2	0.46	0.23	0.5
2	1	2	4.8	0.30	0.24	0.5
1.2	0.5	2	3.1	0.26	0.36	0.4
1	0.5	1.8	2.7	0.24	0.34	0.4
0.5	0.5	0.5	1.6	0.19	0.15	0.4

- W_{M1} : Width of metal 1 line.
- Spt : Spot size in $1/e^2$ diameter.
- Abs : Ratio of energy absorption in each metal line to total effective laser energy.
- Density Ratio : Relative laser energy density ratio on the top surface of metal 2 frame to that of metal 1 line in 2-D model.

$$S_{opt} = 1.24 \times W_{opening\ of\ M2} \tag{7.2}$$

- S_{opt} : Spot size in $1/e^2$ diameter.
- $W_{opening\ of\ M2}$: Width of square opening of metal 2 frame.

Equation 7.2 demonstrates the importance of laser system ability to decrease the spot size with acceptable alignment accuracy for the processing of scaled links. However, considering the lens effect due to the step of unplanarized passivation, the acceptable spot size is considered to be a little bigger than the calculation value for each structure.

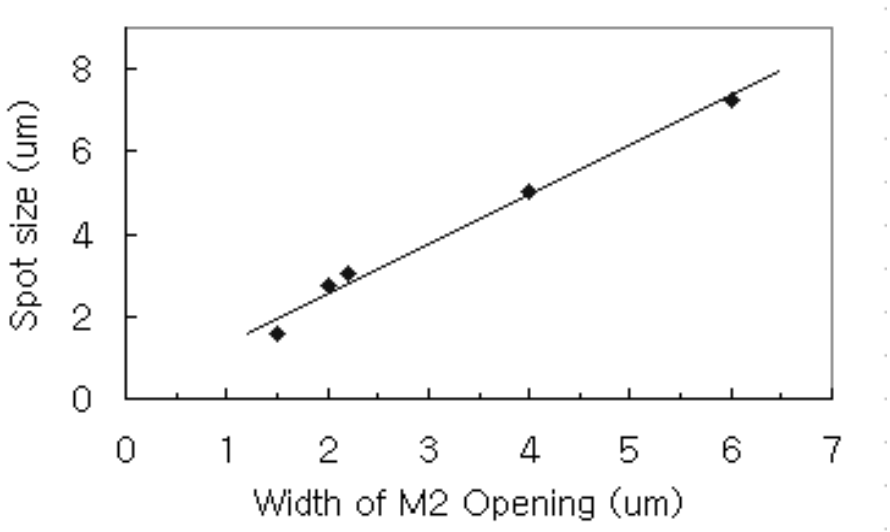

Figure 7.6: Optimum spot size calculation, spot size in $1/e^2$ diameter.

Using GSI Lumonics $M430$ laser system, experiments with various spot sizes (1.7, 2.3, 3.1, 4.1 and 6.2 μm $1/e^2$ diameters, 5 μm was not available) performed on a link structure with 2 μm wide metal 1 line and 4×4 μm square opened metal

2 frame. Links processed with 4.1 μm showed the highest yield throughout the energies as expected from the simulation results.

Modern IR laser systems are being designed to focus a round $1/e^2$ spot size as small as 1.7 μm or less in diameter with an alignment accuracy of less than 0.3 μm and the spot size trend is to decrease even more. Therefore, these spot size and alignment accuracy would enable the scaled link with 0.5 μm wide metal 1 line and 1.5 $\times$ 1.5 μm metal 2 square opening to be possible for linking with an acceptable process window.

In this chapter, it has been experimentally shown and extrapolated by calculations that the make-link is seamless for the application to current VLSI technology. Finite element modeling was performed and the results were consistent with the calculations. In addition, the current trend in semiconductor industry to increase the thickness of metallization will keep the make link technology viable even for the future technology. In the following section, dense layout with scaled link structures will be presented.

7.4 Dense Link Structure

We have shown from the aforementioned calculations and simulations that the scalability of a vertical link structure is capable of practical restructuring application in the increased circuit density. On the other hand, it is also important how to layout the structures in order to increase the interconnect density.

To improve the interconnect density, we propose two newly designed layouts of link structures consisting of two different levels of metallizations. Figure 7.7(a) displays a single metal 2 line can be connected to any metal 1 line, while Figure 7.7(b) illustrates each metal 2 line can be connected to every other metal 1 line

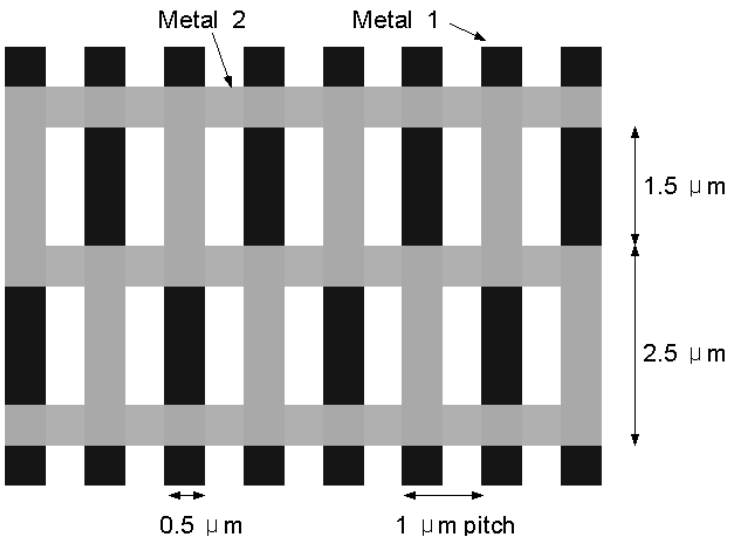

(a)

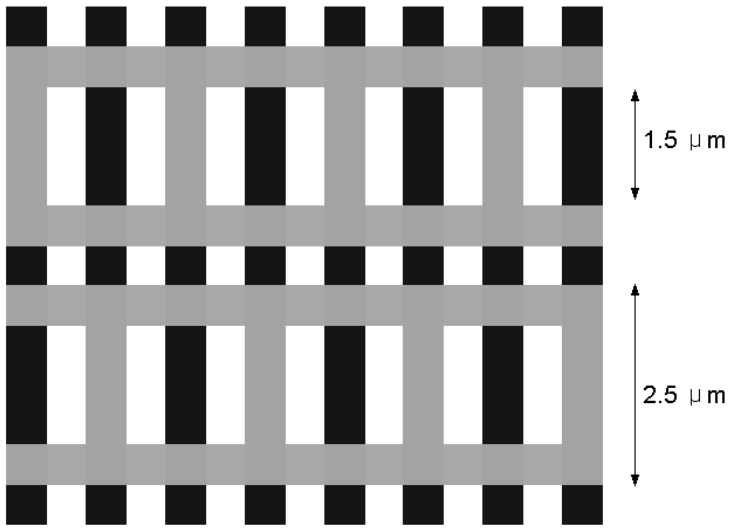

(b)

Figure 7.7: Dense layouts of vertical link structure showing a possible 1μm metal 1 pitch, (a) layout of a single bus and (b) layout of complimentary links.

by forming a link at the crossing link structure.

Each link region consists of a 0.5μm wide metal 1 line and a 1.5×1.5 μm square frame of 0.5μm wide metal 2. Parallel lines of metal 1 are spaced at a 1μm pitch for both layouts and the pitches of metal 2 are 5μm and 3μm for (a) and (b), respectively.

The size of square hole in the metal 2 frame has been decreased from the designs of the test wafer in order to illustrate a maximally dense link region that will assure that metal 1 would terminate on metal 2. The decreased spot size of modern IR laser systems would enable the 1.5×1.5 μm square hole to be possible for linking with an acceptable process window. Furthermore, green laser systems can be focused to a 1μm spot size or so in diameter, thereby, allowing further scaling potential. Therefore, the link structures in the layouts in Figure 7.7 is expected to be a practical and seamless application as antifuse layouts in modern IC design.

Chapter 8

Applications of Vertical Make-link to Laser Programmable Multichip Module

8.1 Introduction

The MCM approach to electronic packaging has improved the system performance by bridging the gap between the current packaging technology and the advanced IC technology [1]. However, the time required to complete the design of a full-custom MCM can be long and the process can be expensive [3]. A complete custom design of an MCM is a task that requires long time and large effort. As a result, programmable multichip modules(PMCMs) have been introduced in order to minimize the time-to-market and reduce the cost.

PMCMs are in a way similar to field programmable gate arrays(FPGAs). FPGAs are devices that are programmed by a user to implement a logic function while PMCMs are programmed to implement only the interconnection. The first step in the development of a PMCM is to prefabricate the substrate in bulk. Each substrate is then customized to provide interconnection based on the specific circuit of the user. The customization process has been carried out by

using electrically programmable switches or by mask programmable techniques.

The main difference between a PMCM and an MCM lies in the way the interconnect wiring is fabricated. Programmable version of the MCMs come with prefabricated interconnect layers with provisions to customize the design based on the user's needs.

8.2 Multichip Modules

At present, there is much interest in raising the capability of integrated circuits by increasing the area of a single-circuit system from the current chip size of about 1 cm^2 to devices that are greater than 10 cm^2. This effort has come to be known as wafer scale integration (WSI). WSI is achieved by interconnecting the operable circuit elements while avoiding the defective ones [51]. As a part of WSI, one promising application in chip repair systems lies in Multichip Modules customization system.

The need in electronic systems of higher clock speeds, lower power consumption, and greater compactness of functionality have led to the wider use of multichip modules (MCMs). The MCM is a new packaging approach in which multiple bare chips are mounted and interconnected on a substrate using layers of conductive and dielectric thin films [52]. Since the substrate, or the chip carrier, has substantially finer conductor lines, smaller dielectric thickness, and denser via grid than the board, they are not subject to the conventional printed circuit board (PCB) design rules and assembly restrictions. Correspondingly, a chip carrier that has only one chip in it is called a single chip module(SCM) [1].

The traditional approach of using single chip packages on PCBs has intrinsic limitations in terms of silicon density, system size, and contribution to propa-

gation delay. If a PCB were completely covered with chip carriers, the board would only have at most a 6% efficiency of holding silicon. In other words, 94% or more of the board area would be wasted space, unavailable to active silicon and contributing to increased propagation delays [1].

With the emergence of VLSI technology, the demand for higher performance and packaging efficiency has increased. The need for high performance system packaging will be met by the developments taking place in multichip modules (MCMs). MCMs provide a very high level of system integration, with hundreds of bare IC chips that are placed very close to each other on a single high density substrate. Elimination of single chip packages can often lead to 10 times higher I/O terminal density at the substrate level and drive demand for increased interconnect density in order to achieve suitable connectivity [53]. As a result, MCM based systems can result in much denser circuits and much shorter interconnect distances among the bare chips. Once suitable interconnect density is realized, the quantitative benefits of MCMs can increase system performance and reduce system area and weight.

The performance gain is due to the reduction in signal delay as the interconnect distances between the bare chips is far shorter than the distances between the chips on a PCB. The reliability improves because there are fewer package levels. The size and weight are reduced since the packages of the individual dies are eliminated. In addition, MCMs can also remove a larger amount of heat and provide a large number of I/Os. Due to these features, MCMs have significantly enhanced the performance and reliability of the end-products. MCMs are therefore considered critical for the development of all computing systems, especially high performance systems. Figure 8.1 shows the diagram of a typical multichip

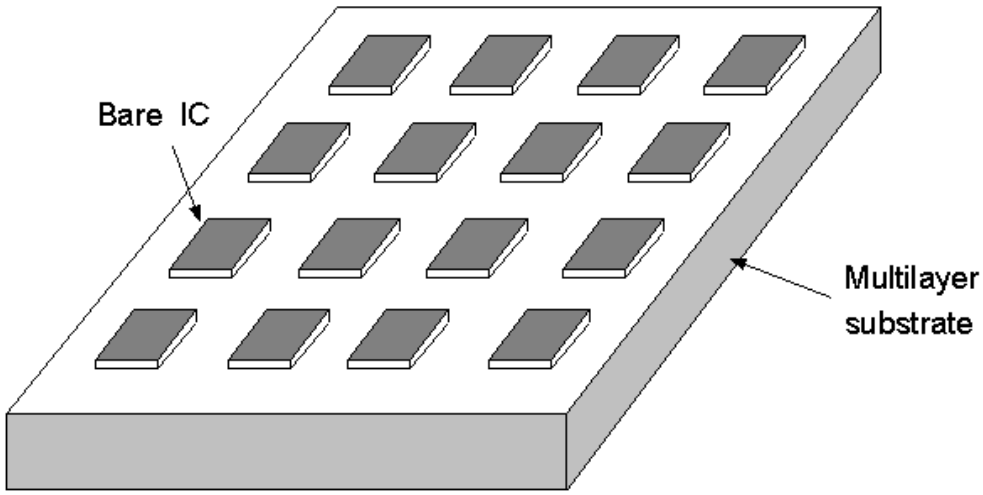

Figure 8.1: A typical multichip module

module.

The main differences between MCMs and other package types (PCBs and SCMs) are the substrate and dielectric materials used and the component mounting and bounding methods employed by MCM manufacturers [52].

The substrate is used for supporting the dies as well as the media for the interconnections among the dies. The interconnections among the dies are made using metal wires that are laid out on layers called signal planes in the substrate. Typically, different layers are used for making horizontal and vertical connections. Additional layers are provided for power and ground connections. The bare dies are attached to the substrate by chip bonding. The chip bonding technique determines how the electrical connections are made between the dies and the substrate. Figure 8.2 illustrates the chip bonding techniques currently used in the industry.

The most commonly used chip and wire bonding method (see Figure 8.2 (a))

is the most reliable one among the three methods. But the procedure is slow and expensive for components with high pin counts. Therefore, it is typically not considered for high volume production. This technique also restricts wire densities because of the larger pad sizes and spacing required for the bonding tool head.

Tap Automated Bonding, as shown in Figure 8.2 (b), is slightly more automated, but requires more effort during MCM design layout.

Flip-chip bonding method, as in Figure 8.2 (c), is becoming prevalent among MCM manufacturers because of its cost effectiveness and among packaging engineers because of optimized circuit densities and enhanced electrical performance. It also permits great chip densities on substrate areas and subsequently, significantly reduced overall circuit inductance and signal delay [52].

The electrical connections between the dies and the substrate are called chip I/Os. Like an SCM, an MCM is packaged to protect it from the hostile environment. In addition, some cooling methods must be used to remove the heat generated by the dies. Electrical connections between the MCM and the outside world such as a PCB are needed to transfer the signals on and off the MCM. Such electrical connections are called module I/Os.

Far from being passive carriers for microelectronics devices, the packages in today's high performance computers pose at least as many engineering challenges as the semiconductor chips that they interconnect, power, cool, and protect. While the semiconductor circuit performance as measured in picoseconds continues to improves computer performance is expected to be in nanoseconds for the rest of this century. The factor of 1,000 is attributable to the packaging. Thus the packaging, which interconnects all the chips to form a particular function, such

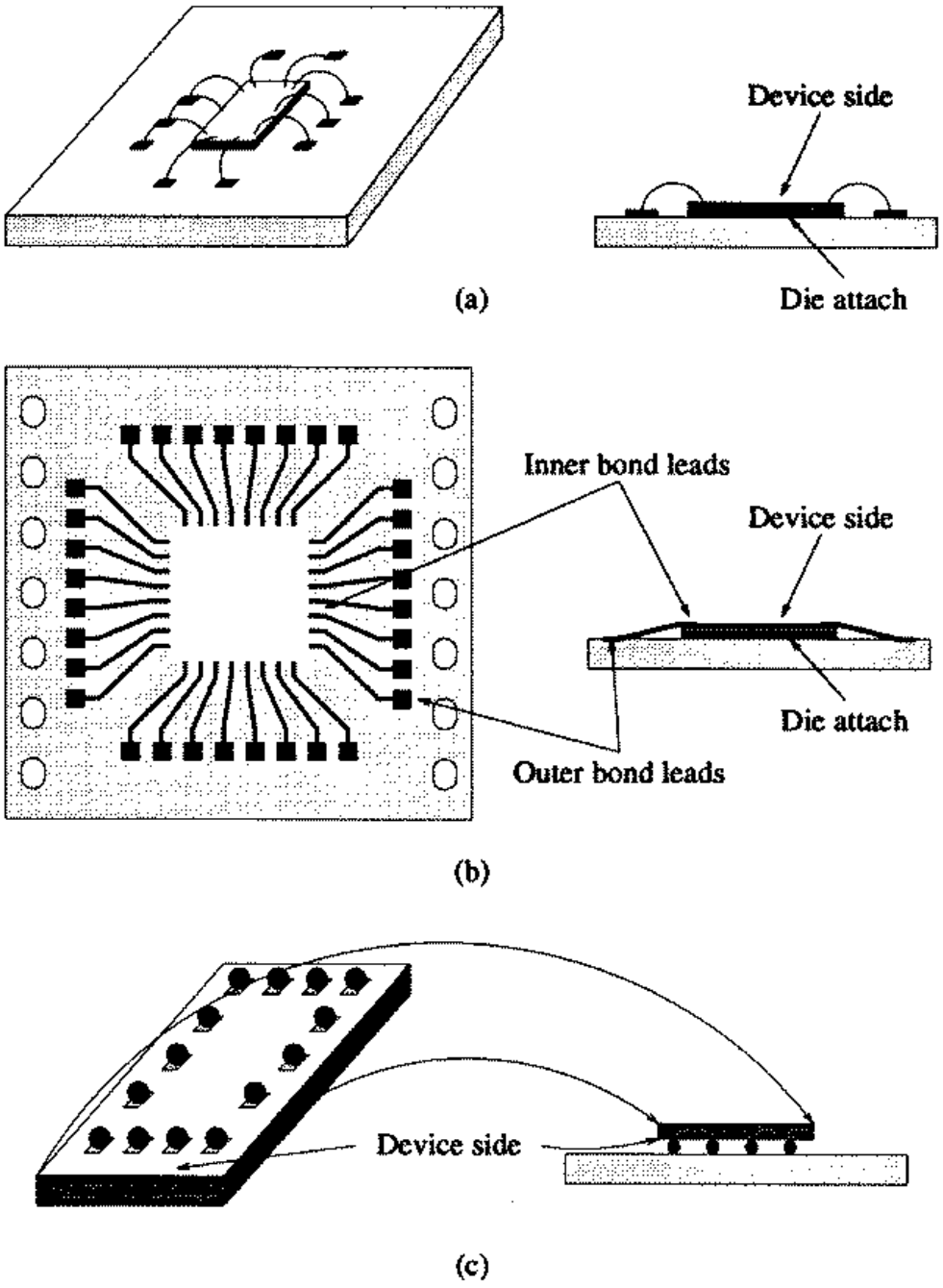

Figure 8.2: Die attachment techniques:(a)wire bonding, (b)tape automated bonding, (c)flip-chip bonding [1].

as a central process unit (CPU), is likely to set the limits on how far computers can evolve. Multichip packaging, which minimizes these limits drastically, is expected to be the basis of all advanced computers in the future. In addition, since this technology allows chips to be placed closer and to occupy less space, it has the added advantages of being used in portable consumer electronics and medical, aerospace automotive, and telecommunication applications. In sum, the advantages of MCMs include smaller size, less weight, better performance, and improved reliability. Due to these advantages, MCMs are finding many applications.

8.3 Classification of PMCMs

PMCMs can be classified as Fully programmable MCMs (FP-MCMs) and Semi-programmable MCMs (SP-MCMs). Electrically programmable antifuses have been in use for the FP-MCMs [1]. Antifuses normally act as insulators, but can be electrically switched to behave permanently as low-resistance conductors by applying a threshold voltage. Programming the circuit signal nets via the antifuse material allows designers to form chip-to-chip or chip-to-I/O circuit connections.

The construction of antifuses often differs from one device to another in subtle ways. Figure 8.3 depicts the cross-sectional view of a commercial electrically programmable antifuse [2]. This antifuse consists primarily of amorphous silicon which is vertically sandwiched between molybdenum-tantalum / aluminum-copper electrodes and horizontally confined by silicon dioxide. In off-state, the antifuse conducts a leakage current and highly conductive filament is established through the application of characteristic threshold voltage. This electrical antifuse technology has been widely utilized in the industry.

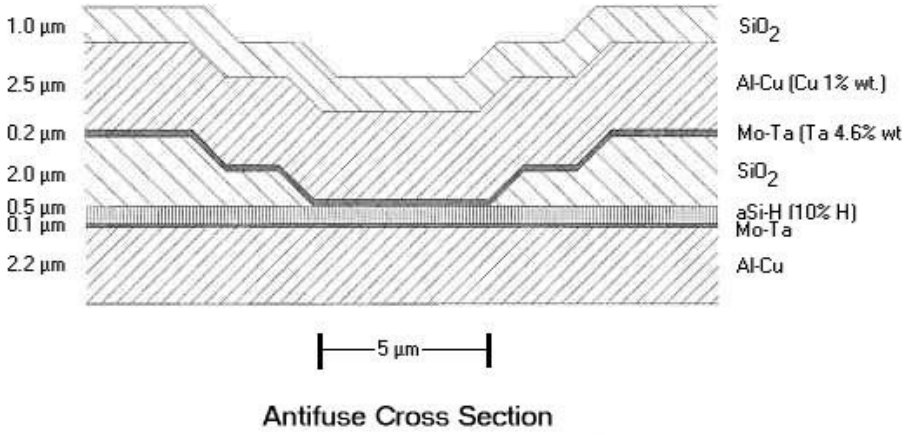

Figure 8.3: Cross-sectional view of electrical antifuse [2].

Figure 8.4 displays how an interconnection works between two chips mounted on the PMCM substrate using antifuse. ICs are connected to pads using wire bonding technique and the antifuses are programmed to connect the two ICs. The dark metallizations indicate the connection between two ICs and they are connected by programmed antifuses while light metallizations mean non-processed and not-connected.

Recently a fully programmable MCM that uses a laser programmable technique to connect two interconnects by way of antifuse was reported [3] and is detailed in the following section.

On the other hand, the SP-MCM technique borrows from the integrated circuit technique of prefabricating all or most of the circuit and later customizing the device to meet the application-specific needs of the user [53]. SP-MCMs are made of prefabricated blank interconnection arrays in copper polyimide (CuPi) substrate [1]. The substrate is then automatically routed by using a large number of interconnects based on a description of the die pad placement and a netlist.

The major design criteria of SP-MCMs are to prefabricate the initial layers

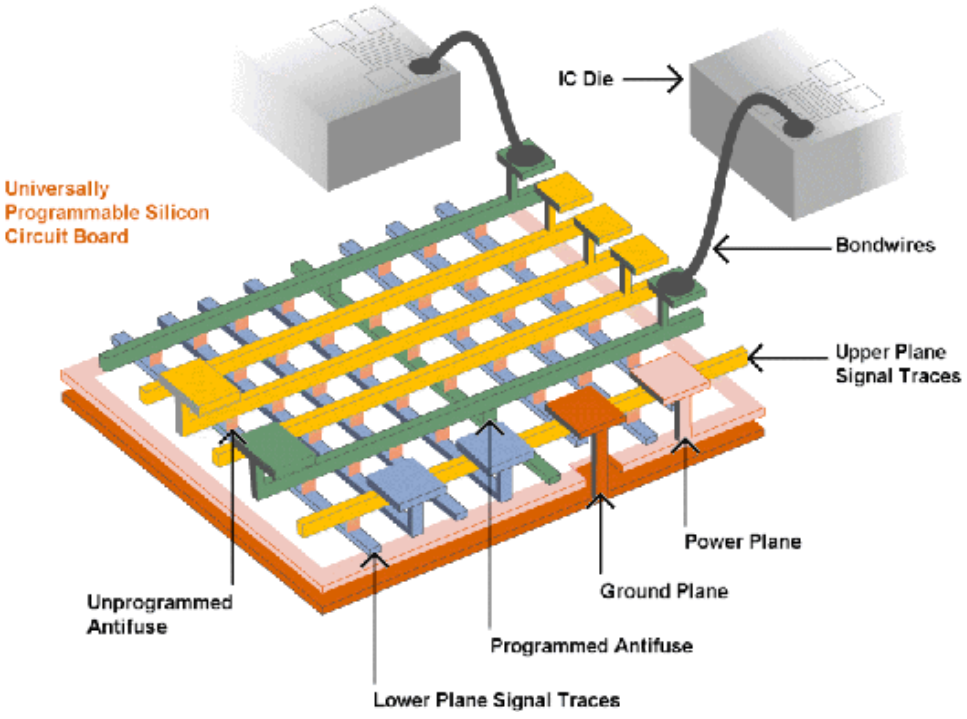

Figure 8.4: Drawing representing interconnection between bare IC chips

using mask fabrication and to customize the few layers of interconnection by user programming. The advantage of using the SP-MCMs are to achieve high yield and quick turn-around time. The cost for manufacturing is higher than FP-MCMs. Quick Turn-Around Interconnect (QTAI) technique is categorized as an SP-MCM.

PMCMs, especially FP-MCMs, have a trade-off which is that PMCMs are not suitable for very high performance applications due to the programmable nature of the substrate. Nonetheless, PMCMs are still greatly becoming attractive alternative to MCMs where fast turn-around and low cost are critical factors. In this chapter, the laser programmable technology adopting make-link technique in FP-MCM are detailed and new substrate designs are proposed.

8.4 Laser Programmable Multichip Module

A laser-programmable MCM(LPMCM) substrate has been built by R. Berger *et al.* in MIT Lincoln Laboratory [3].

In their work, a LPMCM is a silicon substrate with a dense, predefined array of pads, tracks, and links. Drawings in Figure 8.5 show (a) the appearance, (b) the detailed layout and (c) cross-sectional view of the MCM structure.

As shown in Figure 8.5(c), links consist of a silicon nitride layer sandwiched between the two metal layers . When a laser pulse of the correct power and duration is directed to the link region, the metal and the nitride fuse to form a conductive vertical path, with a resistance of typically 2 Ω. The tracks can also be cut by laser energy on the narrow places in the tracks, as can be seen in Figure 8.5(b), to isolate distinct nets and trim unwanted stubs from a net. Power, ground, and signals share the tracks on the two metal layers. The module

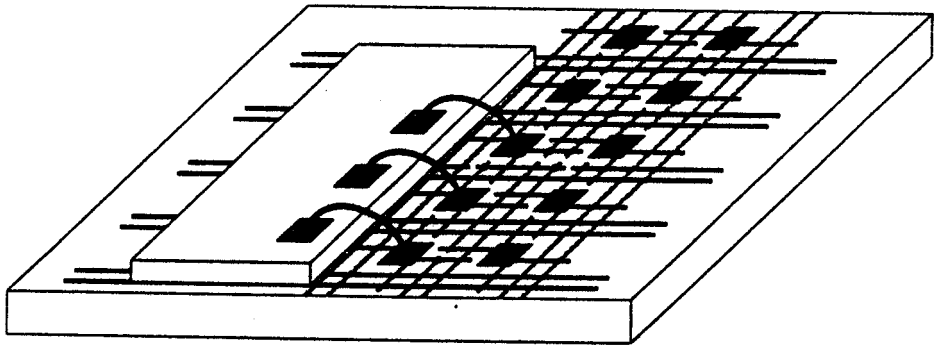

(a)

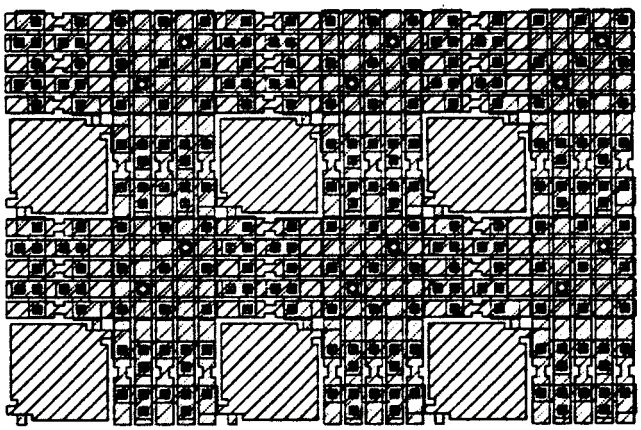

(b)

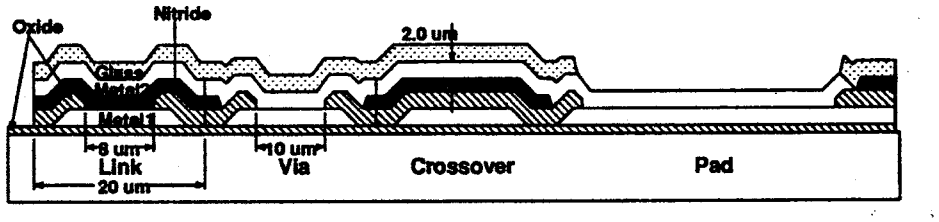

(c)

Figure 8.5: (a) The laser-programmable multichip module, (b) detailed layout of the MCM substrate, (c) cross-section of the MCM structure [3].

consists of an array of 258×258 pads with a pitch of 200 μm, and five tracks between any two adjacent pads. The substrates are manufactured in advance and then quickly programmed by laser to build particular systems.

However, there are some drawbacks to this link technology. Specifically, the size of link structure is relatively large and this vertical link method requires extra processing step. Reduction of link structure size, link yield and compatible processing steps are crucial elements for wide spread use of link technology [54, 35].

Considering these weaknesses of the previous link structure, the direct linking through molten aluminum by laser pulse can resolve the drawback issues of diffused link structure. The new designs of the MCM substrate utilizing MAGIC software, reflecting the improved make-link structure acquired by reliability test as proposed in [27], are presented in the following section.

8.5 Reliability of Vertical Make-link

Accelerated life tests have been performed to evaluate the electromigration reliability of vertical links by W. Zhang et al. [27] In that work, we have shown that the links exhibit a commercially acceptable lifetime (38 years at room temperature with constant current density of 3.0 MA/cm^2). It has also been shown that lifetime vs. laser energy relation is found in agreement with the resistance results. Figure 8.6 displays the results showing lowest electrical resistance corresponding to the highest lifetime in case of vertical link with 6x6 μm metal 2 frame hole and 4 μm wide metal 1 line [27].

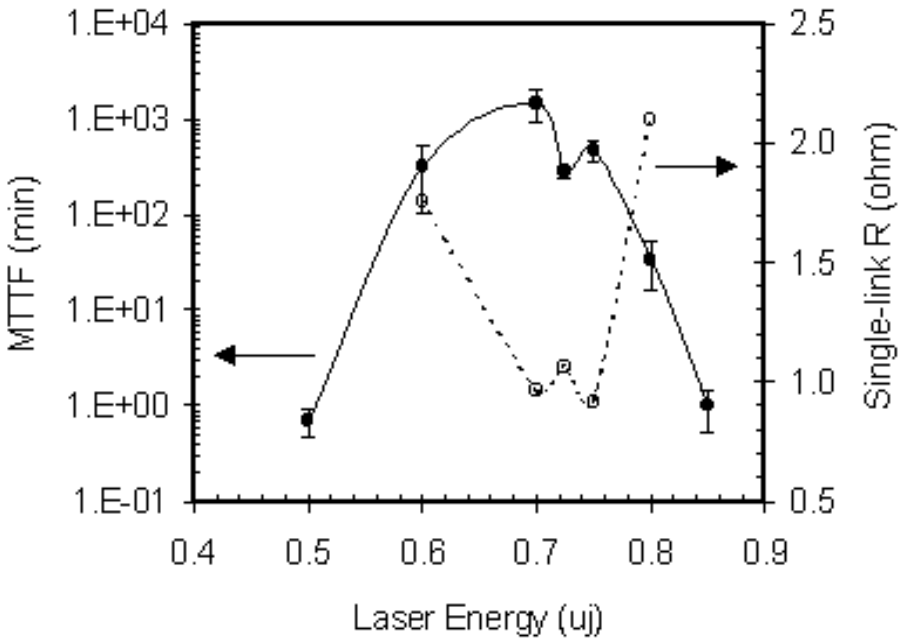

Figure 8.6: Lifetime vs. laser energy in comparison with the energy dependence of single-link resistance.

Moreover, we have learned from FIB image analyses that electromigration occurs not only in the links but also elsewhere including the metal 1 line and the metal 2 frame. In particular, the void produced in metal 1 due to the transport and re-solidification of molten metal during the link formation is considered to be an intrinsic defect of the process which poses reliability concern [27]. Based on the FIB observations, a modified structure was proposed to improve the electromigration reliability as portrayed in Figure **??** and it is used in the design of vertical link structure in the LPMCM substrate. It is expected that this new vertical link structure will have the sufficient reliability for practical implementation on LPMCM substrate design.

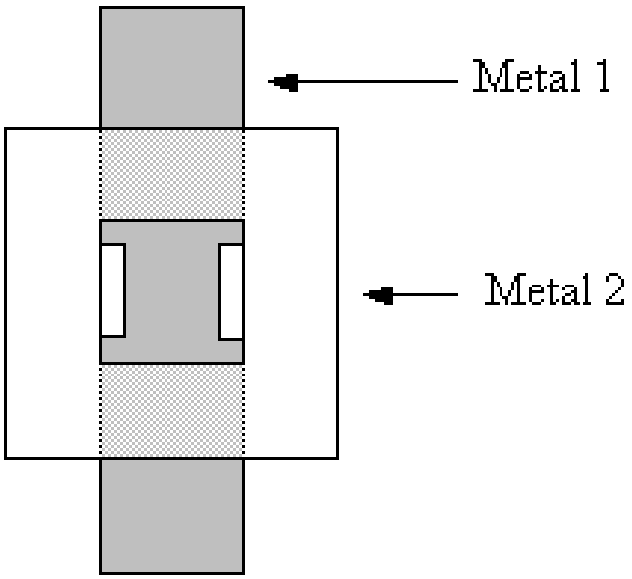

Figure 8.7: An improved vertical link structure considering Blech effect in the metal 1 lower metal line.

8.6 Designs of Substrate

The substrate is built to have a dense, predefined array of pads, metal tracks and links. The aforementioned vertical link technique is utilized for the patterning of wiring connections between pads on the substrate.

After the linking process, integrated circuit chips are mounted, circuit side up, on the substrate, and the chip pads are wire-bonded to the substrate pads by thermal compression. Therefore, the substrates can be manufactured in advance and then quickly programmed by laser within a few minutes to build user-specified systems. When a wiring net has been formed by laser pulses, its completeness and its isolation from other nets may be verified with the aid of a mechanical probe that can make electrical contact to any chosen pad.

The LPMCM substrate, used for supporting the dies as well as the media for the interconnections among the dies, is made on 10 cm silicon wafer and contains 2,281 or 2,863 pads/cm^2 and many tracks of two layers of metal. The substrate can be diced into any size needed to accommodate a given requirement. Figure 8.8 schematically illustrates a layout of a substrate made up of 32 big segments.

The following sections describe its design step by step from the link structure to the whole substrate. It is noticed that thicker metal gives lower resistance and thicker insulator gives lower capacitance, both of which improve the speed of propagation of signals across the module [3]. These depend on the quality of the fabrication processing.

8.6.1 Links

Two prototypes of LPMCM substrate have been designed using the vertical link structure and the detailed designs of linking regions are depicted in Figure 8.9

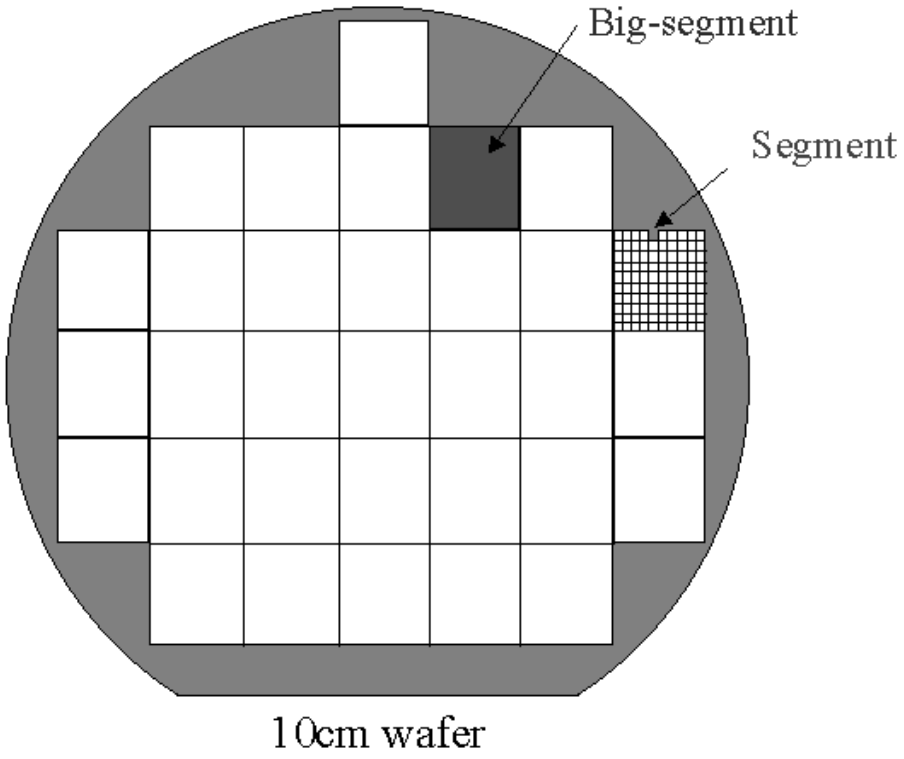

Figure 8.8: The layout of a whole substrate consisting of 32 big segments.

and Figure 8.10. Link structures are arrayed so that they can be formed at any of the intersections of vertical tracks with horizontal tracks around every pad on the substrate. In all the figures of designs through this work, east-west tracks are on the second level of metal (metal 2), north-south tracks on the first level (metal 1).

Figure 8.9 illustrates the vertical link structure with 6 μm wide metal 2 frame with a 8x8 μm square hole aligned to the underneath 6 μm wide metal 1 line (single link). The dark vertical lines indicate metal 1 lines while the light horizontal lines is the metal 2 lines.

Figure 8.10 shows the doubled vertical link structure (double link) with 4 μm wide metal 2 frame with a 6x6 μm square hole aligned to the underneath 4 μm

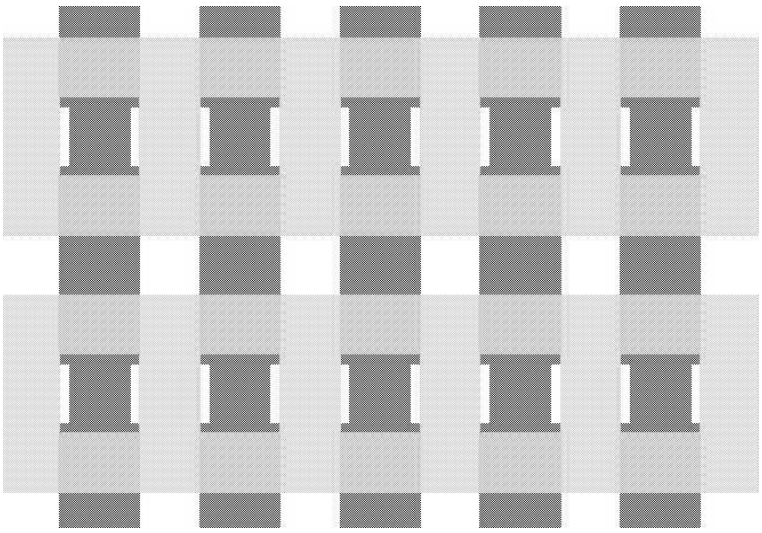

Figure 8.9: Single link structure used in LPMCM substrate (8×8 μm^2 square hole metal 2 frame and 6μm metal 1 line).

wide metal 1 line for a vertical linking region. One connection between metal 1 and metal 2 is made up of two vertical link structures as can be seen in the figure. This double link structure has been designed to decrease the resistance of each connection between metal 1 and metal 2 and improve the reliability. To improve the metal 1-void limited reliability, a newly suggested vertical link structure proposed in [27] has been illustrated for the both designs.

8.6.2 Pads and Metallizations

Figure 8.11 and 8.12 illustrates the arrayed pads and metallizations around them. There are 7 tracks of metal 1 line sideways and 5 tracks of metal 2 line lengthwise between any two adjacent pads in the single link design, Figure 8.11. On the other hand, 5 tracks of metal 1 line or metal 2 line are available for routing any pads together in case of double link design as shown Figure 8.12.

The emphasized metal tracks emanating in four directions from the center

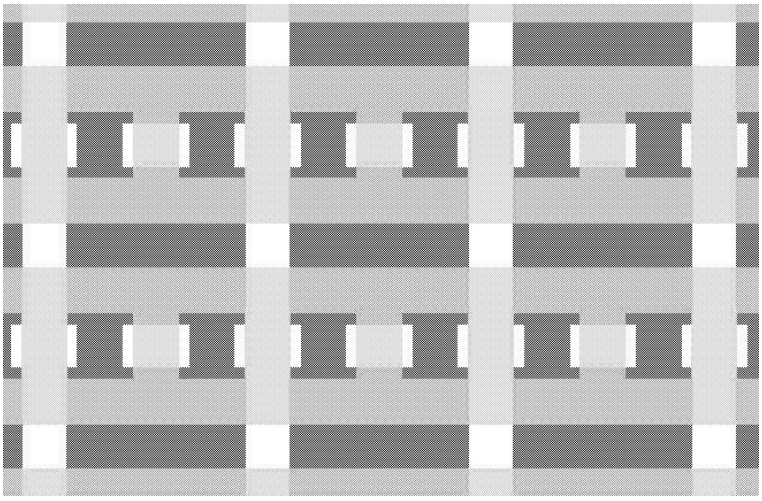

Figure 8.10: Double link structure used in LPMCM substrate (6×6 μm^2 square hole metal 2 frame and 4 μm metal 1 line).

pad in both figures Figure 8.11 and 8.12, and they indicate the metal lines pre-connected into the pad through direct metal contacts. Every pad has the same structure in which the pad is pre-connected to both metal 1 and metal 2 lines around it and the connections enable the pad to interconnect to any other pad through east-west and/or noth-south metal lines.

In the single link design, three tracks of metal 1 line and one track of metal 2, but doubled, are available to connect a pad to any metal lines around it. Therefore, triple links can be formed from a pad to any east-west metal 2 line around it and double links can be made between any pad and any nearby north-south metal 1 line. Those multiple linking to connect a pad to a metal line are designed in order to improve the electrical resistance and the reliability.

In case of Figure **??**, quadruple links are feasible from a pad to a nearby east-west metal 2 line through 2 tracks of metal 1 line pre-connected into the pad, and triple links can be made between a pad and a nearby north-south metal

1 line through the pad-preconnected metal 2 track. The pads are 62×54 μm rectangular-shaped and spaced at 182 μm horizontal and 210 μm vertical pitch for single link design, and 60×56 μm big and 180 μm horizontal and 166 μm vertical pitch for double link one.

8.6.3 Segment

The two figures in Figure 8.13 and 8.14 display the repeating segments consisting of the pads and metallizations around them.

Instead of arraying all the pads evenly without segments throughout the whole substrate, 5×5 pads are separately bundled as a segment in order to increase the routability and decrease the capacitance caused by unnecessarily long tabs. This will give enough routability between any pads within a segment since no connection exists originally between any segments and there is no overlaped usages of metal tracks with other segments.

In order to connect two metal tracks from two different and adjacent segments, metal tabs of either metal 1 and/or metal 2 with double links are designed around the edges of both segment designs in Figure 8.13 and 8.14. The metal 1 tracks in the top and bottom of each segment are modified so that the metal 2 tabs for the connections between segments can be arrayed evenly. Figure 8.15 displays how segments and big-segments which is explained in next section are connected each other using metal tabs. Numbering of pads around every segment has been done in order to help identify the location of any pad.

The sizes of a segment are 1098×972 μm and 900×970 μm for the single link and double link designs, respectively.

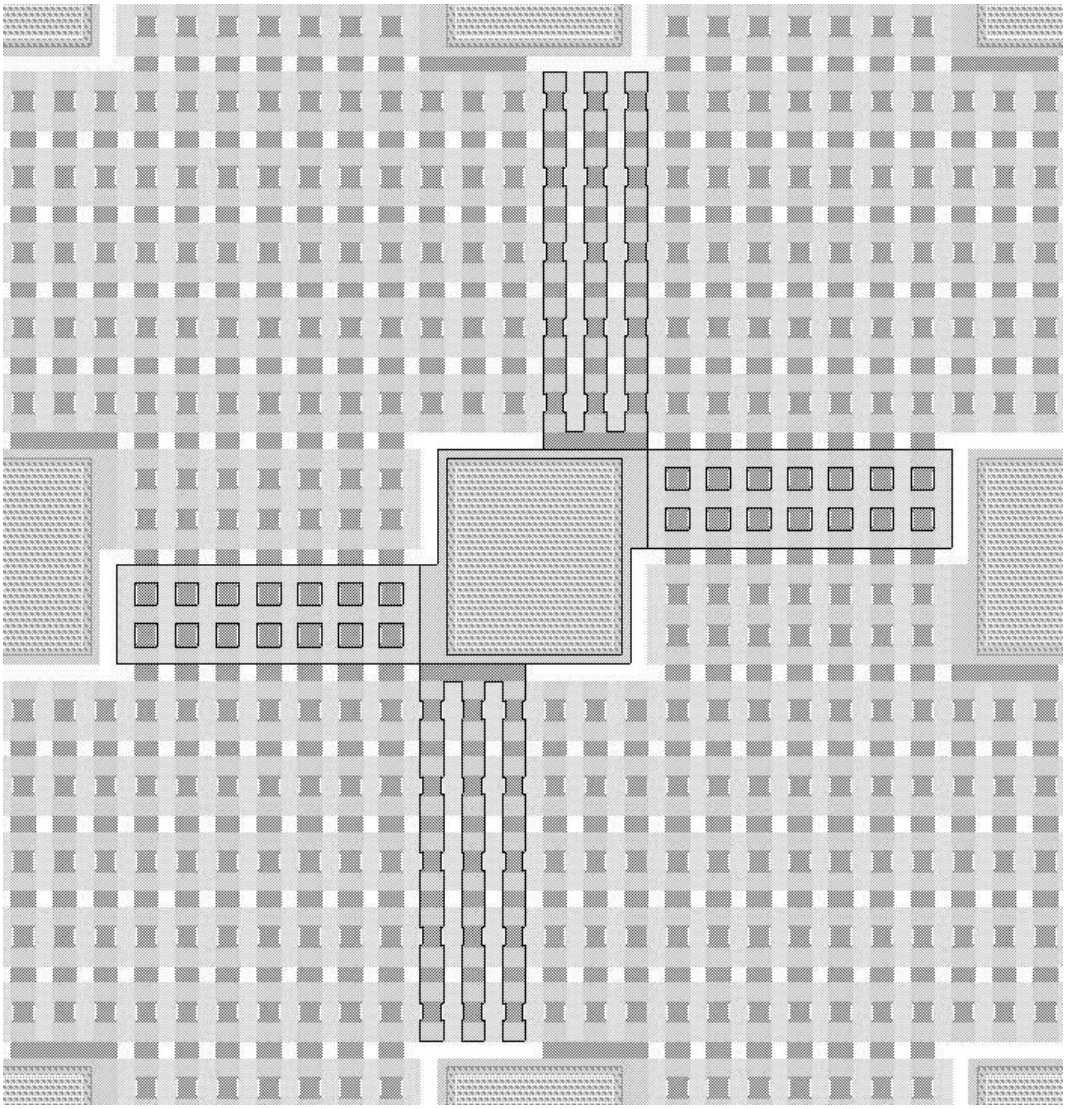

Figure 8.11: The layout of pads and metallization showing the connecting tracks from a pad in LPMCM substrate which adopts single link structure.

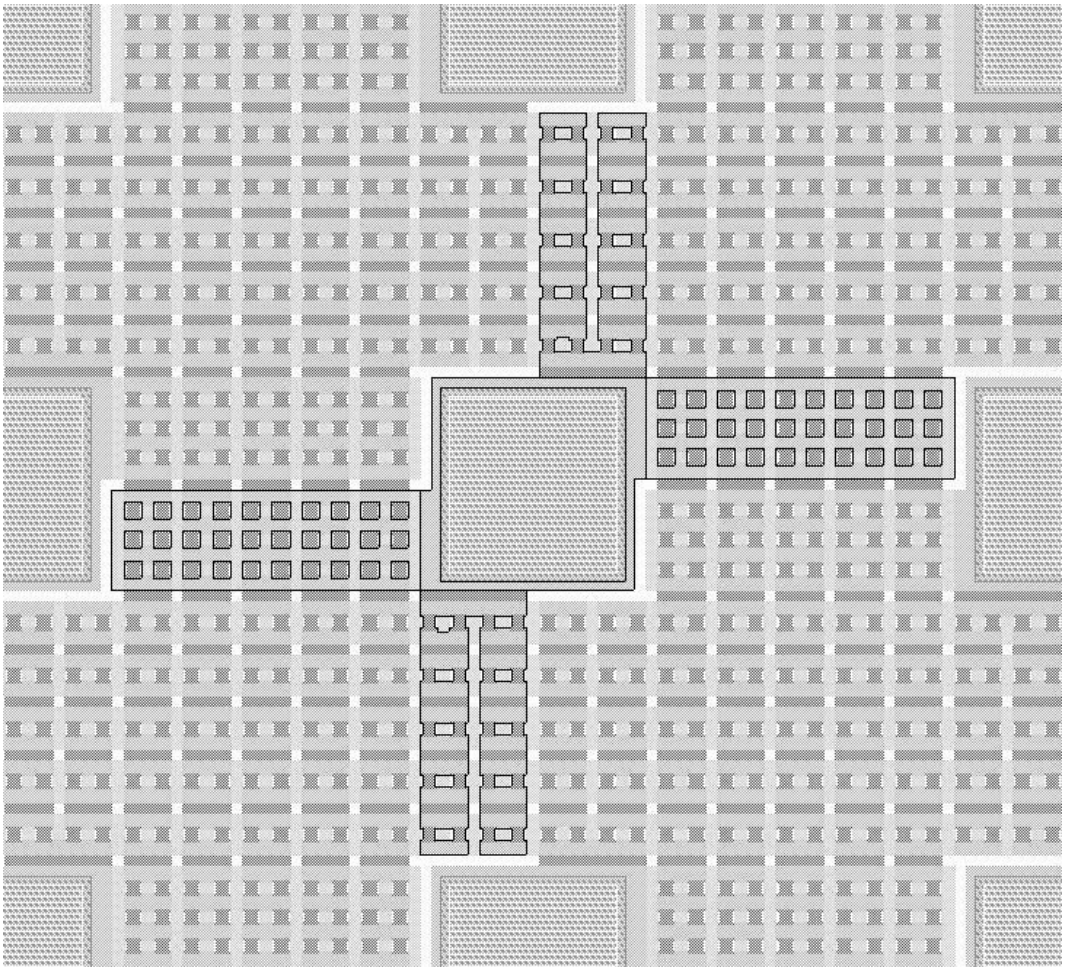

Figure 8.12: Top layout of pads and metallization showing the connecting tracks from a pad in LPMCM substrate which adopts double link structure.

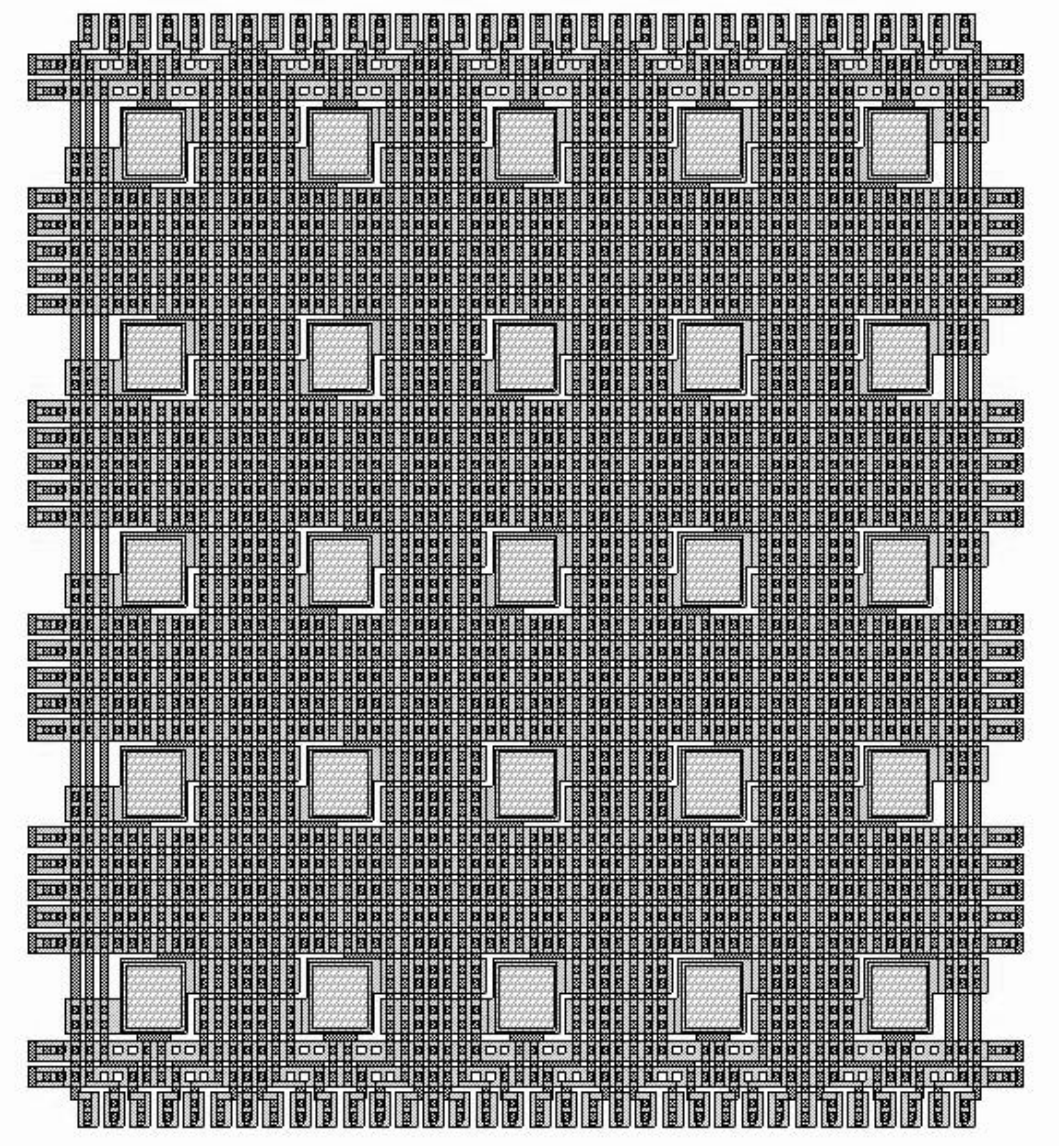

Figure 8.13: Top view of segment with 5×5 pads, single link design.

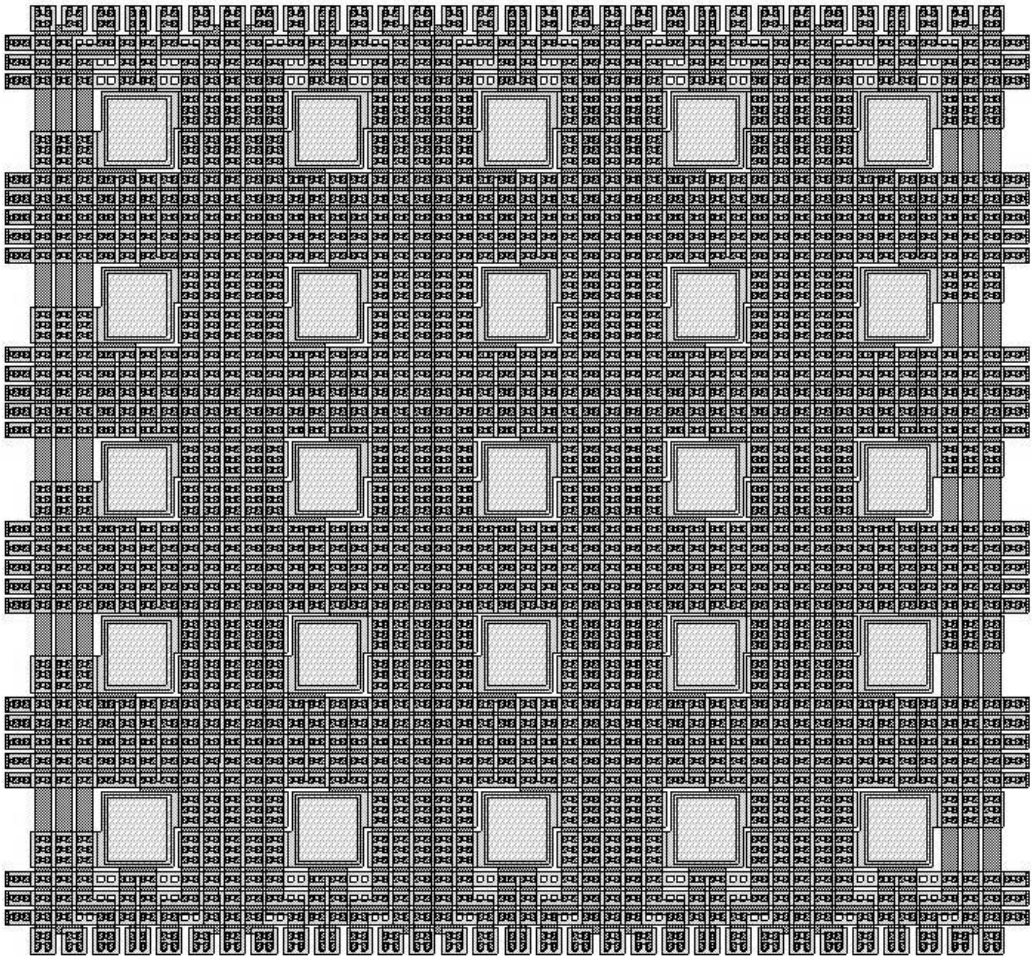

Figure 8.14: Top view of segment with 5×5 pads, double link design.

8.6.4 Big-Segment

A big-segment is an array of 10×10 segments and any two of adjacent big-segments can be connected through the metal tabs which are similar to the metal tabs between segments but much longer than those as can be seen in Figure 8.15. Every corner of a big-segment has a laser alignment mark to increase the laser alignment accuracy. We can notice which big-segment we look at by reading the capital alphabets around the big-segment.

The substrate includes 5×5 big-segments each of which consists of 10×10 segments; thus, there are 2,500 segments in total. This allotment of a substrate into 25 big-segments is done due to the same reason with the case of segments.

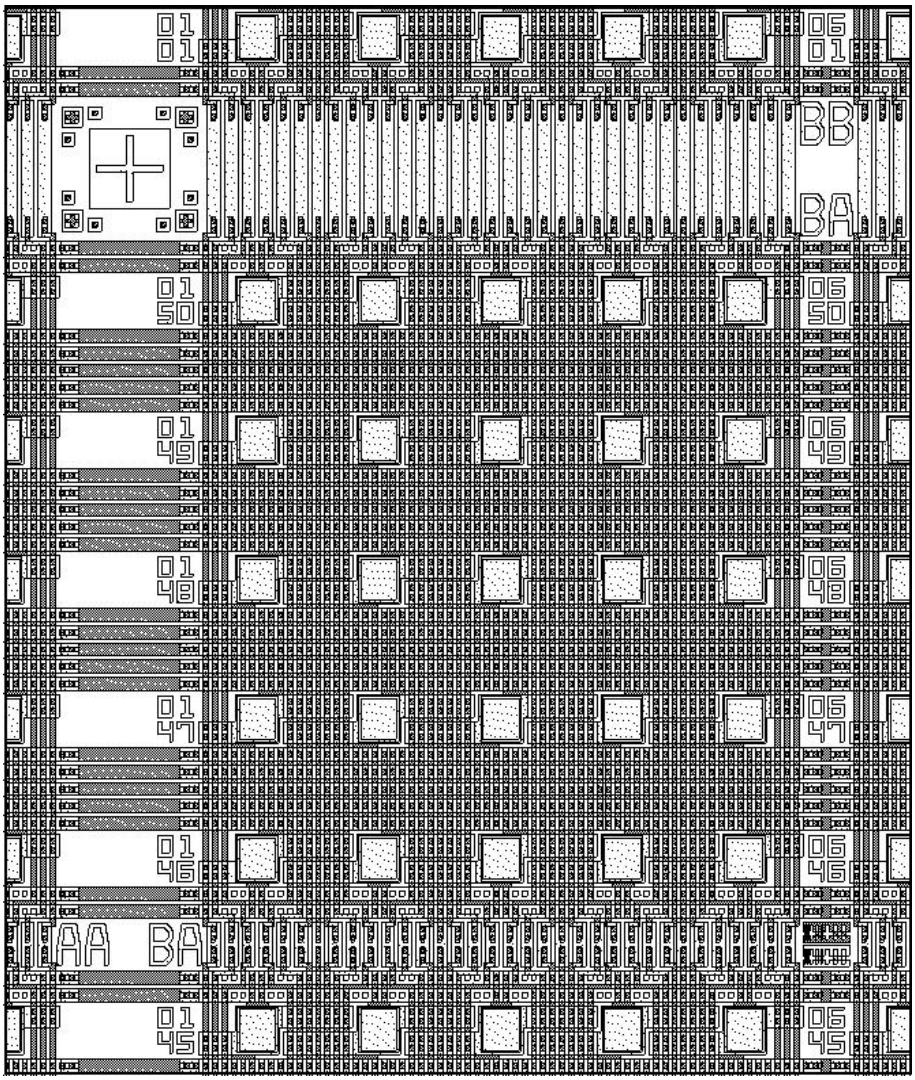

Figure 8.15: Top view of a segment of the single link design showing a laser alignment mark, metal tabs between segments and between big-segments.

Chapter 9

Conclusions and Future Work

9.1 Conclusions

In this work, the dynamics of laser metal cut process and the laser-induced vertical make linking process have been thoroughly investigated by means of experiments and finite element modeling. The followings are the summary of conclusions.

1. Finite element model has been simulated to study the metal-cut process. Experimental observations reveal that lower-corner cracks can be formed at low laser-energy level below passivation-break threshold energy. It is also shown through the observations that the stress-relief effect, due to cracking and breakthrough of passivation caused by upper-corner cracks, exists as predicted by simulations. Laser energy process window for the cut process exists and useful guidelines to get the maximum of the process window were obtained through simulations with various cut structures and laser parameters.

2. 3-D finite element modeling was performed to see if the pad cut structure is an improvement over the simple line cut structure. Simulation results showed

the higher upper corner stress in the case of pad cut structure, but the stress on lower corner in Plane A was much lower than that of the line cut structure. It indicate the improvement of pad cut over simple line cut structure. The results are consistent with the experimental observation results.

3. Laser processing of Cu fuse with two different wavelength laser has been analyzed. Unlike the Al processing, parallel-directed cracking was noticed in the upper and the lower corner. From the ideas of paralleled upper and lower cracks, lateral make-link proposed by J. B. Bernstein [29] is suggested for the repair process instead of cut structure. For improvement of Cu processing, it is of importance to modify the fabrication process, so the two layers of dielectric can stick to each other better. This will keep the crack from going to parallel direction and, thus the crater will have a smaller size.

4. The scalability of a direct metal-to-metal connection between two different levels of metallizations has been extrapolated to be compatible with modern semiconductor fabrication technology. A simple equation to evaluate the scalability was formulated based on FIB cross-sectional images of larger link structures with various sizes. With a 0.6 μm thick metal 1 line and a 0.5 μm thick ILD, a width of less than 0.5 μm is evaluated to be possible for the metal 1 line. Two limitations exist in the process of scaled-down link structures, which are the ratio of the thickness of ILD to the thickness of the metal 1 line, t_{ILD}/t_m, and the quality of laser beam parameters including the spot size and positioning error. However, modern processing technologies and advanced laser processing systems are considered to allow the scalability of vertical make-link structure.

5. Various link structures were simulated by finite element models and the results were consistent with the experimental results, which is a monotonically decreasing trend of relative energy process windows for smaller links. This results indicates that the scaling-down of the link size will raise the requirements on better processing quality of the laser parameters including spot size, positioning accuracy and energy stability. It is also shown that there always exists an acceptable energy process window for any scaled links as long as the lower metal line can share the metal with the resulting link sheet. Therefore, considering the energy process window as well as its scalability, the laser-induced vertical metallic link is expected to be a practical and seamless application for customization in modern IC design with a laser is practical. Dense layouts of interconnect were designed and proposed with a 1 μm pitch of 0.5 μm wide metal 1 line. The results demonstrate the seamless application for customization in programmable gate arrays and for additive redundancy in restructurable integrated circuits, or any other applications where post-processing with a laser is practical.

6. A new LPMCM substrate using the vertical make-link structure was designed. The MCM substrate, used for supporting the dies as well as the media for the interconnections among the dies, is made on 10 cm silicon wafer and contains many pads and tracks of two layers of metal. Due to the elimination of an entire level of packaging in chip-to-chip connections and the fast programmability, this LPMCM substrate will decrease the time and cost for fabrication of MCM which meets user's needs with sufficient reliability. In addition, all of the advantages of laser linking process indicate the potential for far-reaching appli-

cations in the field of MCM and, in turn, this will contribute to the trend of WSI.

9.2 Future Work

In order to achieve a more reliable metal cut process and make the linking process of commercial utility, more research must be conducted.

1. The present finite element analysis has been predicated on the absolute energy absorption, however, the effective laser energy absorption has many factors such as optical interference of reflected beam from the overcoating layer and the metallization. The passivation thickness is also important factor in deciding the effective energy absorption. Those factors need to be considered in the future analysis.

2. Especially in the simulations, the voiding mechanism in the lower metal during the laser heating is ignored so that the calculated stress at the lower corner is believed to be larger than the real value. Therefore, the simulation results deviate from the real value after cracking and passivation break. More sophisticated material modeling is needed to include more detailed information on the metal phase change and the flow of molten metal. On the other hand, the abrupt changes on material properties would lead to a highly nonlinear problem that greatly raises the requirement on convergence control. The stress release from the flow of metal can not be ignored and it will be the key factor to understand the whole procedure of laser processing.

3. Material properties of Cu should be refined to study the thermo-mechnical

phenomena of Cu fuse processing.

4. Cracking angle dependence on laser parameter should be more investigated in both cut and make link processes. This will enable optimizing the design of make link structure and reaching the scaled make links.

5. Theoretical explanation of super heating under laser heating should be investigated.

6. More detailed scalability and the energy process window study should be performed with consideration of laser positioning accuracy error.

7. The LPMCM is still in the design stage and will be produced. More test should be performed on produced substrate and the failure modes should be analyzed. Based on the results, more new designs of LPMCMs with better power distribution should be made.

BIBLIOGRAPHY

[1] N. Sherwani, Q. Yu, and S. Badida, *Introduction to multichip modules.* New York: John Wiley & Sons, Inc., 1995.

[2] I. Pico Technology, "Picostrate reliability." Technical Bulletin, 1999.

[3] R. Berger, R. S. Frankel, J. I. Raffel, C. E. Woodward, and P. W. Wyatt, "A laser-programmable multichip module on silicon," *IEEE International Conference on Wafer-Scale Integration*, pp. 30–35, 1993.

[4] B. A. Lengyel, "Evolution of lasers and masters," *Am. J. Phys.*, vol. 34, pp. 903–913, 1966.

[5] A. E. Siegman, *Lasers.* Mill Valley, CA: University Science Books, 1986.

[6] W. W. Duley, *Laser processing and analysis of materials.* Plenum Press, 1983.

[7] Y. Hua, "Mechanism and yield study of laser induced link and cut," Master's thesis, University of Maryland at College Park, 1997.

[8] R. Osgood, "Laser-fabrication for solid-state electronics," *IEEE Cir. Dev. Mag.*, vol. 6, no. 5, pp. 25–31, 1990.

[9] D. Ehrlich, "Critical issues for single-chamber manufacturing the role of laser technology," *Appl. Surf. Sci.*, vol. 69, no. 1-4, pp. 115–120, 1993.

[10] D. Ehrlich and J. Tsao, *Laser microfabrication.* Boston: Academic Press Inc., 1989.

[11] S. Logumer, *Laser Technology.* New Jersey: Prentice Hall, 1990.

[12] C. Lu, J. Chlipala, and L. Scarfone, "Explosion of poly-silicide links in laser programmable redundancy for vlsi memory repair," *IEEE Trans. Electron Devices*, vol. 36, no. 6, pp. 1056–1062, Jun.,1989.

[13] L. Scarfone and J. Chlipala, "Computer simulation of target link explosion in laser programmable redundancy for silicon memory," *J. Mat. Res.*, vol. 1, pp. pp368–381, Mar/Apr, 1986.

[14] H. Yamaguchi, M. Hongo, T. Miyauchi, and M. Mitan, "Laser cutting of aluminum stripes for debugging integrated circuits," *IEEE J. Solid-State Circuits*, vol. SC-20, no. 6, pp. 1259–1264, Dec.,1985.

[15] R. T. Smith and J. D. Chlipala, "Laser programmable redundancy and yield improvement in a 64k dram," *IEEE J. Solid-State Circuits.*, vol. SC-16, pp. 506–514, Oct. 1981.

[16] Y. Sun, *Laser processing optimization for semiconductor based devices.* PhD thesis, Oregon Graduate Institute, 1997.

[17] U. Patent, 1984. #4,455,495.

[18] S. S. Cohen and G. H. Chapman, *Laser beam processing and wafer-scale integration.* Beam Processing Technologies, New York: Academic Press, 1989.

[19] J. Raffel, R. Frankel, K. Konkle, and J. Murguia, "A laser-restructurable logic array for rapid integrated circuit prototyping," *Lincoln Laboratory Journal*, vol. 4, no. 2, pp. 97–112, 1991.

[20] P. Wyatt and J. Raffel, "Restructurable vlsi-a demonstrated wafer scale technology," *IEEE Proc. International Conference on Wafer-Scale Intergration*, pp. 13–20, 1989.

[21] J. Raffel, A. Anderson, and G. Chapman, "Laser restructurable technology and design," *Wafer Scale Integration*, no. 7, p. 363, 1989.

[22] R. Berger, A. Bertapelli, R. Frankel, J. Hunt, J. Raffel, J. Mann, R. Rhodes, A. Soares, and C. Woodward, "The lincoln programmable image-processing wafer," *Proc. International Conference on Wafer-Scale Integration*, 1990.

[23] H. Hartmann and T. Hillman-Ruge, "Yield and reliability of laser formed vertical links," *SPIE Proc. Multilevel Interconnections: Issues that Impact Competitiveness*, vol. 2090, pp. 146–160, 1993.

[24] M. Rouillon-Martin, M. Chambon, and A. Boudou, "Laser programmable vias for reconfiguration of integrated circuits," *SPIC Proc. of Optical Microlithography and Microcircuit Fabrication*, vol. 1138, pp. 190–197, 1989.

[25] J. B. Bernstein, T. Ventura, and A. Radomski, "High-density laser linking of metal interconnect," *IEEE Trans. Comp. Packag. Manufact. Technol.*, vol. 17A, no. 4, pp. 590–593, Dec.,1994.

[26] J. B. Bernstein, W. Zhang, and C. Nicholas, "Laser formed connections for programmable wiring," *Proc. of the IEEE Custom Integrated Circuits Conference*, pp. 163–165, 1998.

[27] W. Zhang, J. Lee, Y. Chen, J. B. Bernstein, and J. S. Suehle, "Reliablity of laser-induced metallic vertical links," *IEEE Trans. Comp. Packag. Manufact. Technol.*, vol. 22, no. 4, pp. 614–619, 1999.

[28] J. B. Bernstein, "Dielectric fracture leading to metallic connections by laser heating," *Proc. Mat. Res. Soc.*, Fall meeting, 1994.

[29] J. B. Bernstein and B. D. Colella, "Laser-formed metallic connections employing a lateral link structure," *IEEE Trans. Comp. Packag. Manufact. Technol.*, vol. 18A, no. 3, pp. 690–692, 1995.

[30] J. B. Bernstein, Y. Hua, and W. Zhang, "Laser energy limitation for buried metal cuts," *IEEE Electron Device Lett.*, vol. 19, no. 1, pp. 4–6, 1998.

[31] J. D. Chlipala, L. M. Scarfone, and C. Y. Lu, "Computer-simulated explosion of poly-silicide links in laser-programmable redundancy for vlsi memory repair," *IEEE Trans. Elecron Devices*, vol. 36, no. 11, pp. 2433–2439, 1989.

[32] S. S. Cohen, P. W. Wyatt, and G. H. Chapman, "Laser-induced melting of thin conduction films: Part i - the adiabatic approximation," *IEEE Trans. Electron Devices*, vol. 38, no. 9, pp. 2042–2050, 1991.

[33] Y. Sun, R. Harris, E. Swenson, and C. Hutchens, "Optimization of memory redundacy laser link processing," *SPIE*, vol. 2636, pp. 152–164, 1995.

[34] Y. Shen, S. Suresh, and J. B. Bernstein, "Laser linking of metal interconnects: Analysis and design considerations," *IEEE Trans. Electron Devices*, vol. 42, no. 3, pp. 402–410, 1996.

[35] R. Rasera and J. B. Bernstein, "Laser linking of metal interconnect: linking dynamics and failure analysis," *IEEE Tans. Comp. Packag. Manufact. Technol.*, vol. 19A, no. 4, pp. 554–561, 1996.

[36] R. L. Rasera, "Laser linking of metal interconnect: Process considerations and failure analysis using focused ion beam milling," Master's thesis, Massachusetts Institute of Technology, 1995.

[37] G. Yang, "Laser energy window simulation for metal cut structure," Master's thesis, University of Maryland at College Park, 1999.

[38] M. Finot, Y. L. Shen, A. Needleman, and S. Suresh, "Micromechanical modeling of reinforcement fracture in particle-reinforced metal -matrix composites," *Metallurgical and Materials Transactions*, vol. 25A, pp. 2403–2420, 1994.

[39] J. A. Collins, *Failure of materials in mechanical design*, p. 34. New York: John Wiley & Sons, 2nd ed., 1993.

[40] J. D. Chlipala and L. M. Scarfone, "Reliability aspects of laser programmable redundancy: Infrared vs. green, polysilicon vs. silicide," *IEEE/IRPS*, pp. 163–170, 1989.

[41] S. S. Cohen, P. W. Wyatt, J. A. Burns, and J. B. Bernstein, "The mechanism of laser-induced vertical links," *J. Electrochem. Soc.*, vol. 138, no. 10, pp. 3013–3018, 1991.

[42] J. B. Bernstein, W. Zhang, and C. Nicholas, "Laser formed metallic connections," *IEEE Trans. Comp. Packag. Manufact. Technol. Part B*, vol. 21, no. 2, pp. 194–196, 1998.

[43] J. B. Bernstein, "Technique for producing interconnecting conductive links," Jan. 19. 1999. U. S. Patent 5,861,325.

[44] W. Zhang, J. Lee, and J. B. Bernstein, "Energy effect of laser-induced vertical metallic link," *IEEE Tans. Semiconduct. Manufact.*, vol. 14, no. 2, pp. 163–169, 2001.

[45] S. Williamson, G. Mourou, and J. Li, "Time-resolved laser-induced phase transformation in aluminum," *Physical Review Letter*, vol. 52, no. 26, pp. 2364–2367, 1984.

[46] S. Williamson and G. Mourou, "Genesis of melting," *NATO ASI Series, Applied Sciences Laser Surface Treatment of Metals*, vol. E, no. 115, pp. 125–131, 1986.

[47] T. Kikkawa, "Quarter-micron interconnection technologies for 256m drams," *Extended Abstracts of the 1992 International Conference on Solid Devices and Materials*, pp. 90–92, 1992.

[48] W. Zhang, X. Xie, and J. B. Bernstein, "Laser-formed vertical metallic link and potential implementation in digital logic integration," *Proc. Military and Aerospace Applications of Programmable Devices and Technologies Conference*, 1999. Unpublished.

[49] G. S. Sandhu, "Process technology and integration challenges for high performance interconnects," *Thin Solid Films*, vol. 320, pp. 1–9, 1998.

[50] P. Kucher, H. Aochi, J. Gambino, T. Licata, T. Matsuda, S. Nguyen, M. Okazaki, H. Palm, and M.Ronay, "Advanced metallization technology for 256m dram," *Applied Surface Science*, vol. 91, pp. 359–366, 1995.

[51] C. Jesshope and W. Moore, eds., *Wafer Scale Integration*. Bristol, England: Adam Hilger, 1986.

[52] L. A. Bixby and D. T. Dimatteo, "Multichip module: An alternative packaging technology," *Hybrid Circuit Technology*, vol. 7, no. 12, pp. 9–13, 1990.

[53] D. Carey, "Programmable multichip module technology," *Hybrid Circuit Technology*, vol. 8, no. 8, pp. 25–29, 1989.

[54] R. O. Carlson and C. A. Neugebauer, "Future trends in wafer scale integration," *Proceedings of IEEE*, vol. 74, no. 12, p. 321, 1986.